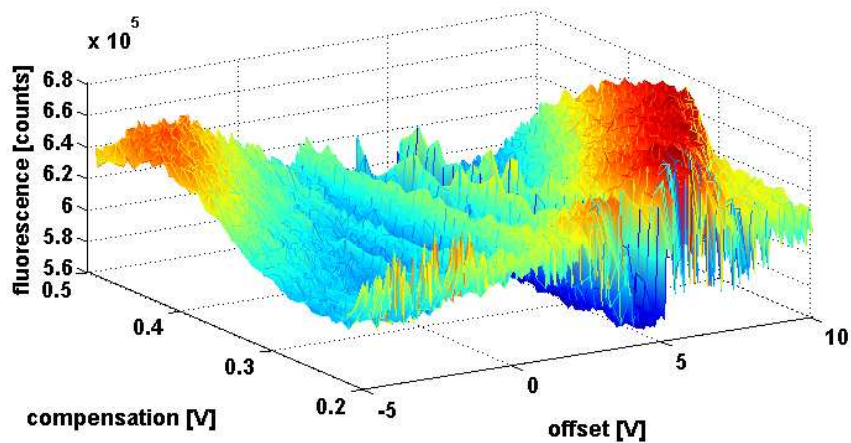




Detection of Qubit Registers in a Micro Trap



Alex Wiens

Quantum

Johannes Gutenberg University, Mainz

A thesis submitted for the degree of
Diplom Physiker (Master of Science)

12.07.2011

1. Reviewer: Prof. Dr. Ferdinand SCHMIDT-KALER

2. Reviewer: Prof. Dr. Klaus WENDT

Signature from head of committee:

Abstract

In this diploma thesis, important technological steps for the handling of multi qubit systems based on ions trapped in a microstructured segmented Paul trap are described for the purpose of designing scalable quantum computation hardware. A method for fast, accurate and parallel readout of a multi qubit system was realized. For qubit readout based on the detection of resonance fluorescence, the challenge lies in distinguishing between *bright* and *dark* states for a low photon flux in the presence of background noise. Our readout method is based on the usage of an EMCCD camera that provides spatial information, allowing us to individually determine the state of each qubit. Since high accuracy of state discrimination is required, several different approaches, such as *maximum likelihood* or *2D-masks*, are investigated and finally implemented into our experimental control system. A detailed comparison of the performance of different image processing algorithms is presented and a *Gaussian-shaped mask* algorithm, scaling to a two qubit system is demonstrated at an exposure time of 3 ms providing a discrimination fidelity of 99.970% which is limited by the spontaneous decay of a metastable state.

Further, a software package for ion positioning and transport in the segmented trap was created and tested. This software package provides control over a custom made multi-channel voltage supply acting as a fast arbitrary waveform generator with a maximum update rate of 2.5 Megasamples per second. The interface provides a convenient integration of transport operations into existing experiment control software. Several experiments based on these prerequisites were performed and are presented in this thesis. In one experiment, moving the ion through a laser beam allows us to employ it as a probe for the transverse mode laser profile with high precision. Transport sequences were applied to a single ion and a quantitative measurement

of energy transfer caused by the transport was performed. A combination of the EMCCD camera and the multi-channel arbitrary waveform generator was used to precisely measure the relative ion position along all three spatial directions. Further, the dependence of a single ion's resonance fluorescence to two compensation voltages was investigated, revealing yet not fully understood effects, encouraging us to further investigate the nature of multi-segmented Paul traps.

Zusammenfassung

In dieser Diplomarbeit werden wichtige technologische Schritte für das Arbeiten mit einer Vielzahl von Qubits, die in Form von gefangenen Ionen in einer segmentierten Mikrochip-Falle realisiert werden, beschrieben. Das Ziel hierbei ist die Realisierung eines skalierbaren Quantencomputers. Schnelle und genaue Diskriminierung einer Vielzahl von Qubits wird untersucht, wobei die Herausforderung für die Qubit-Auslese, die auf der Detektion von Resonanzfluoreszenz basiert, in der Unterscheidung von *hellen* und *dunklen* Zuständen bei niedriger Photonenzahl und hohem Hintergrundrauschen liegt. Für die Auslese wird eine EMCCD Kamera verwendet, deren Ortsauflösung es uns ermöglicht den Zustand jedes Qubits individuell zu bestimmen. Um eine möglichst hohe Genauigkeit der Diskriminierung zu erzielen, wurden verschiedene Herangehensweisen, wie zum Beispiel *Maximum-Likelihood* oder das Verwenden von *2D-Masken*, untersucht und in die Experiment Steuer Software integriert. Die verschiedenen Bildverarbeitungsalgorithmen werden detailliert miteinander verglichen und letztendlich ein Algorithmus auf Basis einer *Gaussförmigen Maske* auf ein Zwei-Ionen-Kristal angewandt. Die Diskriminierungsgenauigkeit des Algorithmus, bei einer Belichtungszeit von 3 ms, liegt dabei bei theoretischen 99,970%, die durch den spontanen Zerfall des metastabilen Zustands limitiert ist.

Ausserdem wurde ein Softwarepaket für die Positionsbestimmung und Transport in segmentierten Fallen programmiert und getestet. Dieses Paket ermöglicht die Kommunikation zwischen der Steuersoftware und einer sonderangefertigten Vielkanal-Spannungsquelle die mit maximal 2.500.000 Spannungenwerten pro Sekunde programmiert werden kann. Einige Experimente die die neuen Werkzeuge nutzen wurden durchgeführt: Eines der Experimente verwendet den Transport, um ein Ion durch ein Laserstrahl zu bewegen, was es uns ermöglicht das Ion als eine hochpräzise Sonde für das Laser-

profil zu benutzen. Ein ion wurde mit schnellen Transportrampen bewegt und der dabei auftretende Energietransfer quantitativ gemessen. Die Kombination der Ortsauflösung der EMCCD Kamera in Verbindung mit dem Vielkanal-Funktionsgenerator wird verwendet, um die Position des Ions in allen drei Dimensionen zu bestimmen. Desweiteren wird die Abhängigkeit der Resonanzfluoreszenz in Verbindung mit zwei Kompensationsspannungen, mit bisher nicht vollständig verstandenem Ergebnis, untersucht, was uns ermutigt in diese Richtung weiter zu forschen, um ein tieferes Verständnis für segmentierte Mikrochip-Fallen zu erlangen.

Contents

List of Figures	iii
List of Tables	v
List of Listings	vii
1 Introduction	1
2 Theoretical Foundations	5
2.1 Scalable Quantum Computation in Segmented Ion Traps	5
2.2 Atom-Light Interaction	8
2.3 One and Two Qubit Operations	11
2.4 Measurement	12
2.5 Single Qubit Tomography	13
2.6 Two Qubit Entanglement	14
2.7 Qubit Realization in a $^{40}\text{Ca}^+$ Ion	16
3 Detection- and Readout Systems	19
3.1 Readout Systems: CCD- vs. PMT	19
3.2 Detection Algorithms	27
3.3 Two Ion Discrimination at 3 ms Timescale with 99.999% Algorithm-Fidelity	40
4 Transport of Ions in a Segmented Paul Trap	45
4.1 Multi-Channel Arbitrary Waveform Generator	45
4.2 Transport and Splitting of a Two Ion Crystal	49

CONTENTS

5 Experiments	55
5.1 Ion as a Beam Profilometer	55
5.2 Fast Axial Transport of a Single Ion	57
5.3 Relative Ion Position Measurement	58
5.4 Reduction of Micromotion - Compensation Scan	59
5.5 Magnetic Gradient Measurement	62
6 Outlook	69
References	71
A Implementation of Camera into Control Program - MyCam	75
A.1 Function List	77
A.2 Example Code	84
A.3 Fitting Routine	88
B Implementation of Arbitrary Waveform Generator - myAnalogOut- Line	89
B.1 Function List	93
B.2 Example Code	95

List of Figures

2.1	Coupling of electronic transitions with the vibrational mode	6
2.2	Scheme of the multi-segmented Paul trap	7
2.3	Geometric Phase Gate	15
2.4	Level scheme of the relevant electronic states of the $^{40}\text{Ca}^+$	17
3.1	Structure of the objective designed by 'Sill Optics'	20
3.2	Top view scheme of the trap-apparatus	21
3.3	Quantum efficiency of the iXon CCD cameras	22
3.4	A schematic of an amplification register	23
3.5	Quantum efficiency of the PMT	25
3.6	Schematic of the beam splitter	25
3.7	Reflection/transmission measurement of the beam splitter	26
3.8	A histogram of a dark noise measurement at 3 ms exposure	27
3.9	Sequence to take signals of alternating 'bright' and 'dark' ion	28
3.10	PMT histogram taken at an exposure time $t_e = 2$ ms	29
3.11	Sample images at different exposure times	30
3.12	Histogram based on integrated pixel-counts of the camera image	30
3.13	Redefinition of the ROI	31
3.14	Classification results with redefined ROI	32
3.15	Gaussian fit applied to an image	33
3.16	Classification results using Gaussian mask	33
3.17	Histograms of two pixels for maximum likelihood algorithm	35
3.18	From count rates to probability distribution of two images at $t_e = 3$ ms .	36
3.19	Results of the 'Maximum likelihood' algorithm	37
3.20	A 2D 'support vector' calculation	38

LIST OF FIGURES

3.21	Results of the 'support vector machine' algorithm	39
3.22	Two Gaussian masks for two ion crystal	40
3.23	A two-step procedure to obtain a single, weighted profile of an ion	42
3.24	Histograms of the weighted left and right ion	43
3.25	Quantum jumps at 3 ms	43
3.26	Result of the Gaussian-Mask algorithm applied to random images	44
3.27	Set of images to verify the result of the algorithm	44
4.1	Scheme of the multi-channel arbitrary waveform generator	46
4.2	Example of simultaneous outputs	48
4.3	Noise measurement of the multi-channel waveform generator	48
4.4	Simple trapping potential	49
4.5	Transport by shifting the trapping potential	50
4.6	Intermediate potentials from segment four to six	51
4.7	Voltages required to realize the intermediate potentials	51
4.8	Linear transport ramp	52
4.9	Erf-shaped time dependent trajectory and force	52
4.10	Erf-shaped ion transport	53
4.11	Splitting scheme	54
5.1	Sketch of Rabi oscillations at different frequencies	56
5.2	Beam profile measurement	56
5.3	Transport to different distances at 200 μ s	58
5.4	Scheme of the electrodes used for the ion bearing measurement	59
5.5	Results of displacement measurement	60
5.6	Scheme of compensation	60
5.7	Doppler broadening used for reduction of micro motion	61
5.8	Red-detuned compensation and offset scan	62
5.9	Magnetic Gradient Measurement pulse scheme	63
5.10	Magnetic Gradient Measurement Bloch sphere view	63
B.1	Scheme of DAC programming	89
B.2	Scheme of the outputs of arbitrary waveform generator	93

List of Tables

3.1	Results of the simple ROI algorithm at different exposure times	31
3.2	Summary of the classification algorithms	39
3.3	Fraction of each state in the whole quantum jump sequence	43
B.1	FPGA bits to DAC connections	91

LIST OF TABLES

List of Listings

A.1	List of exported camera commands	76
A.2	List of camera commands	77
A.3	Creating a camera GUI object - Data2DPlotArray	84
A.4	How to use the camera in video mode	86
A.5	How to use the camera in kinetic mode	86
A.6	Fitting routine applied to an image	87
B.1	myAnalogOutLine class	93
B.2	create a FPGA connection and analog lines	95
B.3	simple sequence of analog values - slow	95
B.4	simple sequence of analog values - fast	96
B.5	Key function of myAnalogOutLine	96

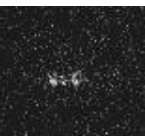
LIST OF LISTINGS

1

Introduction

Seventy years ago the digital computer began its rapid advance into the every-day routine of almost every branch of society one could think of and have since then become an indispensable tool for every scientist in the world. The first usable electro-mechanical computer Zuse Z3 could perform two addition operations every second resulting in 2 'floating point operations per second' (FLOPS). Today's personal computers have a computational power in the order of 100 GigaFLOPS and fit in a case not bigger than a shoe box. The current record of 8.162 PetaFLOPS has been recently achieved using 68544 processors. This tremendous increase of computational power of digital computers raises the question: why do we need a *quantum* computer?

Since the development of quantum physics the theory has been strictly tested due to its counterintuitive nature and superbly mastered every one of the tests with tremendous success. However, increasing understanding of quantum effects raised the necessity to simulate quantum systems, which, no matter how powerful the future computers might become, cannot be simulated by the mere computational power of a classical computer (solid state physics, condensed matter, etc.). Further, quantum information theory has shown that a quantum computer (QC) can solve some problems efficiently that are currently considered intractable on classical computers. In 1981 Richard P. Feynman proposed to simulate a quantum mechanical system using a computer operating based on quantum mechanical principles: the quantum computer. The task of designing a QC mainly consists of finding a suitable system of quantum bits (qubits) that can interact via quantum gates as described by the DiVincenzo criteria (CZ95). The main obstacle of realizing such a system remains the existence of decoherence, which arises



1. INTRODUCTION

from interaction of the computational units with the environment, destroying the phase coherences that give the quantum computation its power. Therefore, any computational task has to be completed within the coherence time. Magnetic field fluctuations are one of the main sources for coherence time limitations. One possibility to reduce decoherence is introducing a *decoherence free* subspace on the expense of using two physical qubits to realize one logic qubit (LCW98). Further, Quantum error-correction can be used to reduce the impact of decoherence (Sho95). On the one hand, the qubits needs to be well isolated from the environment in order to limit the decoherence effects, but on the other hand the qubits must be easily accessible from the outside and have strong coupling between each other in order to allow for state manipulation and for final readout of the computation result. The two requirements are generally incompatible, making it challenging to find a feasible implementation of a QC.

Over the last decades, several physical systems, all trying to fulfill the DiVincenzo criteria for quantum computing (BBC⁺95), have been proposed and partially realized. Since the quantum information community has grown fast within the last years, only a small field and groups can be mentioned in this theses:

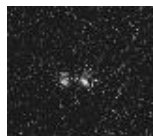
- Solid state approach
 - Superconductor- based quantum computers (CW08)
 - Quantum dots (FYV00),(LD98)
 - Nuclear magnetic resonance on molecules in solution (VSB⁺01)
 - Impurity doped crystals (NMR⁺08)
- Optical approach using spin states of photons (Mon02)
- Trapped ion quantum computer (CZ95)
- Optical lattices used for quantum computation (BCJD99)

So far, quantum computation based on trapped ions has demonstrated the most promising results since the trap apparatus presents a set of required properties by nature. Ions, confined in space, have a strong coupling provided by the Coulomb force which is much stronger than any other interaction for typical separations of a few wavelengths. Modern vacuum chambers have a good isolation of qubits from the environment leading to

long coherence times and allow optical access for manipulation and readout. The Innsbruck group around Rainer Blatt has demonstrated a full control of up to eight qubits (or one quByte) in a linear Paul trap, obtaining the maximum possible information on these states by performing a full characterization via state tomography (HHR⁺05), and in a more recent publication an entanglement of up to 14 qubits is shown (MSB⁺11). However, one of the basic limitations quantum computing in single potential Paul traps is the fact that scalability cannot be reached by putting more and more ions into the trapping well. Pursuing an equilibrium of Coulomb forces, a few ions will align themselves linearly along the axis, but increasing the number of ions will *compress* the ions to a point where the Coulomb repulsion is stronger than the radial restoring force, leading to a zigzag-shaped crystal. Another negative effect is that the number of vibrational modes increases linear with the number of ions in a single trapping potential. One ion has one vibrational mode, two ions have a *common-mode* and a *stretch-mode* and so on. All modes need to be cooled to the ground state, and individually addressed for coherent manipulation, making it challenging to operate with long ion crystals. Several ways to circumvent the scalability problems of ion traps have been proposed and partially realized:

- Atom-Photon networking (CZKM97), (WWKR07)
- Probabilistic entanglement (DBDM04), (MMO⁺07)
- Laserless quantum computing (MW01),(JBT⁺09)
- Fast gates on large ion arrays (GRZC03), (Dua04)
- Multiplexed/ Segmented ion traps (CZ95)

Here, the effort towards utilizing a micro-structured, segmented trap with a linear 3D geometry for scalable quantum logic is investigated. This thesis is organized in the following way, with chapter two containing a brief theoretical summary of atom-light interaction and basic features of quantum logic based on ion traps. The readout systems employing the spatial resolution of an EMCCD camera or the fast time response of a PMT, are presented in chapter three followed by a description of ion transport in a multi-segmented micro-structured Paul trap in chapter four. Experiments utilizing the shuttling and the introduced readout techniques are then presented in chapter five.



1. INTRODUCTION

2

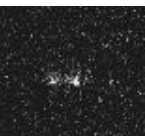
Theoretical Foundations

2.1 Scalable Quantum Computation in Segmented Ion Traps

Inspired by the great success of ion traps in the field of precision measurements Ignacio Cirac and Peter Zoller proposed ion traps to be used for quantum computation (CZ95) Trapped ions as qubit candidates provide the following features complying with the DiVincenzo criteria (DiV00):

- existing schemes for n -bit entangling quantum gates
- strong coupling of qubits provided by the Coulomb force which can be described in terms of normal modes. Two ions aligned in the axial direction of the trap have two normal modes: the *center-of-mass* mode at frequency ω_c , and the *stretch* mode at frequency $\omega_s = 3^{1/2}\omega_c$ where the ions oscillate in opposite directions. A set of $3..n$ ions have a variety of possible modes which scales linear with the number of ions.
- long decoherence times enabling computation
 - good isolation from outer influences.
 - spontaneous emission suppressed using long-lived atomic states
- readout can be performed with high efficiency

Two basic types of devices can confine charged particles to well-defined regions of free space: Penning traps and Paul traps. Although Penning traps nicely solve the



2. THEORETICAL FOUNDATIONS

fundamental problems of ion confinement, the trap's strong magnetic field hinders its application for quantum computation. For quantum information processing the cyclotron motion would have to be cooled to its ground state, which has proven to be a challenge for crystallized ion strings. These handicaps of the Penning trap, made the Paul trap the favorable tool to realize a QC.

Transitions between the atomic levels encoding the qubit can be driven using lasers. Two different degrees of freedom can be addressed: The internal electronic state of the qubits and the external, vibrational state of the trap, allowing one to interact with all qubits simultaneously. This way, both, single qubit rotations and multi-qubit entangling gate operations can be realized. The vector of an N qubit system is given by

$$|q_1, q_2, \dots, q_N\rangle |n\rangle \quad (2.1)$$

with the first kets representing the electronic state of each qubit and $|n\rangle$ referring to vibrational states of the common-mode. A system, cooled to the ground state is described by $|q_1, q_2, \dots, q_N\rangle |0\rangle$, with all ions at rest referring to the common mode, whereas $|q_1, q_2, \dots, q_N\rangle |1\rangle$ represents a state where the ions collectively oscillate along the trap axis at a frequency ω_c . This oscillation modulates sidebands onto the frequency spectrum where the most common are called *red sideband* and *blue sideband* (see figure 2.1). In section 2.6 it will be shown how the vibrational degree of freedom can be used

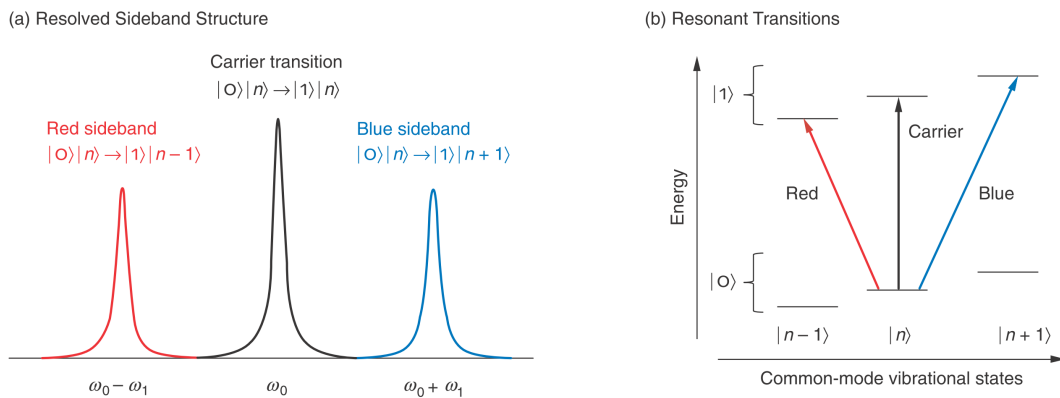


Figure 2.1: Coupling of electronic transitions with the vibrational mode. Each electronic transition at ω_0 (carrier) is accompanied by two sidebands at $(\omega_0 - \omega_1)$ (red side-band) and $(\omega_0 + \omega_1)$ (blue side-band). This is also the basic principle of sideband cooling.

Source: *Los Alamos Science* Number 27 2002

2.1 Scalable Quantum Computation in Segmented Ion Traps

to entangle two qubits. However, as already mentioned in the introduction, one of the basic limitations in a linear Paul trap is the fact that its scalability cannot be reached by putting more and more ions into the trapping well. The current state of the art is the demonstration of 14 entangled qubits in a linear Paul trap (MSB⁺11). Still, any further increment of this number is unlikely since the effort of maintaining full control scales non-linear with the number of ions. One way to overcome the limits for the manipulation of large ion crystals is the usage of micro fabricated Paul traps aligned in an array. The idea is to use more complicated electrode geometries where a smaller (e.g. two) number of ions is strapped in an individual Paul trap. In order to make use of the full number of ions as qubits, ions must be shuttled between the different trap regions. This approach was first presented in (KW02) and a successful demonstration of shuttling and splitting operations has been performed by (RBKD⁺02). We use a micro structured Paul trap with 32 segments (see figure 2.2), subdivided into three regions: i) A storage region where the ions are loaded and read out at segment five.

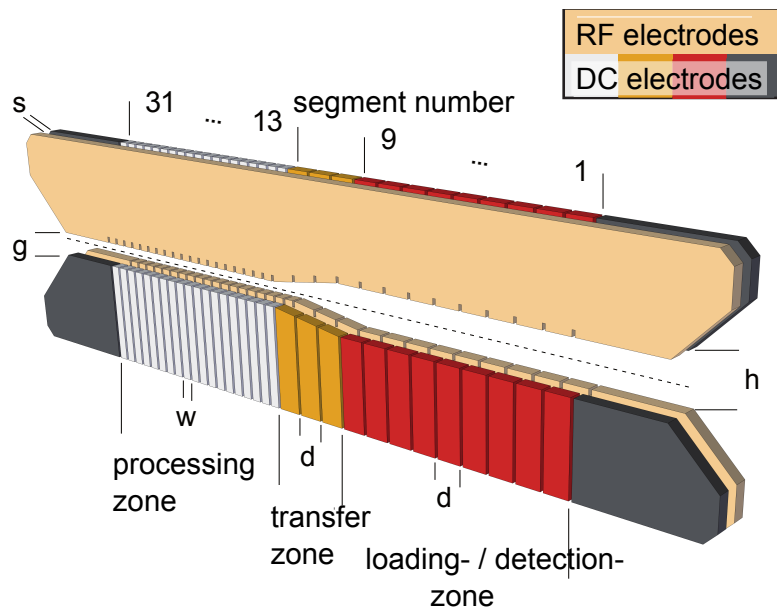
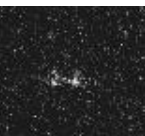


Figure 2.2: Scheme of the multi segmented Paul trap utilized in our experiment. The geometry parameters are: $d = 250 \mu\text{m}$, $w = 125 \mu\text{m}$, $h = 500 \mu\text{m}$, $g = 250 \mu\text{m}$, $g = 125 \mu\text{m}$
Original image: (Sch09)

ii) A processor zone where the geometry is changed to achieve higher axial frequency. And iii) a transfer region to make a smooth transfer from storage into processor region



2. THEORETICAL FOUNDATIONS

possible. The fabrication, assembly and mounting of the trap is described in detail in (Sch09). There are several other techniques proposed to achieve scalability of quantum computers based on Paul traps which are listed in chapter 4.1. The next chapter will briefly summarize the theory of atom-light interaction, since major part of this thesis deals with fluorescence-based readout and determination of qubit states.

2.2 Atom-Light Interaction

The Hamilton operator H of the system composing a Hamilton operator H_{at} of an atom at rest and the time dependent coupling $V(t)$ describe the atom-light interaction.

$$H = H_{at} + V(t) \quad (2.2)$$

For the sake of simplicity, the atom is treated as a two-level system having a ground state $|0\rangle$ and an excited state $|1\rangle$ with a total energy difference $\Delta E_{21} = \hbar(\omega_2 - \omega_1) = \hbar(\Delta\omega_{21})$. Here, the time dependent potential term can be described by $V(t) = -\hat{\mathbf{d}}\boldsymbol{\epsilon}E_0 \cos(\omega_L t)$ where $\hat{\mathbf{d}} = -e\hat{\mathbf{r}}$ is the electric dipole operator and E_0 gives the amplitude with the polarization $\boldsymbol{\epsilon}$ of the laser beam at a frequency ω_L . Using a general expression for a two level system wave function

$$\Psi(\mathbf{r}, t) = c_1(t)e^{i\omega_1 t}u_1(\mathbf{r}) + c_2(t)e^{i\omega_2 t}u_2(\mathbf{r}) \quad (2.3)$$

where c_1 and c_2 describe the time dependence of the amplitudes of the stationary Eigenfunctions $u_{1,2}(\mathbf{r})$, we can write the time dependent Schrödinger equation as a set of first order ordinary differential equations:

$$i\hbar \frac{\partial}{\partial t} \Psi(\mathbf{r}, t) = H\Psi(\mathbf{r}, t) \quad (2.4)$$

$$\begin{aligned} \dot{c}_1(t) &= i \frac{d_{12}^\epsilon E_0}{\hbar} e^{i\omega_{21}t} \cos(\omega_L t) c_2(t) \\ \dot{c}_2(t) &= i \frac{d_{12}^\epsilon E_0}{\hbar} e^{i\omega_{21}t} \cos(\omega_L t) c_1(t) \end{aligned} \quad (2.5)$$

where $d_{12}^\epsilon = \langle 1 | \hat{\mathbf{d}} | 2 \rangle \boldsymbol{\epsilon} =: d$ is the atomic dipole matrix element. Equations 2.5 can be decoupled and solved in the *Rotating-Wave-Approximation* frame (Blo06) leading to:

$$\begin{aligned} |c_1(t)|^2 &= \frac{\Omega_0^2}{2\Omega^2} \{1 + \cos(\Omega t)\} \\ |c_2(t)|^2 &= \frac{\Omega_0^2}{2\Omega^2} \{1 - \cos(\Omega t)\} \end{aligned} \quad (2.6)$$

with $\Omega = \sqrt{\Omega_0^2 + \delta^2}$ being the *general Rabi frequency* and δ describing the detuning of the light field and the resonant atomic transition. $\Omega_0 = \frac{dE_0}{\hbar}$ is the *bare Rabi frequency* with d being the dipole matrix element and E_0 the amplitude of the light field. The system oscillates between the two states at the Rabi frequency Ω which depends on the intensity of the laser, and can be prepared in a desired state by adjusting the pulse area $A = \Omega t$. Here, A is often chosen to match:

- $\pi/2$ -pulse

A system initially prepared in the ground state $|0\rangle$ can be transferred into an equal superposition state of the ground and excited state. This pulse is often used in a Ramsey scheme.

- π -pulse

A system initially prepared in the ground state $|0\rangle$ can be fully¹ transferred into excited state resulting in complete population inversion.

Note that the contrast of the Rabi oscillations highly depends on the detuning δ . The atom-light interaction can be treated in a similar way to describe quadrupole transitions with a quadrupole matrix element $M^{E2} = \epsilon \langle 1 | e(\mathbf{r} \circ \mathbf{r}) \mathbf{k}^{(0)} | 2 \rangle$. A forbidden dipole transition $d = 0$ usually can be driven using a quadrupole transition.

Photon Scattering

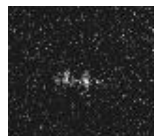
In previous calculations the limited lifetime of the excited state $|1\rangle$ of the two level system was neglected. To take this limitation into account the density matrix

$$\rho = \begin{pmatrix} \rho_{11} & \rho_{21} \\ \rho_{21} & \rho_{22} \end{pmatrix} = \begin{pmatrix} c_1 c_1^* & c_1 c_2^* \\ c_2 c_1^* & c_2 c_2^* \end{pmatrix} \quad (2.7)$$

can be used where the off-diagonal elements ρ_{21} and ρ_{12} describe the coherent behavior of the system, while the diagonal elements ρ_{11} and ρ_{22} describe the population probabilities to find the system in a given state $|0\rangle$ or $|1\rangle$. Further, the following relationships between the matrix elements can be shown:

$$\begin{aligned} 1 &= \rho_{22} + \rho_{11} \\ \rho_{12} &= \rho_{21}^* \end{aligned} \quad (2.8)$$

¹Full transfer is only possible for the resonant case.



2. THEORETICAL FOUNDATIONS

Time evolution of the density matrix elements without spontaneous decay can be obtained by differentiation with respect to t (Blo06):

$$\begin{aligned} \frac{d}{dt}\rho_{11} &= i\frac{\Omega_0}{2}(\rho_{21} - \rho_{12}) \\ &\vdots \end{aligned} \quad (2.9)$$

By introducing the variables $\rho_{\tilde{1}2} = e^{-i\delta t}\rho_{12}$ and $\rho_{\tilde{2}1} = e^{i\delta t}\rho_{21}$ the system is now in the rotating frame of the light field ω_L . To take the spontaneous decay into account equations 2.9 can be expanded with a damping parameter γ resulting in:

$$\begin{aligned} \frac{d}{dt}\rho_{11} &= \gamma\rho_{22} + i\frac{\Omega_0}{2}(\rho_{\tilde{2}1} - \rho_{\tilde{1}2}) \\ \frac{d}{dt}\rho_{22} &= -\gamma\rho_{11} + i\frac{\Omega_0}{2}(\rho_{\tilde{1}2} - \rho_{\tilde{2}1}) \\ \frac{d}{dt}\rho_{\tilde{1}2} &= -(\gamma/2 + i\delta)\rho_{\tilde{1}2} + i\frac{\Omega_0}{2}(\rho_{22} - \rho_{11}) \\ \frac{d}{dt}\rho_{\tilde{2}1} &= -(\gamma/2 - i\delta)\rho_{\tilde{2}1} + i\frac{\Omega_0}{2}(\rho_{11} - \rho_{22}) \end{aligned} \quad (2.10)$$

which are known as the *Optical-Bloch-Equations* (OBEs) and fully describe the atom-light interaction in the Rotating-Wave-Approximation. Using the relations 2.8 the OBEs can be reduced to two equations:

$$\begin{aligned} \frac{d}{dt}\rho_{\tilde{2}1} &= -(\gamma/2 - i\delta)\rho_{\tilde{2}1} - i\frac{w\Omega_0}{2} \\ \frac{d}{dt}w &= -\gamma(w + 1) - i\Omega_0(\rho_{\tilde{2}1} - \rho_{\tilde{1}2}) \end{aligned} \quad (2.11)$$

with the introduced inversion factor $w = \rho_{22} - \rho_{11}$. Solving the stationary case $\frac{d}{dt}w = 0$ (difference in population does not change) and constant coherence $\frac{d}{dt}\rho_{\tilde{2}1}$, one obtains:

$$\begin{aligned} w &= -\frac{1}{1 + S} \\ \rho_{\tilde{2}1} &= \frac{i\Omega_0}{2(\gamma/2 - i\delta)(1 + S)} \end{aligned} \quad (2.12)$$

where Ω_0 is the bare Rabi frequency and δ is the detuning to resonance. Further, the *saturation parameter* $S = \frac{S_0}{1 + 4\delta^2/\gamma^2}$, with $S_0 = \frac{2\Omega_0^2}{\gamma^2}$ being the *bare saturation parameter*, have been introduced. The combination of relation 2.8 and equation 2.12 using the obtained expression for the saturation, yields to the an expression for photon scattering rate:

$$\Gamma_{\text{scat}} = \gamma\rho_{22} = \frac{\gamma}{2} \frac{S_0}{1 + S_0 + 4\delta^2/\gamma^2} \quad (2.13)$$

which is limited to $\Gamma = \gamma/2$ for $S_0 \rightarrow \infty$.

2.3 One and Two Qubit Operations

The development of a quantum computer begins with a set of basic tools and the simplest system - a single qubit. A single qubit vector can be parameterized using a ket $|\phi\rangle = a|0\rangle + b|1\rangle$ with a and b being complex numbers satisfying $|a|^2 + |b|^2 = 1$. Any given operations on a qubit must preserve this norm, and thus are described by 2×2 unitary matrices. The basic and most important of these are the Pauli matrices given by:

$$\begin{aligned}\sigma_1 = \sigma_x &= \begin{pmatrix} 0 & 1 \\ 1 & 0 \end{pmatrix} \\ \sigma_2 = \sigma_y &= \begin{pmatrix} 0 & -i \\ i & 0 \end{pmatrix} \\ \sigma_3 = \sigma_z &= \begin{pmatrix} 1 & 0 \\ 0 & -1 \end{pmatrix}\end{aligned}\tag{2.14}$$

These matrices give rise to three useful classes of unitary matrices, the *rotation operators* about the \hat{x} , \hat{y} and \hat{z} axes defined by the equations:

$$\begin{aligned}R_x(\theta) &\equiv e^{-i\theta\sigma_x/2} = \begin{pmatrix} \cos(\theta/2) & -i\sin(\theta/2) \\ -i\sin(\theta/2) & \cos(\theta/2) \end{pmatrix} \\ R_y(\theta) &\equiv e^{-i\theta\sigma_y/2} = \begin{pmatrix} \cos(\theta/2) & -\sin(\theta/2) \\ \sin(\theta/2) & \cos(\theta/2) \end{pmatrix} \\ R_z(\theta) &\equiv e^{-i\theta\sigma_z/2} = \begin{pmatrix} \cos(\theta/2) - i\sin(\theta/2) & 0 \\ 0 & \cos(\theta/2) + i\sin(\theta/2) \end{pmatrix}\end{aligned}\tag{2.15}$$

Thinking of a Bloch sphere; applying these operations on a Bloch vector rotates the vector at a given angle θ around the axis u , v or w . A qubit prepared in the state $|0\rangle$ can be thus put to a superposition $|\phi\rangle = 1/\sqrt{2}(|0\rangle + |1\rangle)$ by rotating around the y axis. A combination of these primitive operations

$$U = a \cdot R_x(\alpha) + b \cdot R_y(\beta) + c \cdot R_z(\gamma)\tag{2.16}$$

can be used to create special qubit operations, e.g. *Hadamard gate*. Similar to a classical computer, a controlled operation on two input states is the most useful operation to perform (if 'a' is true then do 'b'). In analogy to the elementary *exclusive OR* (xOR) operation¹ of a classical computer, the quantum algorithms can be based on a series of

¹classical computers usually use a *not AND* (NAND) to realize xOR, NOR etc. but they can be converted into each other.



2. THEORETICAL FOUNDATIONS

controlled NOT (cNOT) gates, which is given by $|c\rangle|t\rangle \rightarrow |c\rangle|t \oplus c\rangle$, where c denotes the *control* qubit and t the *target* qubit respectively. If the control qubit is $|1\rangle$ then the target qubit is flipped. This operation can be written as a 4×4 matrix:

$$C_{NOT} = \begin{pmatrix} 1 & 0 & 0 & 0 \\ 0 & 1 & 0 & 0 \\ 0 & 0 & 0 & 1 \\ 0 & 0 & 1 & 0 \end{pmatrix} \quad (2.17)$$

The C_{NOT} gate is important since a combination of this gate with a single qubit rotation is a uniform tool to construct any type of quantum gate, allowing one to realize quantum logic circuits.

2.4 Measurement

The final step in a quantum circuit is the measurement. Quantum measurements are described by a collection $\{M_m\}$ of *measurement operators*. These are operators acting on the state space of the system being measured. The index m refers to the measurement outcomes that may occur in the measurement (NC03). In the bra-ket notation the probability of the vector $|\psi\rangle$ to be found in a given state m after a measurement is given by:

$$p(m) = \langle \psi | M_m^\dagger M_m | \psi \rangle \quad (2.18)$$

with M being the measurement operator satisfying the *completeness relation*

$$\sum_m M_m^\dagger M_m = \mathbb{1} \quad (2.19)$$

Or putting it other way around; the vector $|\psi\rangle$ of the system after a measurement is:

$$|\psi\rangle = \frac{M_m |\psi\rangle}{\sqrt{\langle \psi | M_m^\dagger M_m | \psi \rangle}} \quad (2.20)$$

An important example of a measurement is the measurement of a qubit in *the computational basis*. This is a measurement of a single qubit with two different outcomes, defined by two measurement operators $M_0 = |0\rangle\langle 0|$ and $M_1 = |1\rangle\langle 1|$. Assuming the measured state to be $|\psi\rangle = a|0\rangle + b|1\rangle$ the probability $p(0)$ to find the system in the state $|0\rangle$ is given by:

$$\begin{aligned} p(0) &= \langle \psi | M_0^\dagger M_0 | \psi \rangle \\ &= \langle 0 | a^* | 0 \rangle \langle 0 | a | 0 \rangle = |a|^2 \end{aligned} \quad (2.21)$$

and $p(1)$ given in a similar manner.

Projective Measurements

A projective measurement is described by an observable, M , a Hermitian operator on the state space of the system being observed. The observable M can be written as a composition of eigenvectors P_m with eigenvalues m :

$$M = \sum_m m P_m \quad (2.22)$$

Upon measuring the state of $|\psi\rangle$, the probability of observing the result m is given by:

$$p(m) = \langle \psi | P_m | \psi \rangle \quad (2.23)$$

For any system the eigenvectors P_m can be understood as projective operators onto an eigenspace of a chosen basis. The average value of the observable M is then given by $\langle \psi | M | \psi \rangle$, and if a large number of experiments is performed the standard deviation of the observed values is determined by: $\Delta M = \sqrt{\langle M^2 \rangle - \langle M \rangle^2}$.

2.5 Single Qubit Tomography

Tomography is a method to reconstruct quantum states from a finite amount of measurements. The most general description of a single qubit state is the density matrix

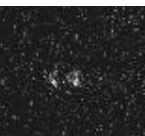
$$\rho = \begin{pmatrix} \rho_{11} & \rho_{21} \\ \rho_{21} & \rho_{22} \end{pmatrix} \quad (2.24)$$

and since its a density matrix it must be Hermitian and have a trace $Tr\{\rho\} = 1$. Therefore, the density matrix of a two-level system is fully determined by four real parameters which can be reduced to three using the constraint of $Tr\{\sigma\} = 1$, which is valid when the system is closed. The tomography procedure relies on the fact that every density matrix ρ can be expanded into a series of mutually orthogonal operators. For a single qubit:

$$\rho = \frac{Tr\{\sigma_1\rho\}\sigma_1 + Tr\{\sigma_2\rho\}\sigma_2 + Tr\{\sigma_3\rho\}\sigma_3}{2} \quad (2.25)$$

where σ_i are the Pauli matrices. Or more general:

$$\rho = \sum_{\vec{\nu}} \frac{Tr\{\sigma_{\nu_1} \otimes \sigma_{\nu_2} \cdots \otimes \sigma_{\nu_N} \rho\} \sigma_{\nu_1} \otimes \sigma_{\nu_2} \cdots \otimes \sigma_{\nu_N}}{2^N} \quad (2.26)$$



2. THEORETICAL FOUNDATIONS

having N -qubits system. Therefore, the density matrix ρ of a given state can be reconstructed by measuring the expectation values of the operators σ_i or the corresponding tensor products for a N -qubit system respectively. Projective measurements are usually performed to determine the elements of the density matrix ρ . Therefore, the experiment needs to be prepared and measured numerous times in order to obtain sufficient accuracy. Still, since the amount of measurements is limited and the resulting density matrix has to meet the constraints of being Hermitian and having a $Tr\{\rho\} = 1$ the methods of *maximum likelihood* can be applied to obtain a best matching density matrix to the taken data. One can define a cost function:

$$C = \left| \sum_{i=1}^2 \sum_{j=1}^2 (\rho_R - \rho_T)_{i,j} \right|^2 \quad (2.27)$$

with ρ_T contains the measured elements of the density matrix and ρ_R is a positive definite density matrix. To obtain a positive definite matrix the approach of (JKMW01) can be used. This technique can be extended to a N -qubit setup.

2.6 Two Qubit Entanglement

The last sections showed how to perform operations on one or two qubits and how to measure this quantum system. Here a brief summary is describing how a common vibrational mode of a two ion crystal can be used to entangle two ions. The vibrational mode can be coherently displaced in the position-momentum (z,p) phase space by applying a classical force $F = F_0 \sin(\omega t - \phi)$ with ω chosen to match the frequency of the harmonic oscillator. If the force acts for a time t , a displacement by Δz and Δp in phase space is formally described by the effect of the displacement operator on the quantum state $|n\rangle$ of the harmonic oscillator:

$$D(t) = -\frac{F_0 z_0}{2\hbar} e^{i\phi} \cdot t \quad (2.28)$$

where $z_0 = \frac{\hbar}{2m\omega}^{1/2}$ is the spread of the ground state. The phase factors for all displacements accumulate in such a way that a geometric phase $\phi_g = \frac{A}{\hbar}$ is acquired, with A being the area covered in the p - z space (LDM⁺03). Generally, the state of the harmonic oscillator changes after a displacement pulse, but if the force is applied in a way that the loop in the p - z space is closed, the harmonic oscillator returns to its original state.

A state-dependent coherent force can be applied to entangle two ions which is shown in the following.

Using the notation introduced in 2.1, a two qubit state initialized in the internal and external ground state is given by $|00\rangle|0\rangle$. The coherent force is designed in a way that only different states are affected. This can be realized by adjusting two laser beams with relative detuning of $\omega = \omega_1 - \omega_2$ and a total wavevector $k = k_1 - k_2$ along the axial direction of the trap. If ω is close to the frequency ω_s , the stretch mode can only be excited if the ions are in different states ($|01\rangle$ or $|10\rangle$). Adjusting the displacement force to accumulate a total phase $\phi_g = \pi/2$ in a loop in (p-z) space after a time t , the states change as follows:

$$\begin{aligned}
 |00\rangle|0\rangle &\xrightarrow{D} |00\rangle|0\rangle \\
 |01\rangle|0\rangle &\xrightarrow{D} e^{i\pi/2} |01\rangle|0\rangle \\
 |10\rangle|0\rangle &\xrightarrow{D} e^{i\pi/2} |10\rangle|0\rangle \\
 |11\rangle|0\rangle &\xrightarrow{D} |11\rangle|0\rangle
 \end{aligned} \tag{2.29}$$

A combination of qubit rotations and the state-dependent force in a sequence can be used to entangle ions. Figure 2.3 shows a spin echo scheme performed by D. Leibfried et. al. with an entangling fidelity of 97% (LDM⁺03). The first $\pi/2$ -pulse transforms

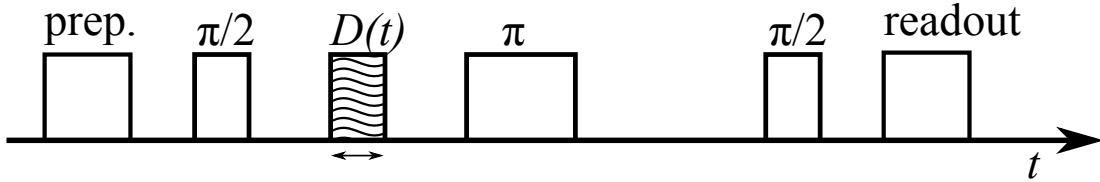


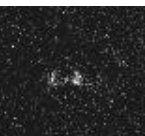
Figure 2.3: Geometric phase gate sequence applied to perform qubit entanglement.

the two ions into a superposition:

$$\Psi_0 := |00\rangle|0\rangle \xrightarrow{\pi/2} 1/2(|00\rangle + |11\rangle + |01\rangle + |10\rangle) =: \Psi_1 \tag{2.30}$$

The state-dependent force is only affecting the combination of different states, leading to:

$$\begin{aligned}
 \Psi_1 &\xrightarrow{D(t)} 1/2[(|00\rangle + |11\rangle)|0\rangle \\
 &\quad + e^{i\phi_g(t)}(|01\rangle|\alpha(t)\rangle + |01\rangle|-\alpha(t)\rangle)] =: \Psi_2
 \end{aligned} \tag{2.31}$$



2. THEORETICAL FOUNDATIONS

The subsequent π - and the following $\pi/2$ -pulse generally transform Ψ_2 into a more complicated superposition state:

$$\begin{aligned} \Psi_2 &\xrightarrow{3/2\pi} 1/2[(|00\rangle + |11\rangle) |0\rangle \\ &+ 1/2e^{i\phi_g(t)} (|01\rangle - |11\rangle + |00\rangle - |10\rangle) |\alpha(t)\rangle \\ &+ 1/2e^{i\phi_g(t)} (|10\rangle - |11\rangle + |00\rangle - |01\rangle) |-\alpha(t)\rangle =: \Psi_3 \end{aligned} \quad (2.32)$$

Adjusting the trapping- and laser parameters to match $\phi_g(t) = \pi/2$ and $\alpha(t) = 0$ (closed loop), results in an overall transformation:

$$\Psi_0 \longrightarrow 2^{-1/2} (|00\rangle + i|11\rangle) |0\rangle \quad (2.33)$$

with two ions, initially prepared in the ground state, entangled. Note that during this process the stretch mode was used as a bus to realize the entanglement.

2.7 Qubit Realization in a $^{40}\text{Ca}^+$ Ion

To store any information using an atomic qubit with two states, having lifetimes longer than the total preparation, computation and readout time, are required. Three basic types of internal states of an atom are suitable and have been successfully implemented within the last decade each having its advantages and disadvantages (Pos11):

- Internal metastable electronic states. Coherent manipulations are driven directly on dipole-forbidden transition (typically quadrupolar). The coherence time is given by the coherence of the used laser, requiring high effort on stabilizing the laser in the 1 Hz regime, which is nowadays routinely achieved in quantum optics laboratories. Ultimately, the coherence is limited by the lifetime of the metastable state. One particular advantage of this type of qubit is that the readout can be performed directly as fluorescence on the fundamental dipole transition will only be detected if the qubit is in the ground state.
- Hyperfine- or Zeeman sublevels of the electronic ground state. Coherent manipulation can be performed utilizing stimulated Raman transitions. The readout of this qubit type is generally more difficult since both qubit levels will yield fluorescence upon resonant irradiation on a dipole transition. One method to circumvent this is the usage of the quadrupole transition to *hide* the population

of one level in a metastable state¹. The predominant decoherence source is given by fluctuating magnetic fields. *Clock states* can be chosen for encoding the qubit. These do not possess a first-order Zeeman splitting, such that this decoherence process is strongly suppressed. Clock state encoding is only possible for hyperfine and the metastable qubit. Further, rephasing techniques for coherence protection can be used. Moreover, the already mentioned, decoherence free subspace can be used to avoid the impact of magnetic field on the expense of two physical qubits for one logic qubit.

To realize the atomic qubit in our experiment we chose the Zeeman sublevels of a $^{40}\text{Ca}^+$ ion. Figure 2.4 shows the level scheme of a $^{40}\text{Ca}^+$ ion, along with the transitions used for our particular qubit realization. Two coils, arranged at a 45 degree angle with

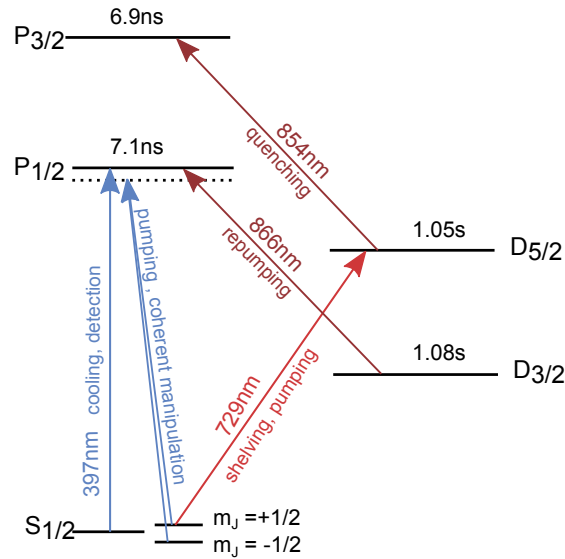
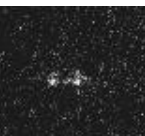


Figure 2.4: Level scheme of the relevant electronic states of the $^{40}\text{Ca}^+$ utilized in our experiment. The hyperfine substructure and other levels are omitted here. The laser-driven transitions between the states are shown along with their purpose and the wavelength.

respect to the axial direction of the trap, set to a total magnetic field of 0.7 mT, provide the quantization axis and the Zeeman sub structure. The resulting splitting of the $S_{1/2}$ state is approximately given by 18 MHz. This setup was build and characterized by Jens Welzel (Wel11). The manipulation of the two qubit states $|0\rangle = S_{1/2}, m_J = -1/2$ and $|1\rangle = S_{1/2}, m_J = +1/2$ is performed by a stimulated Raman transition (Pos11). Since

¹Used in our experiment



2. THEORETICAL FOUNDATIONS

the Doppler cooling and readout laser is not narrow enough to distinguish between the two spin states, a 729 nm frequency stabilized diode laser is used to shelve the $m_J = +1/2$ state to the metastable $D_{5/2}$ state. Therefore, states being in the $m_J = +1/2$ are called 'dark' since no fluorescence light is emitted while driving the 397 nm transition. The $m_J = -1/2$ state is called 'bright' respectively. The 729 nm quadrupole transition can be used to realize an optical qubit with $|0\rangle = S_{1/2}$ and $|1\rangle = D_{5/2}$ also.

3

Detection- and Readout Systems

3.1 Readout Systems: CCD- vs. PMT

The readout of atomic quantum bit (qubit) states is commonly accomplished by measuring fluorescence light. Depending on the amount of detected photons, one classifies the state into 'bright' or 'dark'. In our microtrap experiment a $^{40}\text{Ca}^+$ ion is used and we can address two kinds of qubits:

- Metastable electronic state with $S_{1/2} \longleftrightarrow D_{5/2}$ quadrupole transition near 729 nm used for qubit states.
- Zeeman sublevels where $S_{1/2, m_J = +1/2} \longleftrightarrow S_{1/2, m_J = -1/2}$ states are manipulated using the $P_{1/2}$ level for stimulated Raman transitions.

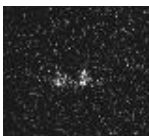
Figure 2.4 shows the level scheme of a $^{40}\text{Ca}^+$ ion, along with the transitions used for our particular qubit realization. In both cases the readout is done by driving the $S_{1/2} \longrightarrow P_{1/2}$ transition near 397 nm, making detection of photons of fundamental importance to our experiment.

Technical requirements for photon detection are the following:

- collect as much fluorescence light as possible
- efficiently detect collected light

Thus, an imaging setup covering a large solid angle (see figure 3.2) and furthermore, an extremely sensitive detection device as we want to operate in realtime¹ are required.

¹timescale: 100-1000 μ s



3. DETECTION- AND READOUT SYSTEMS

To meet the requirement of collecting maximum amount of fluorescence light a custom-

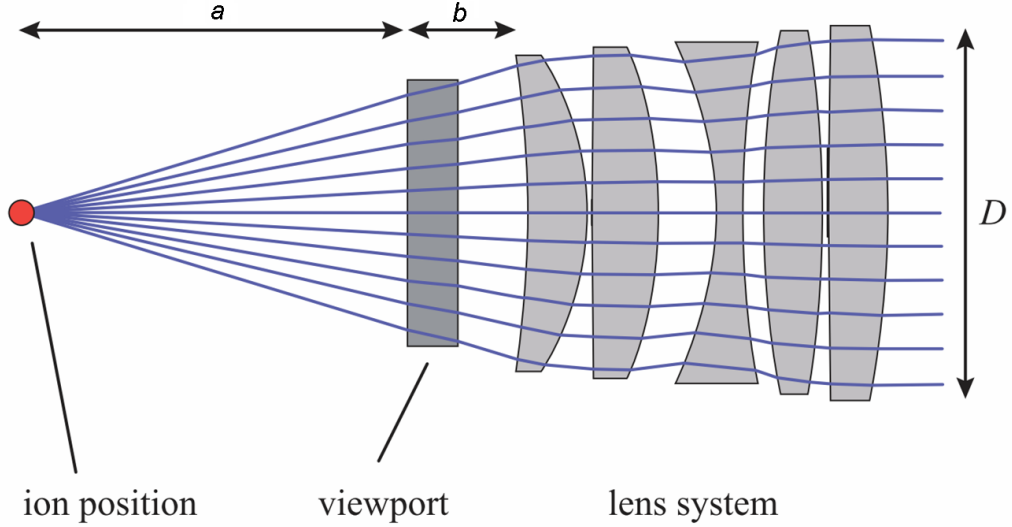


Figure 3.1: Structure of the used objective designed by 'Sill Optics'. Distance of the light source (ion) is supposed to be $a \approx 40$ mm. The distance of the objective is approximately $b \approx 10$ mm resulting in a total distance $d \approx 50$ mm. The aperture $D = 38$ mm and distance d are limiting the covered solid angle. The numerical aperture is specified to $A_N=0.27$. Source: (Sch10)

made objective (see figure 3.1) has been designed (Mai06) and placed as close as possible to the trap. Assuming a distance $d = 50$ mm and a lens diameter $D = 38$ mm one calculates¹ the covered solid angle

$$\Delta\Omega = \frac{S}{R^2} = 2\pi \left\{ 1 - \frac{d}{\sqrt{\left(\frac{D}{2}\right)^2 + d^2}} \right\} = 0.410 \quad (3.1)$$

resulting in an approximate number of collected photons

$$N \approx t_e \cdot S \cdot QE \cdot T \cdot \frac{\Delta\Omega}{4\pi}. \quad (3.2)$$

where t_e is the exposure time of the detection device, S the photon scattering rate, QE the quantum efficiency of the detection device and T the transmissive fraction of optical elements (lens, beam splitter, filter). Originally, the magnification factor of the setup was specified to be a factor of 20 (see (Mai06) section 2.1.1) which can be easily

¹see (Bro05) equation 3.164

quantified:

The full width of the camera image (128 pixels) covers approximately one segment of the trap ($\approx 250 \mu\text{m}$) and with a pixel size of $24 \times 24 \mu\text{m}$ one calculates the magnification factor $M \approx 12$. The discrepancy from the specified value is caused by a lens, placed in front of the camera to reduce the magnification, in order to get a higher signal on a smaller surface.

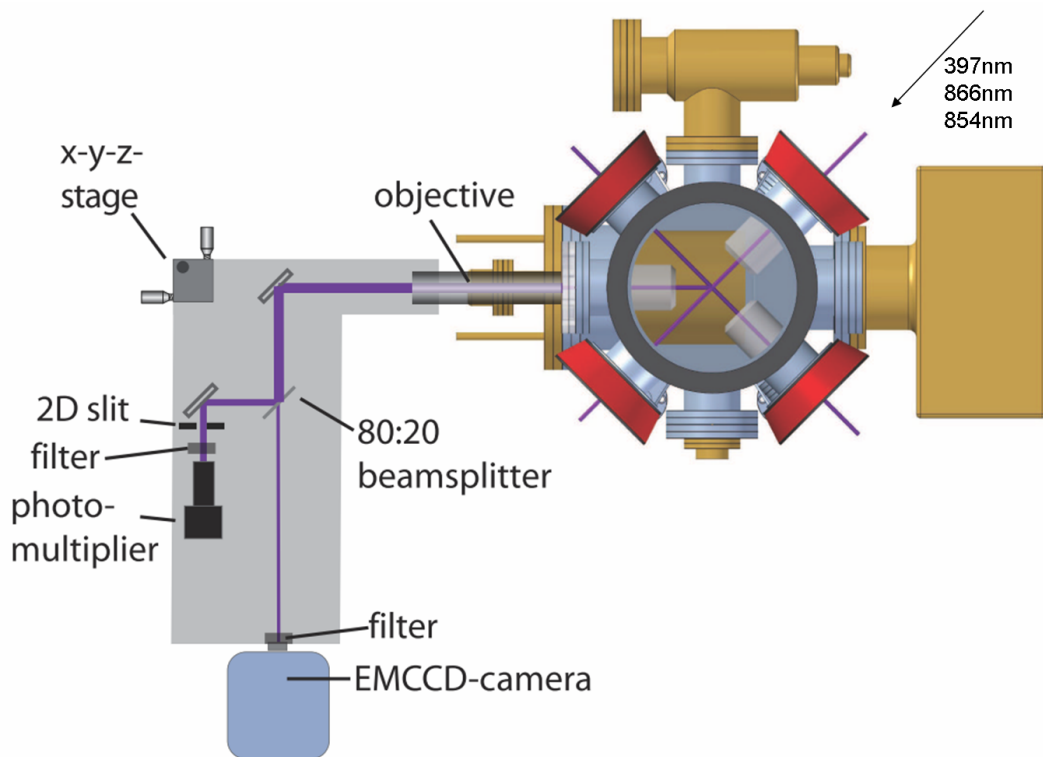
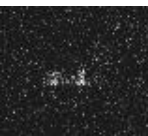


Figure 3.2: Top view scheme of the trap-apparatus, imaging and detection setup. Gray-shaded area indicates a box covering the PMT and camera from external light sources. The objective, mirrors and detection devices are mounted as a system and are moved by the x-y-z-stage.
Source: (Pos11)

A three-axis translation stage adjusts the focus and the observed segment on the micro trap. The 80:20¹ beam splitter² reflects 80% of the light to the Photomultiplier-Tube

¹Later we will see that these numbers are not generally valid

²Vendor unknown



3. DETECTION- AND READOUT SYSTEMS

(PMT) where a moveable 2D-slit¹ and an optical band-pass filter² for 397 nm wavelength reduces the background noise while the remaining 20% are transmitted to the EMCCD-camera where the light is filtered with an identical band-pass as for the PMT. The beam-splitter is mounted on a magnetic foot and can be easily removed for measurements requiring higher count rates at the camera. The details of the trap-apparatus itself can be found in (Sch09). The top view of the setup is shown in figure 3.2.

EMCCD Camera

In the experiment we use an Andor iXon^{EM} DV860 back-illuminated EMCCD camera with a total resolution of 128x128 pixels and a pixel-size of 24x24 μm . It utilizes a unique electron multiplying³ structure that is built onto the silicon-chip enabling charge from each pixel to be multiplied on the sensor before it is read out, while utilizing the full QE performance of the CCD sensor (see figure 3.3). The electron multiplication

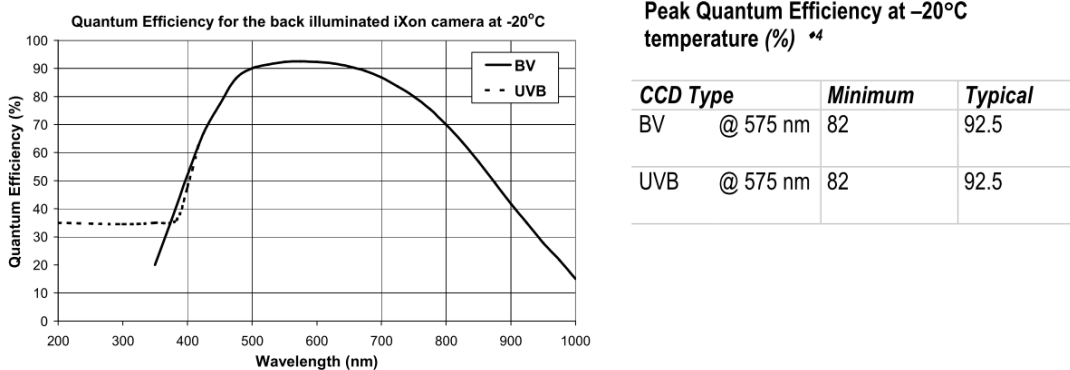


Figure 3.3: Quantum efficiency of the iXon CCD cameras extracted from tech-sheet. See (And06) for more information.

register is an additional shifting register where amplification occurs prior to readout by the charge amplifier. The electrode voltage of this register is adjusted in a way that avalanche multiplication of electrons occur while the charge is shifted from each segment of the register. Typically, the voltage is adjusted to a value where with each shift, the probability p of each initial electron to produce an additional electron is 0.01 – 0.02 resulting in a mean gain $g = (1 + p)^r$ where r is the size of the EM register.

¹Owis GmbH, Staufen, Germany

²Semrock, Rochester, USA. Model: FF01-377/50-23.7-D

³Electron multiplication amplification is responsible for the 'EM' in the EMCCD.

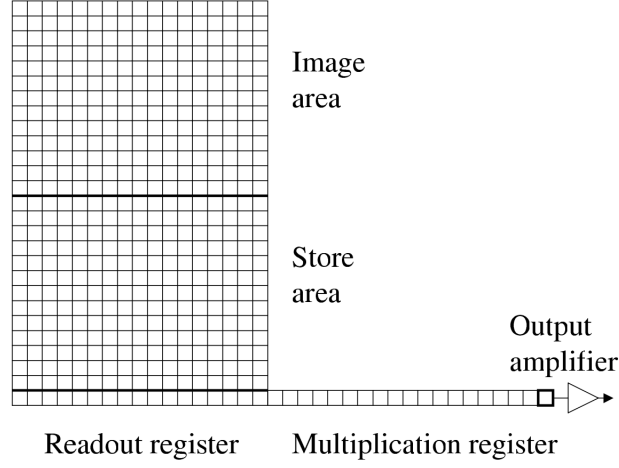


Figure 3.4: A schematic of an amplification register. Source: (BHM03)

Since the probability to produce an extra electron is small the size of EM register is significant. The probability distribution for an electron multiplication device with r elements in the multiplication register is given by (MTS85):

$$\begin{aligned}
 p_r(x) &= (1 - P) p_{r-1}(x) \\
 &\quad + P \sum_{k=0}^x p_{r-1}(x - k) p_{r-1}(k), \quad x, r \geq 1 \\
 p_r(0) &= 0, \quad r \geq 1 \\
 p_0(x) &= \delta_{1,x}, \quad r \geq 1
 \end{aligned} \tag{3.3}$$

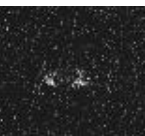
where P is the probability to produce an additional electron at each stage.

Assuming a large r and small P equation 3.13 can be approximated to:

$$P_1 = g^{-1} \exp(-xg^{-1}) \tag{3.4}$$

where $P_1(x)$ signifies the probability of the output for a single electron to be found x (BHM03).

To generalize the probability for $2..n$ input electrons a convolution of equation 3.4 with



3. DETECTION- AND READOUT SYSTEMS

itself can be done and iterated for a given number of input electrons:

$$\begin{aligned}
 P_2(x) &= \sum_{c=2}^x g^{-2} \exp(-cg^{-1}) \exp[-(x-c)g^{-1}] \\
 &= g^{-2}(x-1) \exp(-xg^{-1}) \\
 P_3(x) &= \frac{(x-2)(x+1) \exp(-xg^{-1})}{g^3 2!} \\
 &\vdots \\
 P_n(x) &= \frac{x^{n-1} \exp(-xg^{-1})}{g^n (n-1)!}
 \end{aligned} \tag{3.5}$$

where $P_n(x)$ is valid from $x \geq n$ (BHM03). The expectation value and variance are calculated to be $\langle P \rangle = ng$ and $\sigma = ng^2$.

Providing equation 3.5 with a Poisson probability distribution of the input photons one can calculate:

$$p(x, \mu) = \sum_{n=1}^{\infty} \frac{\exp(-\mu - x/g) \mu^n (x/g)^{n-1}}{g(n-1)! n!} \tag{3.6}$$

allowing one to estimate the mean gain g and the mean light level μ photon pixel⁻¹. Applying a fit of this function to a given (bright) pixel distribution allows one to estimate the gain of the EM register on the CCD chip (BHM03).

The CCD chip itself is placed in vacuum and can be cooled down to -70 °C using a Peltier-cooler, efficiently reducing noise arising from dark counts¹. Background counts are dominated by camera clock-induced charge readout noise rather than scattered light. The full CCD-chip can be read out at up to 2 kHz. Faster rates of up to 10 kHz can be reached using sub-imaging and on-chip binning of the pixels.

Photomultiplier Tube

The P25PC photomultiplier tube used in the experiment is a photodetector module designed by Sens-Tech and configured for photon counting. It comprises a 25 mm diameter end window photomultiplier tube with a UV sensitive photocathode. Even though the QE is a factor of three smaller than that of a EMCCD camera, its low noise and low dark-count rate makes it a favorable detector if no spatial resolution is required. Since the PMT is designed for photon counting and has a fast response time it can be easily used for time resolved measurements (see (MSW⁺08)).

¹Noise from thermally generated electrons collected in the CCD contributing to the measured signal.

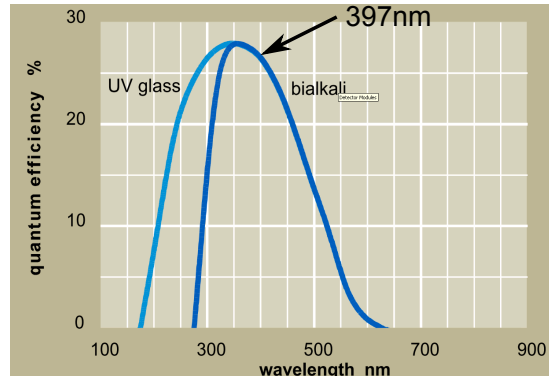


Figure 3.5: Quantum efficiency of the PMT extracted from tech-sheet. Source: (Sen10)

Characterization of the Beam Splitter

In the future, one could think of experiments requiring a combination of the CCD- and PMT detector (e.g. time resolved measurements using spatial resolution of the CCD while having the advantageous time-response behavior of the PMT), and since both detectors share one photon source, the precise fraction of the beam-splitter is of interest.

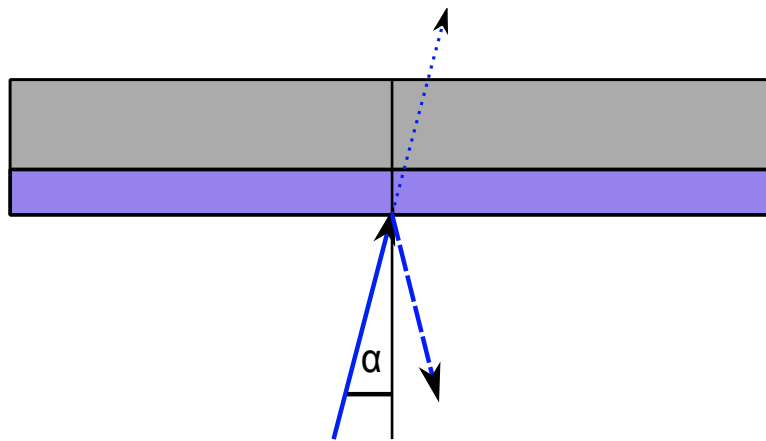
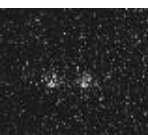


Figure 3.6: Schematic of the beam splitter. Blue shaded area represents the coating material.

The resulting curves shown in figure 3.7 point out that the 80:20 branching is only valid if the beam is adjusted perpendicularly with respect to the splitter. This can be explained as follows; varying the angle of the beam changes the distance the light



3. DETECTION- AND READOUT SYSTEMS

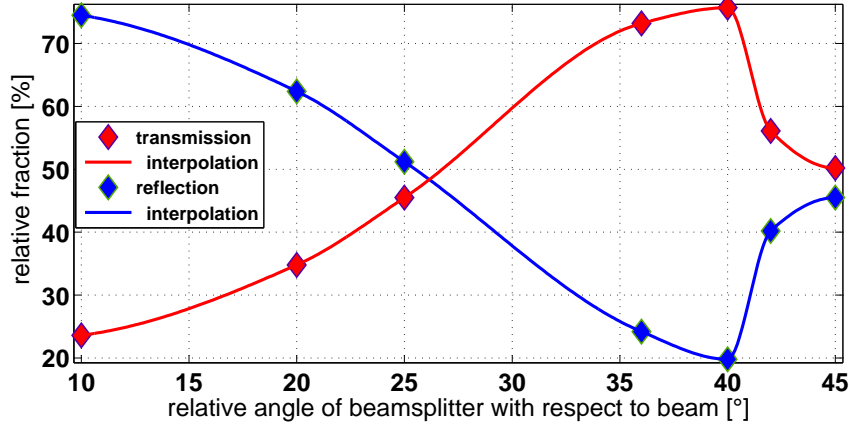


Figure 3.7: Reflection / transmission measurement of the beam splitter in the detection branch. The polarization does not change the behavior of the beam splitter and therefore was omitted.

has to travel through coating medium. The effective distance $d' = \frac{d}{\cos(\alpha)}$ drastically changes the behavior of the beam splitter up to a point where it behaves inverse to its specifications.

Since the experiment does not use a power-meter a verification was done using the CCD camera. Two series of 50.000 ion images were taken at an exposure time $t_e = 5 \text{ ms}$ - one with, one without the beam-splitter. To reduce the fluctuations of the count rates from different images arising from different noise sources (shot-noise, dark noise etc.), the series of images were averaged. The averaged count rate of the resulting images can be used to calculate the fraction of light being transmitted through the beam splitter. To decrease the noise offset the images were fitted with a 2D Gaussian:

$$z(x, y) = y_0 + Ae^{-\left(\frac{x-x_c}{s_1}\right)^2 - \left(\frac{y-y_c}{s_2}\right)^2} \quad (3.7)$$

The offset values were found to be $y_1 = 1035 \pm 4$ for the series with- and $y_2 = 1010 \pm 2$ for the series without the beam splitter and subtracted from the averaged images $c_{1/2}(x, y) = p_{1/2}(x, y) - y_{1/2}$, where $p_{1/2}(x, y)$ is the averaged pixel count rate at a given x and y coordinate of data set 1 and 2 respectively. The background- and scattered light cannot be the major source of the high count rates since a histogram on a single pixel level reveal that the minimum counts detected in dark ambient are in the order of magnitude of ≈ 900 counts as one can tell from figure 3.8. The high offset in count rates must originate from a hardware offset of the camera: *maybe to make sure the count*

rate output of the camera is always positive or due to miscalibration (contact person LOT Oriel).

Sum of counts $I = \sum_{x,y \in \text{image}} c(x,y)$ are found to be:

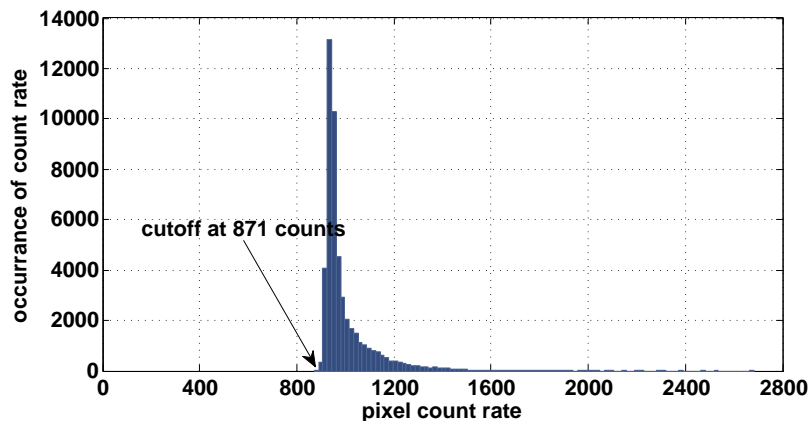


Figure 3.8: A histogram of a dark noise measurement at 3 ms exposure time with a total set of 50.000 images on a single pixel.

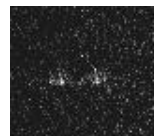
$I_1 = 6479 \pm 267$ and $I_2 = 20662 \pm 803$ leading to $31 : 69(\pm 1)$ branching ratio of the beam splitter. This value seems reasonable as the the plate is mounted at an angle $\alpha \approx 15^\circ$.

3.2 Detection Algorithms

As mentioned in previous chapter, the readout of atomic qubit states is usually done by measuring resonance fluorescence light, and for a single qubit one is interested in a map

$$A : \{\text{measured signal}\} \longrightarrow \{0, 1\} \quad (3.8)$$

to distinguish the qubit state. Depending on the type of the detector the measured signal provides one with either time resolved information (PMT) or spatial information (CCD) which can be additionally taken into account to map the signal onto $\{0,1\}$ improving the classification result (MSW⁺08). Here the PMT is used as an integrating detector in a defined time window with neglected time information and the measured signal is classified into two classes depending on amount of photons counted using



3. DETECTION- AND READOUT SYSTEMS

threshold σ .

$$A : \{\text{measured signal}\} \rightarrow \left\{ \begin{array}{l} < \sigma \rightarrow \text{'dark'} \\ \geq \sigma \rightarrow \text{'bright'} \end{array} \right\} \hat{=} \{0, 1\} \quad (3.9)$$

Since one is interested in a threshold σ to map the PMT count rates to a binary value $v \in \{0, 1\}$, the ion needs to be primed in both states (fluorescing('bright') and non-fluorescing('dark')) and measured. To achieve that, a sequence is employed where the near 397 nm readout lasers is generally enabled while the repump laser near 866 nm is turned on or off during a PMT readout (see figure 3.9). This sequence is typically repeated numerous times, since the statistical nature of source and the noise of the detector lead to count-rate fluctuations. To reduce the impact of noise and background which mainly arises from scattered laser light of the micro trap¹, the slit in front of the PMT is adjusted in a way that the signal-to-noise ratio (SNR) is maximized², reducing the exposed area to a tiny square where mainly the fluorescence light impinges.

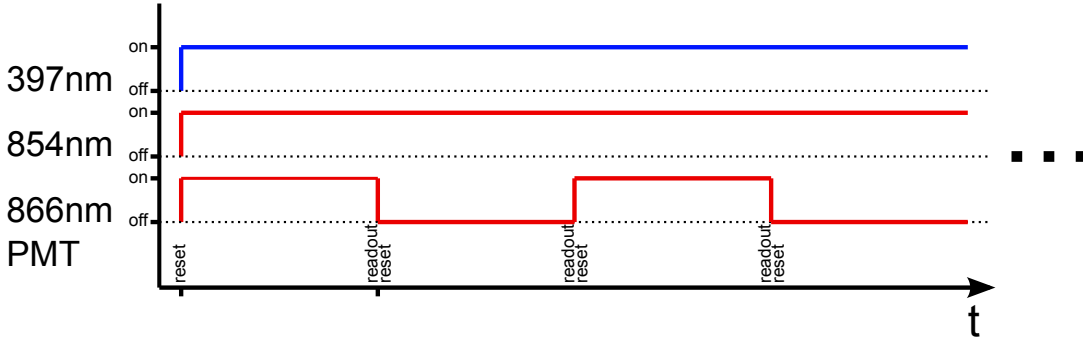


Figure 3.9: Sequence to take signals of alternating 'bright' and 'dark' ion to distinguish the threshold σ .

Doing the 'readout' of the ion in that way slightly differs from the actual experiment as during the readout phase the 866 nm laser is always enabled while the quenching 854 nm laser is always disabled. This results in a minor change of the background noise as the scattered 866 nm light is not fully absorbed by the 397 nm filters in front of the PMT. By preparing the states in that way we further neglect spontaneous decay from $D_{5/2}$ which mean lifetime is limited to ≈ 1 s since we are primary interested in the goodness of the algorithms. Binning the signal, knowing that every second signal is

¹Scattered laser light is a common problem of micro-fabricated Paul traps.

²see 'diffmode' scan in the software

supposed to be 'bright' allows one to calculate¹ an optimum threshold $\sigma = \sqrt{\bar{n}\bar{s}}$ for classification where \bar{n} and \bar{s} are the average counted photon number for distributions 'bright' and 'dark'. The result of PMT discrimination is displayed in figure 3.10.

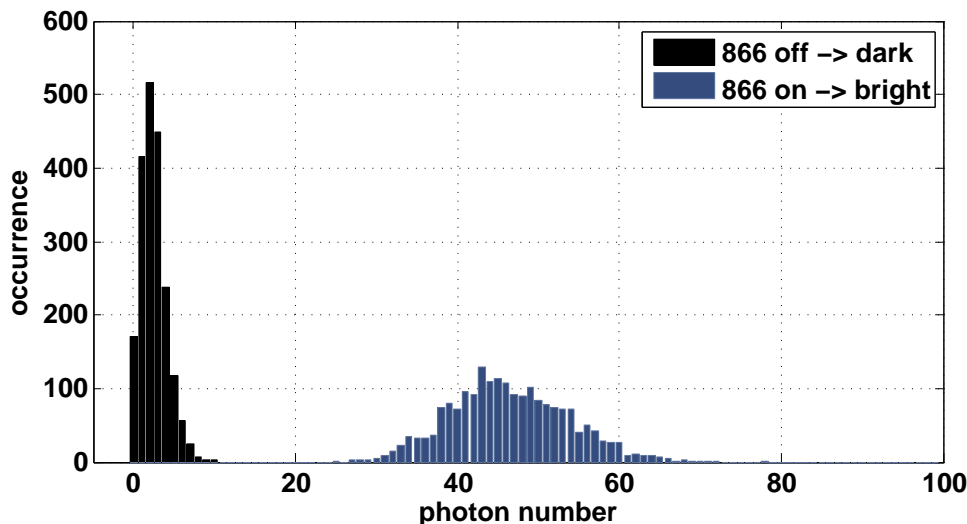
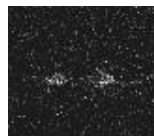


Figure 3.10: PMT histogram taken at an exposure time $t_e = 2$ ms with a 397nm laser-power $P = 160 \mu\text{W}$ with a set of 2000 bright and 2000 dark signals.

In analogy to this technique one can process the camera image in a way where only a small rectangle around the ion is contributing to the signal by summing pixel-values of the CCD-image in a region-of-interest (ROI). Data is acquired in the same way as described above for the PMT readout. Sets of 'bright' and 'dark' images with a resolution of 10x14 pixel were taken at different exposure times $t_e = \{1, 2, 3\}$ ms at 397 nm laser power of $\approx 160 \mu\text{W}$, each having 50.000 images. An example image from each set can be found in figure 3.11. After calculating the total count-rates within a ROI: $I = \sum_{p \in \text{ROI}} p$ and binning the result, the threshold σ for classification can be obtained in the same way as described for the PMT (see figure 3.12). Still, the results of the algorithm are found to be suboptimal (see results in table 3.1) and a comparison of the spacing between the 'bright' and 'dark' histograms of PMT and CCD (figures 3.12 and 3.10) clarify that the PMT, even though it has a lower QE, has a better SNR resulting in a better discrimination at same exposure time. In the following, several

¹see appendix of (Roo00)



3. DETECTION- AND READOUT SYSTEMS

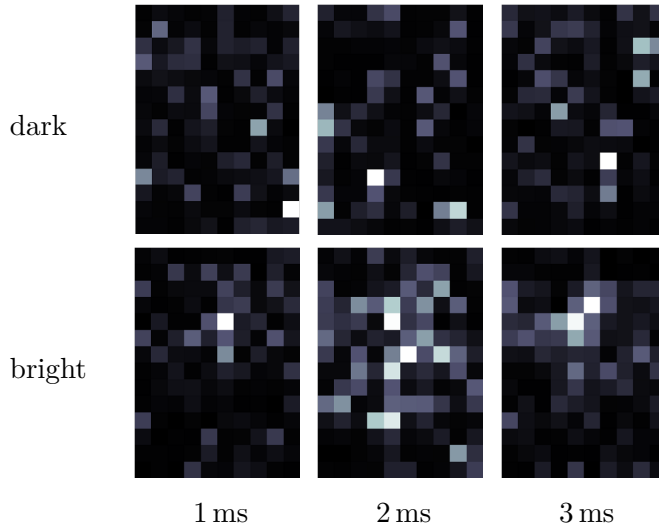


Figure 3.11: Sample images from each dataset (14x10 pixel).

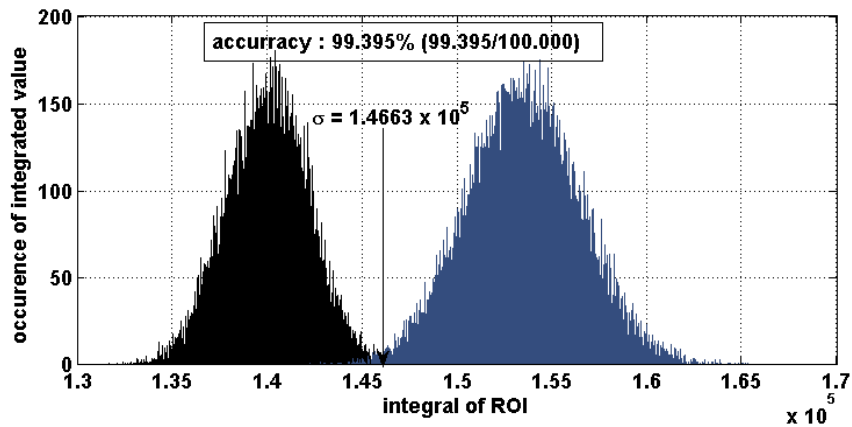


Figure 3.12: A histogram based on integrated pixel-counts of the camera image at $t_{\text{exp}} = 2 \text{ ms}$ and calculated threshold σ value. Note that compared to the PMT the discrimination result is worse.

methods using the spatial information of the CCD camera are presented in order to increase SNR and therefore the classification accuracy.

Pixels of Interest

Obviously, the ion image is not rectangular and using the simple ROI algorithm we reduce the SNR by summing over the edges of the ROI which carry no useful informa-

t_{exp}	bare classification accuracy[%]
$1\mu\text{s}$	91.225
$2\mu\text{s}$	99.395
$3\mu\text{s}$	99.956

Table 3.1: Results of the simple ROI algorithm using the camera at different exposure times. The non-linearity of the classification at different exposure times arises from the fact that the distributions bright and dark merge.

tion. Instead of defining a region as a rectangular surface around the ion we can define it by the brightest pixels. To identify the pixels where most of the light impinges and to avoid a high impact of count rate fluctuations arising from noise and the Poissonian count statistics of each pixel, a reference image at long (≈ 50 ms) exposure time needs to be employed. Sorting the pixels of this image in a descending order beginning with the highest count rates and storing its coordinates, allows us to define a ROI consisting of pixels carrying most of the information (e.g. 10 brightest pixels). Figure 3.13 shows the image used for the algorithm with its variable ROI set.

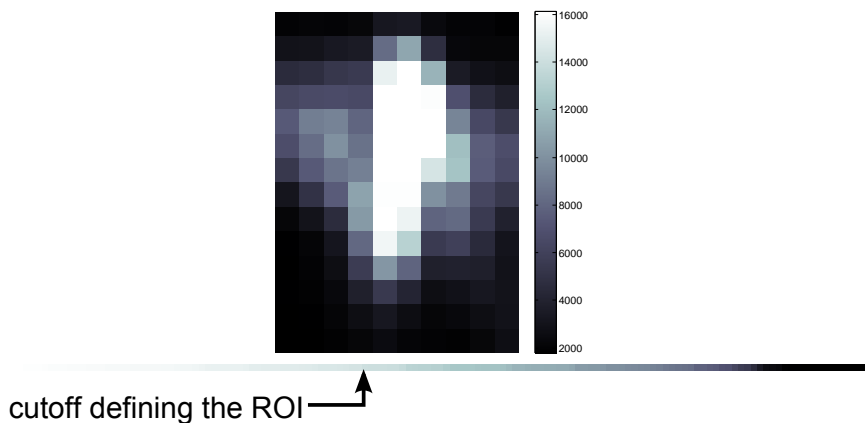
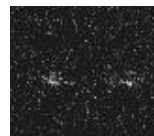


Figure 3.13: Definition of ROI consisting of the brightest pixels of the image.

From here the procedure is the same as for the simple square-shaped ROI algorithm. The sum is taking only those pixels into account which are included in the ROI set. As one can tell from figure 3.14, this algorithm provides a much better classification results, but its optimum strongly depends on the cutoff of ROI which needs to be adjusted manually and the algorithm itself cannot be easily extended on a multi-qubit setting.



3. DETECTION- AND READOUT SYSTEMS

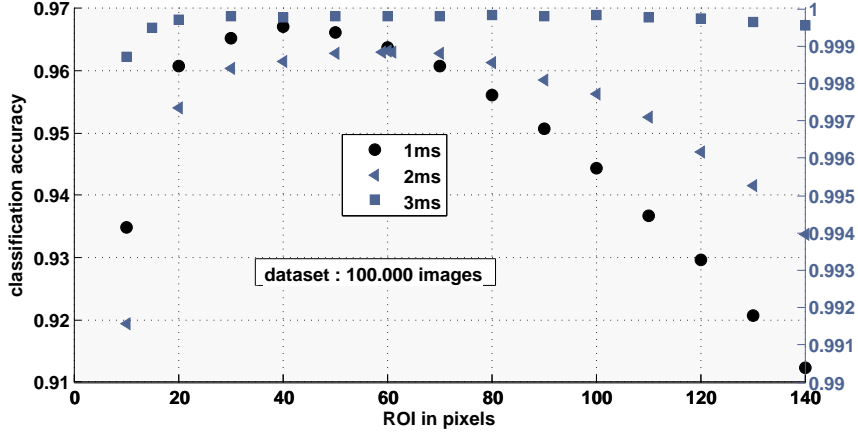


Figure 3.14: Classification results depending on the amount of pixels included to the ROI set. Two different y-axes were defined, the color of the data points matches to the color of the corresponding axis.

Giving a Pixel a Weight

Another way of employing the spatial information of the signal is to provide each pixel with a weight. Pixels carrying little information should contribute less to the sum than pixels carrying more information (e.g. higher count-rates). A simple way of realizing this is calculating a mask which needs to be overlapped with each image taken by the camera. One way of calculating a suitable mask is taking an image with long exposure and fitting a 2D Gaussian (see figure 3.15). The resulting fit parameters can be used to calculate a mask $M(x,y) = e^{-\frac{(x-x_c)^2}{s_1^2} - \frac{(y-y_c)^2}{s_2^2}}$ with $(x,y) \in \text{Image}$, which can be used to weight each pixel in the sum $I = \sum_{p \in \text{ROI}} M(x,y) \cdot p(x,y)$.

Due to imaging errors the shape of the ion image differs from a perfect Gaussian and for a single ion implementations one could think of using an adaptive mask taking the shape of the ion into account instead of fitting a Gaussian. Departure from an analytical calculated mask (e.g. Gaussian) thus will cause trouble trying to generalize this algorithm to a multi-qubit setting since in our setup it is not possible to individually illuminate only one ion in an ion crystal. A ten ion string for example would produce a single tube-like mask and in the case where only one out of the ten ions is bright, the mask would drastically reduce the SNR of this single, fluorescing ion. Since a Gaussian-shaped mask efficiently suppresses noise the algorithm is almost insensitive to variations of large ROI- and image size producing an overall good discrimination result (see figure

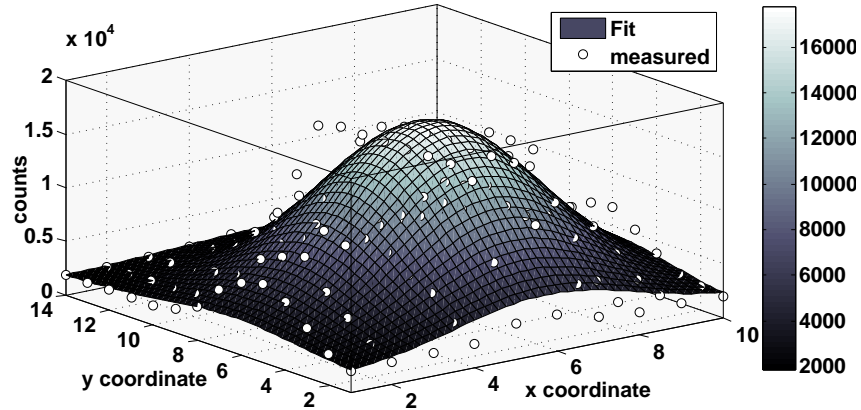


Figure 3.15: Fit applied to figure 3.14 providing the required parameters to calculate the mask $M(x,y)$.

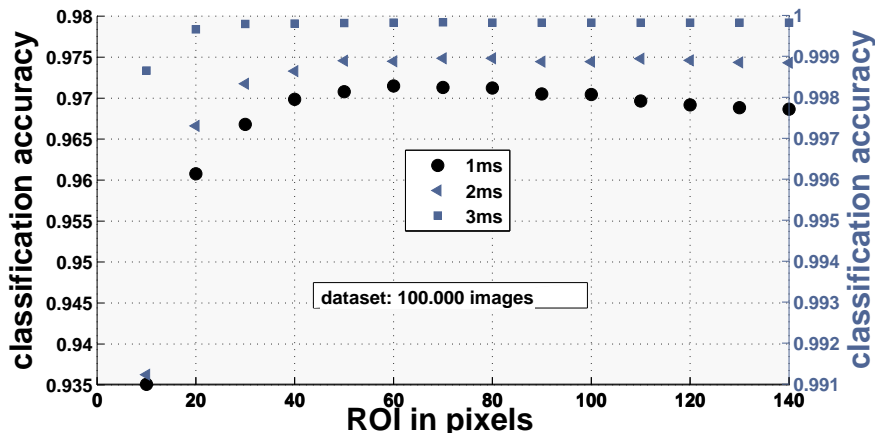


Figure 3.16: Classification results depending on the size of the ROI-set combined with a Gaussian mask. Note that the result is almost independent from the ROI-set. Two different y-axes were defined, the color of the data points matches to the color of the corresponding axis.

3.16). It further can be easily extended to a multi-qubit setting as we will see later.

Statistical Algorithm: Maximum Likelihood

Instead of reducing the entire image information to a single value of the integrated count value one could think of classification on the single pixel level. For long exposure time ($t_{\text{exp}} \approx 50 \text{ ms}$) it is possible to determine the qubit state based on count values from a single pixel. At short exposure times the distribution of count-rates 'bright' and



3. DETECTION- AND READOUT SYSTEMS

'dark' overlap, leading to significant discrimination errors (see figure:3.17). Instead of giving a binary result 'bright' or 'dark' one can provide each pixel value v with a value $p \in [0, 1]$ corresponding to its probability of being bright. To project v on its probability a map

$$A : (v \in \mathbb{N} | 0 \leq v \leq 2^{16})^R \longrightarrow (p \in [0, 1])^R \quad (3.10)$$

is required, where R is the number of pixels in an image.

Defining a distribution (histogram)

$$S(c) = \sum_{l=1}^N x_l(c) \quad (3.11)$$

for each pixel, where N is the image number and

$$x_l(c) = \begin{cases} 1 & \text{if pixel value } v = c \\ 0 & \text{else} \end{cases} \quad (3.12)$$

allows us to calculate S_{bright} and S_{dark} distributions based on the two image sets leading to a probability distribution

$$p_{x,y}(c) = \frac{S_{x,y,\text{bright}}(c)}{S_{x,y,\text{bright}}(c) + S_{x,y,\text{dark}}(c)} \quad (3.13)$$

for each pixel to be bright¹. This probability distribution of an image allows us to define a map

$$B : (p(c))^R \longrightarrow \{0, 1\} = \{\text{dark}, \text{bright}\} \quad (3.14)$$

To determine the distribution of each pixel we require a set of images to build up the statistics (see figure3.17). Here, a set of 50.000 images from each class, bright and dark, was used. Based on the histograms of each pixel a probability distribution can be calculated which assigns each count value of a pixel a given probability to be bright. If the distribution of count-rates can be accessed analytically (e.g. fitting) the probability distribution can be stored as a set of parameters, otherwise a look-up-table for each pixel can be generated. In this case we used a look-up-table as the recorded data is sufficient to build up good statistics.

Since pixels not illuminated with fluorescence light cannot provide any information

¹The probability to be dark can be obtained in a similar way

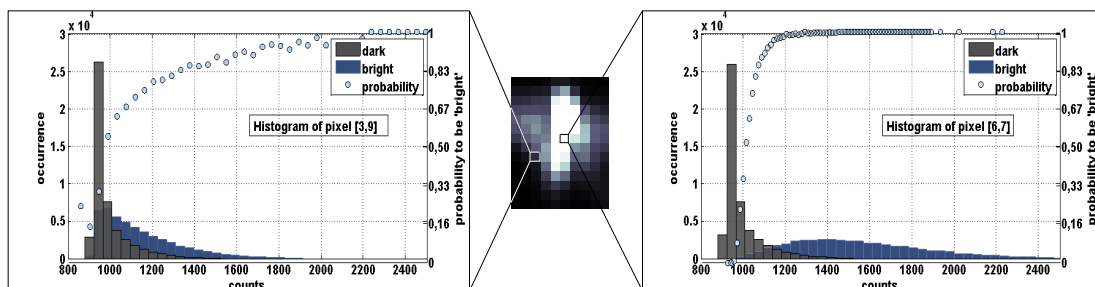


Figure 3.17: Description of the algorithm based on a dataset of 100.000 images at an exposure time $t_{\text{exp}} = 3$ ms. To point out the difference a hardly illuminated pixel is compared to a bright pixel.

whether the ion is dark or bright, its probability to be bright results in $p = 0.5$ (see edges of the probability image in figure 3.18). This result can also be obtained analytically using equation 3.13, assuming same distributions S_{bright} and S_{dark} .

The map $A : v(x, y) \rightarrow p(x, y) \in [0, 1]$ allows us to estimate the state of the qubit putting a threshold at $\sigma = 0.5$ for the mean probability $\bar{p} = \frac{1}{R} \sum_{p \in \text{Image}} p$.

$$B : \bar{p} \begin{cases} \geq 0.5 & \rightarrow \text{'bright' } \\ < 0.5 & \rightarrow \text{'dark' } \end{cases} \quad (3.15)$$

This is justified as pixels carrying no information result in a probability $p = 0.5$ and the value set of p is enclosed $p \in [0, 1]$. The error $\Delta\bar{p}$ can be estimated assuming each pixel being independent and using Gaussian error propagation.

$$\begin{aligned} \Delta\bar{p} &= \sqrt{\left(\frac{\partial\bar{p}}{\partial p_1} \Delta p_1\right)^2 + \left(\frac{\partial\bar{p}}{\partial p_2} \Delta p_2\right)^2 + \dots} \\ &= \sqrt{\frac{1}{N} \cdot \sum_{i=1}^N (\Delta p_i)^2} \end{aligned} \quad (3.16)$$

Further, assuming an upper limit for the error $\Delta p_i = \Delta p_{\text{max}}$ of each pixel to be constant one finds a coarse approximation for the resulting error $\Delta\bar{p} = \Delta p_{\text{max}}$. The result of the algorithm displayed in figure 3.19 is found to provide the best results so far. Still, to achieve good results using numerical calculations of probability distribution a large set of data needs to be acquired and since each pixel has its unique distribution the classification accuracy highly depends on ions position. In this evaluation no cross-correlations between pixels were taken into account. One could think of cross-correlation methods



3. DETECTION- AND READOUT SYSTEMS

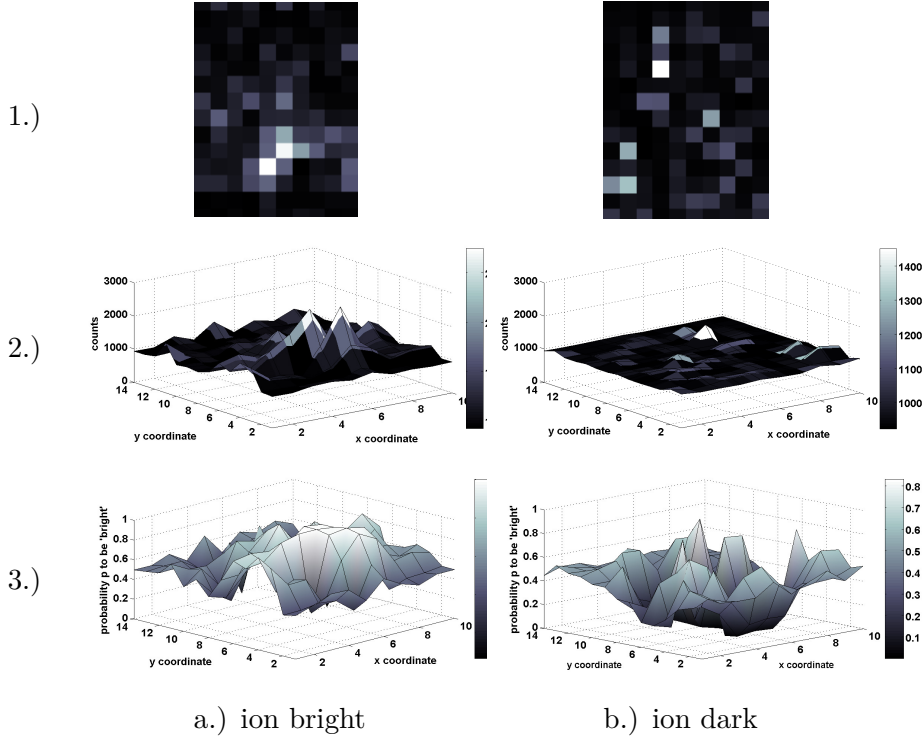


Figure 3.18: From count rates to probability distribution of two images taken at 3ms exposure time. 1.) Show the 2D images of the bright and dark ion, respectively (count value encoded into brightness of pixel). 2.) 3D landscape plot corresponding to 1. 3.) Probability landscape plot. Note that the dark image produces a dip as its the probability to be bright is low.

and a combination of so far introduced techniques to further improve the results of this algorithm. Another method to achieve a discrimination based on probabilities, is to calculate two numbers- one for being bright and one for being dark:

$$\begin{aligned}
 N_{\text{bright}} &= \prod_{p \in \text{Image}} p \\
 N_{\text{dark}} &= \prod_{p \in \text{Image}} (1 - p)
 \end{aligned}
 \tag{3.17}$$

The bigger number indicates to which class an image most likely fits. In this method the 'bad pixels', which carry no information, have no negative effect on the result since they contribute to the product of both numbers equally. The results of this classification method are i) 97.854% for 1 ms, ii) 99.827% for 2 ms and iii) 99.990% for 3 ms which are similar to the previous method.

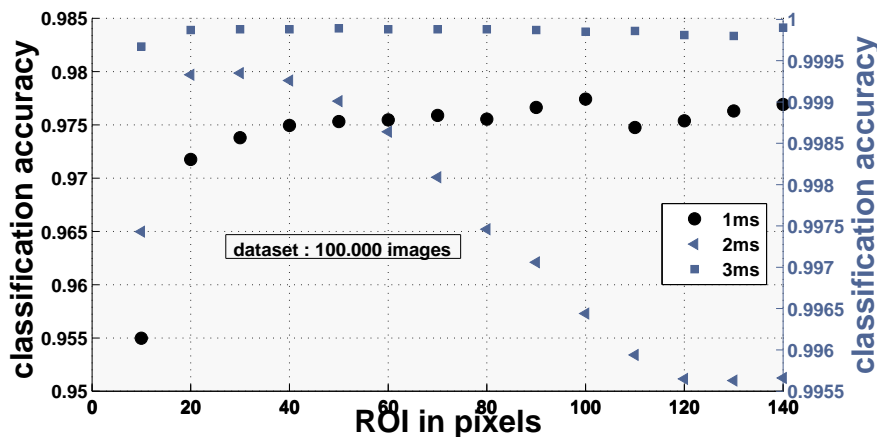


Figure 3.19: Results of the 'Maximum likelihood' algorithm. Note that for the 2ms points the maximum discrimination accuracy is reached for smaller ROI-sets compared to other algorithms indicating that the algorithm more efficiently uses the pixel information. The drop in accuracy is the result of the threshold $\sigma = 0.5$ since pixels carrying no information have a probability $p = 0.5$ to be bright and a simple averaging reduces the SNR.

Machine Learning: Support Vector Machine

The Support-Vector-Machine belongs to the category of 'learning algorithms'. It separates (classifies) data described by a set of G parameters into two classes using a (hyper)plane with the condition of maximal spacing between each class and the (hyper)plane (Mar03).

$$H := \{x \in \mathbb{R}^G | \langle w, x \rangle + b = 0\} \quad (3.18)$$

To specify the separating (hyper)plane the algorithm needs to be provided with a set of *training* data which have to be taken under same conditions as the *real* data. Furthermore the membership of each training set must be known in order to find the best separating plane. Once the parameters b and w are set, any data taken under same conditions can distinctly be assigned to a corresponding class. In this evaluation each set ('bright' and 'dark') is based on the fluorescence level of each pixel, resulting in a 140-dimensional space for hyperplane calculation. A significant advantage of this algorithm is the fact that it calculates the separating plane maximizing the gap between the provided training set, resulting in a high accuracy even using a small set of training data (see figure 3.20). Still, this algorithm has disadvantages compared to the algorithms using a mask and a threshold.



3. DETECTION- AND READOUT SYSTEMS

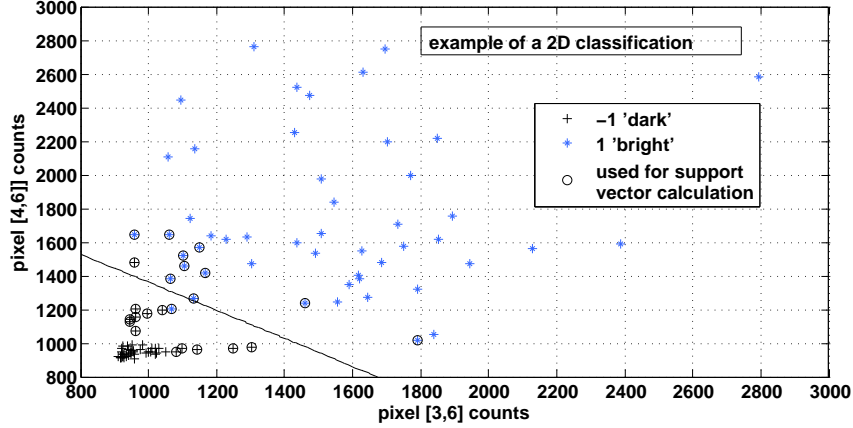


Figure 3.20: A 2D 'support vector' calculation based on a set of 100 images taken at an exposure time $t_{\text{exp}} = 3$ ms. To visualize the result only two pixels were taken to calculate the separating plane (indicated by the line).

- the accuracy of classification is highly dependent from the training dataset (see figure 3.21).
- the algorithm a priori is limited to two classes¹ therefore an extension to multi-qubit setting is challenging.
- it is not always possible to obtain a training set under experimental conditions with known membership. Other so far introduced algorithms do not require the membership.

Summary

All demonstrated algorithms can significantly improve the accuracy of the classification. As already mentioned, the data was acquired in a way that the spontaneous decay of the metastable $D_{5/2}$ state could be neglected which is no longer valid during real sequences used in the experiment. Further, the shelving efficiency to the $D_{5/2}$ state is limited. Therefore the total discrimination efficiency needs to take these predominant effects into account. Here only the bare classification accuracy of the algorithms is investigated. Still, some of the techniques are not easily applicable to future requirements of the experiment. The key criteria to the algorithm are accurate classification

¹A combination of separating planes can be used to handle this problem.

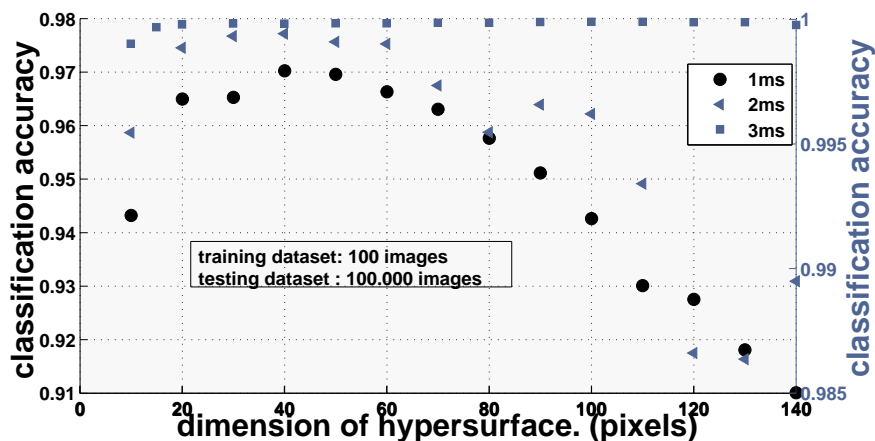
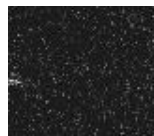


Figure 3.21: Results of the 'support vector machine' algorithm. Note that with the amount of pixel the classification accuracy decrease, since more not illuminated pixels have to be considered by the algorithm resulting in a different (worse) separating hyper-plane.

	1 ms[%]	2 ms[%]	3 ms[%]	ROI dependent	multi-ion	preparation effort
ROI	96.715	99.887	99.983	yes	challenging	simple
MASK	97.149	99.895	99.983	no	simple	medium
ML	97.743	99.935	99.990	partial	medium	high
SVM	97.025	99.943	99.991	yes	challenging	simple

Table 3.2: Summary of the classification algorithms providing additional information on its dependency of ROI-set, extendability to multi-ion setup, and the preparation complexity. Note that since no post-selection of data was done, all the results are in principle limited by the fact that the ion by chance has got hot, resulting in little count-rates and therefore is assigned into 'wrong' class.

and simple preparation for the actual experiment paired with the necessity of being able to extend the algorithm on a multi-ion system. The algorithm using a Gaussian mask to weight the pixels seems as the most promising one. It requires a fitting routine and a small set of images to determine a threshold to map integrated pixel-values on a binary state. Further, it is almost independent from a ROI-set and therefore independent from the size of the image and achieves good classification results. In the next paragraph a two-ion classification using a Gaussian mask is demonstrated.



3.3 Two Ion Discrimination at 3 ms Timescale with 99.999% Algorithm-Fidelity

The preparation for a two ion discrimination is similar to the single ion discrimination using a Gaussian mask. An image of a two ion crystal is taken at a long exposure time (20 ms) and fitted with two overlapping Gaussian distributions (see figure 3.22).

$$z(x, y) = y_0 + A \left(e^{-\left(\frac{x-x_{c,1}}{s_1}\right)^2 - \left(\frac{y-y_{c,1}}{s_2}\right)^2} + e^{-\left(\frac{x-x_{c,2}}{s_1}\right)^2 - \left(\frac{y-y_{c,2}}{s_2}\right)^2} \right) \quad (3.19)$$

Here, equal amplitudes A and widths s_1 and s_2 are chosen for the sake of simplicity. The

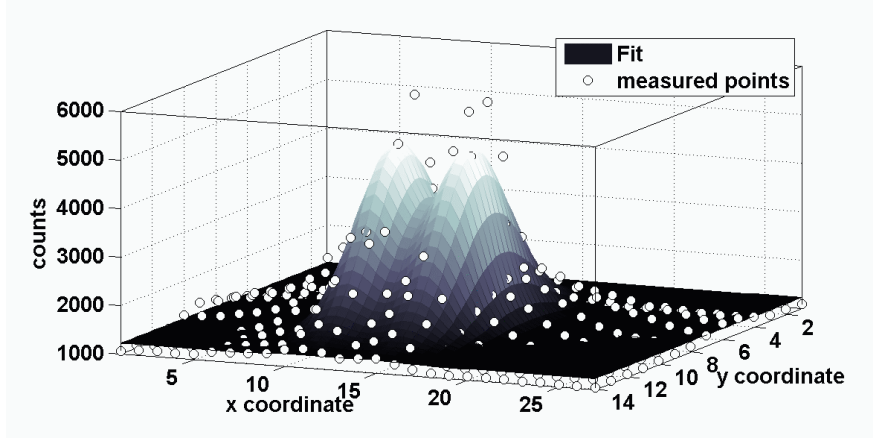


Figure 3.22: Fitting result of a two ion crystal.

resulting fit parameters are used to calculate two masks:

$$\begin{aligned} M_1(x, y) &= e^{-\left(\frac{x-x_{c,1}}{s_1}\right)^2 - \left(\frac{y-y_{c,1}}{s_2}\right)^2} \\ M_2(x, y) &= e^{-\left(\frac{x-x_{c,2}}{s_1}\right)^2 - \left(\frac{y-y_{c,2}}{s_2}\right)^2} \end{aligned} \quad (3.20)$$

Since an individual addressing of the ions is not possible and a deterministic preparation can be done either 'all ions dark' or 'all ions bright' (used for Gaussian fitting), we have to take into account that individual Gaussian masks merely *suppress* the impact of the neighboring ion's light. This results in an overall shift of count rates to higher values with the consequence of a slightly different determination of the threshold σ . Further, cases where only one of the ions is bright (and the neighbors are dark) will result in lower count-rates and therefore might get assigned to a wrong class. To take

3.3 Two Ion Discrimination at 3 ms Timescale with 99.999% Algorithm-Fidelity

this into account, the impact of the neighboring ion's light needs to be subtracted from the image of the examined ion. For a two ion crystal, observing the left ion, one has to subtract the impact of the right ion's light and vice versa. Since these operations change the image they need to be applied to both sets of data - bright and dark (see figure 3.23 for examples).

$$\begin{aligned} \text{Img}'(x, y) &= \text{Img}(x, y) \cdot \text{Mask}_{\text{Right}}(x, y) \\ \text{Img}_{\text{Left}}(x, y) &= \{\text{Img}(x, y) - \text{Img}'(x, y)\} \cdot \text{Mask}_{\text{Left}}(x, y) \end{aligned} \quad (3.21)$$

$$\begin{aligned} \text{Img}''(x, y) &= \text{Img}(x, y) \cdot \text{Mask}_{\text{Left}}(x, y) \\ \text{Img}_{\text{Right}}(x, y) &= \{\text{Img}(x, y) - \text{Img}''(x, y)\} \cdot \text{Mask}_{\text{Right}}(x, y) \end{aligned} \quad (3.22)$$

Applying this technique on a set of 'bright' and 'dark' images one obtains four new sets of images (a dark- and a bright set for each ion) or generally $2N$ where N is the number of ions. Binning the sum of each image of the set allows one to determine a threshold σ_n for each ion to map its state onto $\{0,1\}$ where n is the ion's number.

To estimate the classification error of the algorithm the histograms 3.24 were fitted with Gaussian distribution and using the thresholds σ_1 and σ_2 the classification errors are found to be $\Delta_{\text{Left}} = 99.9991\%$ and $\Delta_{\text{Right}} = 99.9989\%$ leading to a an overall classification accuracy of 99.999%. One can improve the result at least one order of magnitude by using the fitted curves and search for an overall minimum of both distributions and calculate optimal thresholds $\sigma_{1,2}$. Another limitation in actual experiment is the spontaneous decay of the metastable $D_{5/2}$ state. At an exposure time of $t_e = 3$ ms one calculates that the total goodness of discrimination is limited by the spontaneous decay to $\approx 99.7\%$. To reduce the impact of the limiting factor, the exposure time needs to be reduced. See (MSW⁺08) for general limitation at different exposure times. To further test the algorithm the 854 nm laser was disabled and the 729 nm laser was enabled at low power to *slowly* drive the $S_{1/2} \longleftrightarrow D_{5/2}$ transition resulting in a random 'blinking' of the two ions. Higher laser power would result in faster transitions, ultimately 'dimming' the ion's light since the camera would see a time-averaged fluorescence signal of a bright and a dark ion. A set of 20.000 images was taken at 3 ms exposure time and processed through the described algorithm. Since the 'blinking' sequence is random, the verification cannot be done automatically. A subset of 100 images was checked manually with an 100% match with the algorithm (see figures 3.26 and 3.27).



3. DETECTION- AND READOUT SYSTEMS

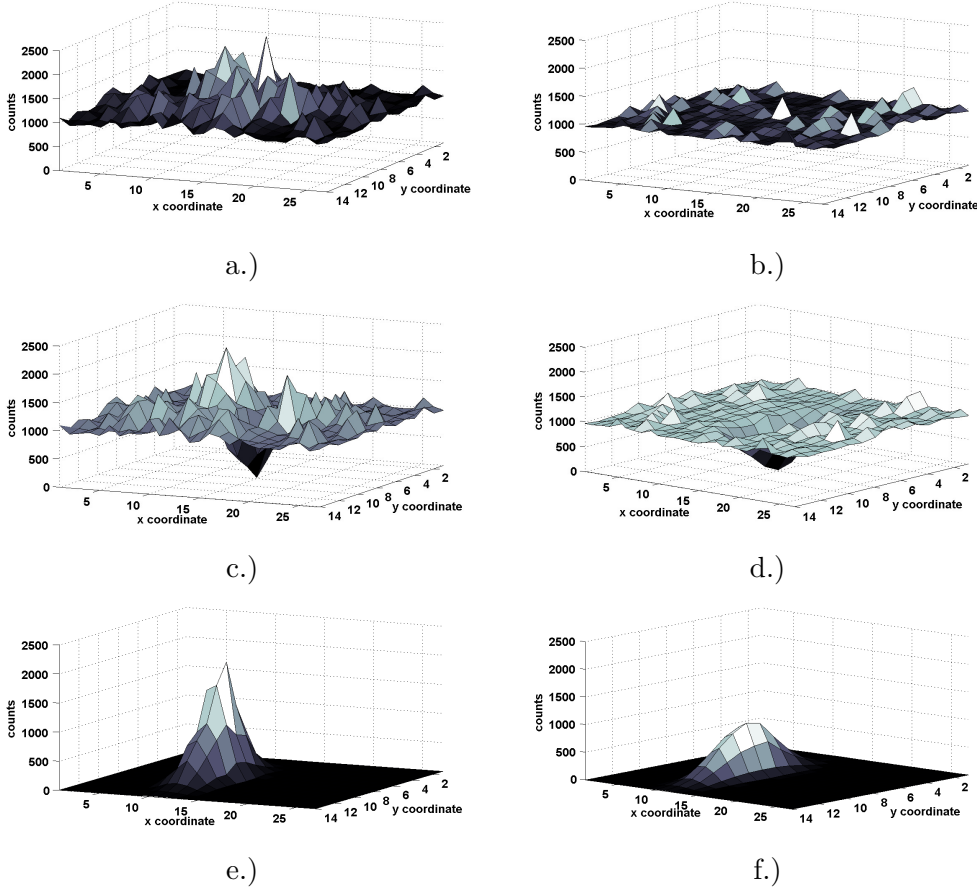


Figure 3.23: A two-step procedure to obtain a single, weighted profile of the left ion. a.) and b.) show an example of deterministic primed states, both bright and both dark, respectively. c.) and d.) show a.) and b.) with subtracted right neighbor. e.) and f.) show the profile of only the left ion’s light weighted with a Gaussian mask. Note that since the offset y_0 is not taken into account a full weighted profile of the neighbor is subtracted (noise and signal) resulting in a dip which fully cancels the impact of the neighboring ion’s fluorescence light.

To estimate the classification result of the whole sequence we can compare our expectations with the outcome of the algorithm. In a well prepared system (laser powers, laser-pulses etc.) one would expect a 25% probability to find the two ion crystal in each state (00, 10, 01 and 11), therefore one could expect the outcome of the sequence to roughly match these values. Table 3.3 shows the results of states found with the algorithm. As one can tell from the numbers in table 3.3, the 'dark, dark' (00) state occurred more than twice as often as expected, which in fact is not a discrimination

3.3 Two Ion Discrimination at 3 ms Timescale with 99.999% Algorithm-Fidelity

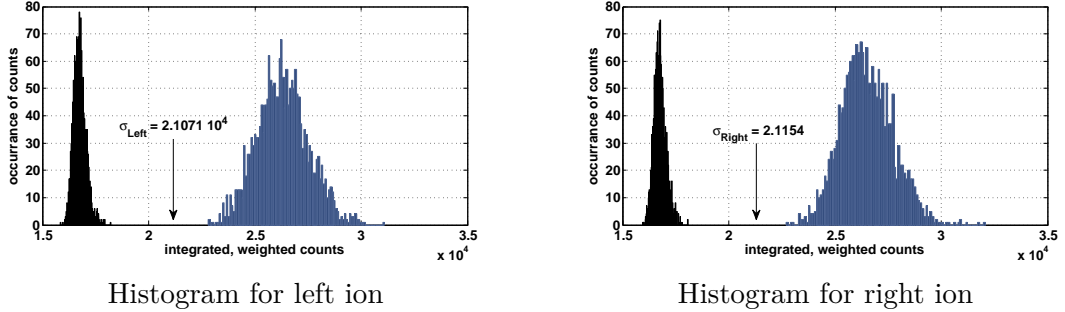


Figure 3.24: Histograms of the left and the right ion at 3 ms exposure time based on modulated images as described above. A set of 2.000 'bright' and 2.000 'dark' images was used. Note that since the histograms are clearly separated a decreasing of exposure time is feasible.

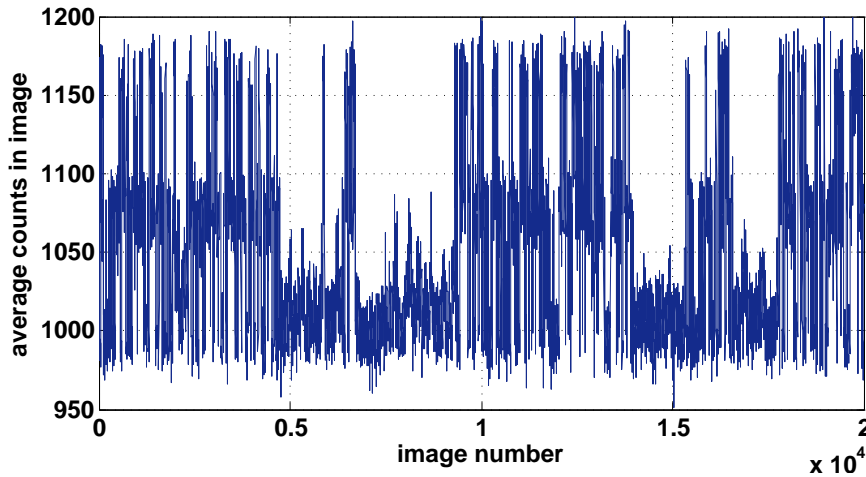


Figure 3.25: Averaged count rate of each image of the taken 'blink' sequence. Note that the three states overlap since this is a simple averaging.

state	found [%]
00	54.52
01	12.99
10	16.11
11	16.39

Table 3.3: Fraction of each state in the whole 'blinking' sequence . Note that 00 state derives more than a factor of two from the expected value.



3. DETECTION- AND READOUT SYSTEMS

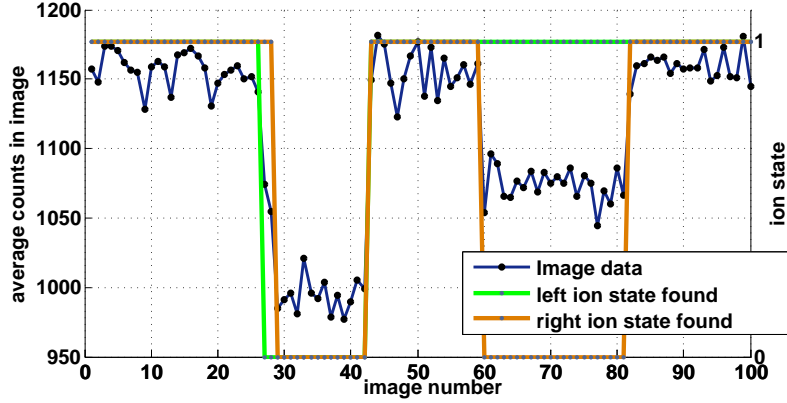


Figure 3.26: Result of the Gaussian-Mask algorithm applied to a random sequence of blinking ions. The right y-axis indicates the state of the ions as determined from the algorithm, where 0 represents dark and 1 represents bright state. The image data points are averaged count rates of an entire image comparable to a signal of the PMT. Note that measuring with a PMT one would realize in signals [60,81] that only one of the ions is bright but would not be able to distinguish which.

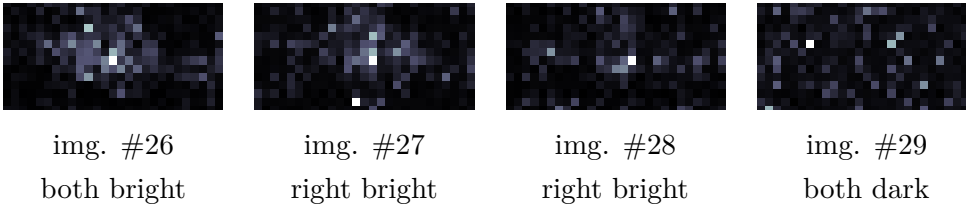


Figure 3.27: Set of images to verify the result of the algorithm applied to a random sequence at an exposure time of 3 ms.

error. As one can tell from the figure 3.25 the 'dark, dark' state actually occurred more often than the other states. The deviation can be explained by two means: i) the ion crystal might got hot and therefore appeared dark and ii) the powers of all lasers were not adjusted to realize a 25% branching of possible states. The relative fraction of other states roughly match the expectations.

A lot of effort was put into reduction of scattered light and better signal resulting in a better signal-to-noise ratio (beam alignment, laser powers, RF-amplitude and trapping potential) allowing us to reach a high fidelity discrimination accuracy of states of a two ion crystal at 3 ms exposure time. Since the histograms are clearly separated we should be able to further reduce the exposure time to values 1..2 ms allowing us to compete with the PMT and having the advantage of spatial resolution of the CCD camera.

4

Transport of Ions in a Segmented Paul Trap

4.1 Multi-Channel Arbitrary Waveform Generator

Over the last years, systems of trapped ions interacting with laser radiation have turned out to be promising candidates to realize a scalable quantum computer. Still, quantum systems composing a single trapping potential have several problems that prevent simply putting more ions into the trapping well from yielding scalability:

- the required strength of radial confinement to maintain the ions in a linear string increases with the number of ions
- rapidly growing number of vibrational degrees of freedom needs to be controlled and cooled to the ground state
- larger number of ions results in smaller distances hindering individual addressing of the ions.

The current state of the art is the demonstration of an entanglement of 14 qubits in a linear Paul trap (MSB⁺11), and it will be very difficult to obtain significantly more qubits using single trapping potentials. To circumvent these limitations, several proposals have been made and partially realized (see 1). Here the focus is put on the last method using multiplexed trap structures. The basic idea is to shuttle ions between different regions of a trap in order to control only a small group of qubits at a time. To operate a multi-segmented Paul-trap in this way, numerous, fast, stable



4. TRANSPORT OF IONS IN A SEGMENTED PAUL TRAP

and programmable DC-voltages are indispensable for the experiment since the ions need to be shuttled between a processor- and a storage region with high precision, requiring each of the 64 electrodes of our trap to be individually supplied. However, the task of combining all of these requirements is ambitious and the narrow field of application makes it difficult to *purchase* a commercial off-the-shelf solution, such that the need of a custom homemade solution arises. During the past years a series

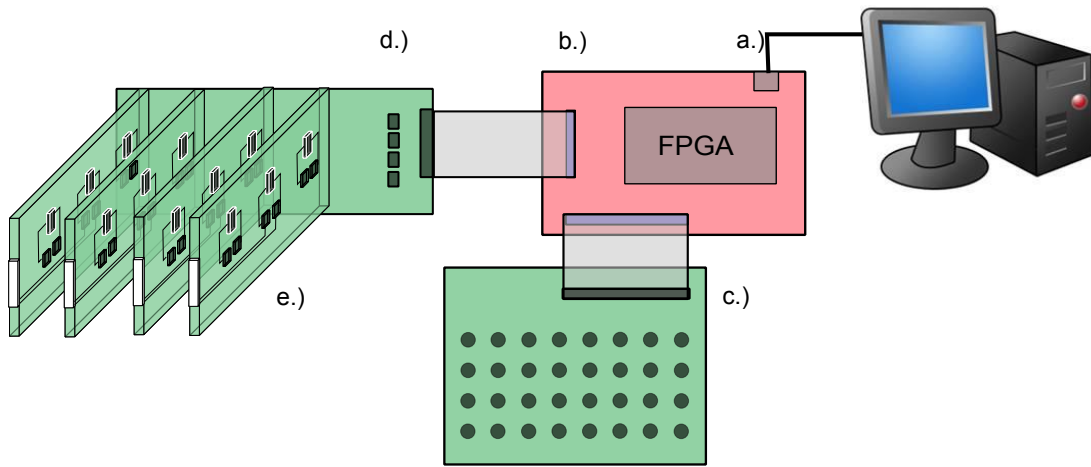


Figure 4.1: Scheme of the multi-channel arbitrary waveform generator. (a) gigabit Ethernet interface between a desktop computer and the FPGA. (b) Xilinx Virtex-5 FXT Evaluation Kit FPGA board (AVN11) (c) 32 channel of TTL outputs (d) mother-board of the analog part (e) analog cards with 24 programmable low-noise output stages. See text for further explanation.

of prototypes was designed, fabricated and tested (see (Sch09) for previous model) with the objective to fulfill the requirements for transport far below the adiabatic timescale. In the following, a short description of the latest prototype (see figure 4.1) is presented, which so far has shown promising results. The device is realized with a 'field programmable gate array' (FPGA) configured to operate as a fast 'first in, first out' (FIFO) register. It pushes the data from an integrated DDR memory, which is programmed with a regular desktop PC using a gigabit Ethernet interface, to the output pins of the FPGA board. The output pins are subdivided into two classes for two different purposes - programming an 'analog card' and Transistor-Transistor-Logic (TTL) for communication and synchronization with other devices. An amplifying board maps the output of a TTL-pin of the FPGA to the TTL standard (4.1(c)). The FPGA-

4.1 Multi-Channel Arbitrary Waveform Generator

pins designated for programming the analog cards are connected to a battery-driven¹ backplane-board² where optocouplers galvanically separate the FPGA and the analog part of the device (4.1(d)). The key parts of the device are four analog output boards each carrying three 8814 current³ digital to analog converter (DAC) chips⁴ with each chip providing four channels (4.1(e)). Each channel is connected to two amplification stages where the current is mapped on a $\pm 10\text{V}$, which results in a 0.3mV voltage resolution since each channel has a 16 bit resolution. We use two output stages in combination with an adder stage to easily apply differential voltages on one segment pair of a trap and at the same time reduce the differential noise. That way a single output channel provides us with two voltages $V_1 = V_0 + V_C$ and $V_2 = V_0 - V_C$ where V_0 is the voltage provided by the DAC and V_C is a compensation voltage, which can be supplied from either of the following sources:

- the ground in case no adder is needed
- an external source
- an internal op-amp that is adjusted using a potentiometer
- an internal DAC output⁵

A single channel of each DAC can be programmed simultaneously at a maximal update rate of 2.5MHz , two channels at 1.25MHz and so on until all four channels of each DAC are programmed at a rate of 625kHz . A delay of $N \cdot 20\text{ns}$ can be inserted in between each voltage programming where N is an integer value. Using four cards we are able to drive 12 voltages at 2.5MHz simultaneously or up to 48 voltages programmed at a rate of 625kHz . For a more detailed description of the device box see appendix B. Figure 4.2 shows a demonstration of simultaneous outputs of the device employing a single card. The spiky noise during the programming of a voltage arise from the oscilloscope, since digital probes are connected. Disconnecting the digital probes confirms that almost no digital clock signal is modulated onto the analog voltage as one can tell from figure 4.3. A transport measurement, described in section 5.2, supports the claim that almost no digital noise can be found on the analog outputs.

¹The analog part of the box is supplied with two 12V batteries to reduce noise.

²In the current version up to four cards can be installed.

³We use a current DAC since the noise emerged to be lower than that of a voltage DAC.

⁴See (Tex06) for more informations.

⁵Two DAC outputs (10 and 11) are designated to to operate as an adder or as a regular DAC



4. TRANSPORT OF IONS IN A SEGMENTED PAUL TRAP

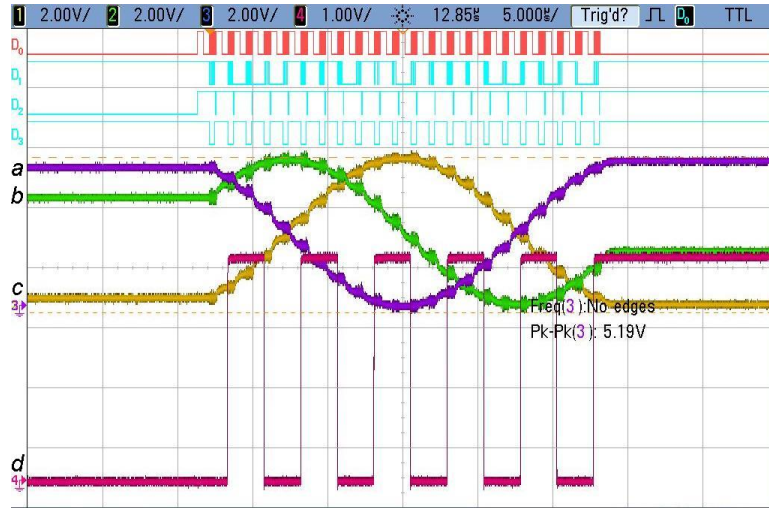


Figure 4.2: Example of simultaneous outputs of the arbitrary waveform generator measured with an oscilloscope. After each programming step a delay of 800 ns is inserted. Traces a), b) and c) show a sinusoidal signal shape with a 5 Volt amplitude using three DAC chips simultaneously. Signal d) shows a switched TTL output. Signals $D_{0,1,2,3}$ are digital pulses for DAC programming. Note that the noisy regions on the analog outputs arises from the oscilloscope since the digital probes are connected. The digital TTL signal is not affected since its ground is different from the analog part.

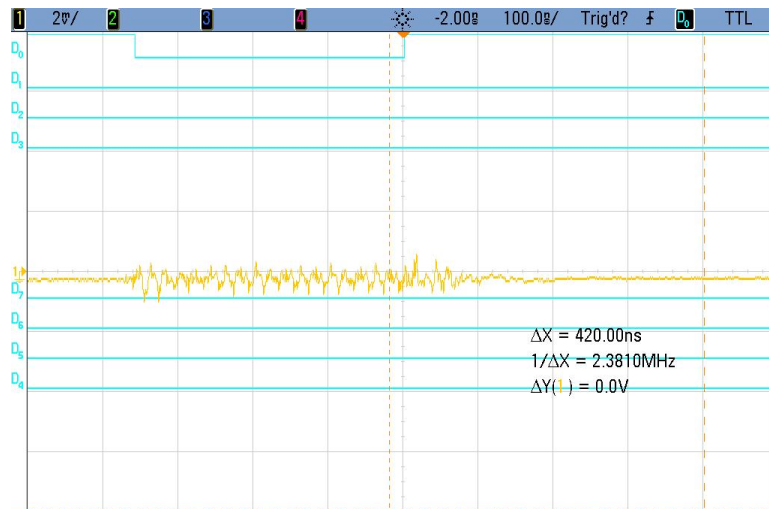


Figure 4.3: Noise measurement with only one digital line connected for triggering purpose. The oscilloscope sees the single digital line modulated with the rest of the digital signals (RF pickup). Note that to measure the analog output a 1:20 probe was used, therefore the y-axis scales up with additional factor of 20 resulting in a total scale of 40 mV.

4.2 Transport and Splitting of a Two Ion Crystal

The ion's position along the axial direction is defined by the axial trapping potential, which depends on the applied DC-voltages of each segment. The most simple trapping potential one can realize is a well, defined by three electrodes (see figure 4.4). Usually,

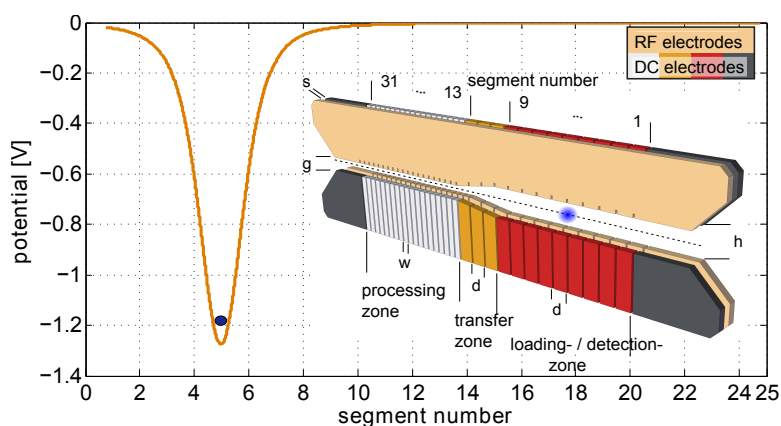


Figure 4.4: Calculated trapping potential with all segments grounded except for segment five. Here a potential using $V_5 = -6\text{ V}$ was calculated.

the trapping is performed at segment five since the flux of ^{40}Ca atoms is aligned at that segment. To transport the ion to another segment (e.g. segment six) the voltages need to be changed to create a trapping potential at that electrode. If the transport distance is short enough and the potentials overlap one could think of simply applying a trapping voltage to the neighboring segment and the ion would follow (see figure 4.5). However, using this technique would lead to a massive energy transfer and to avoid that, the minimum of the potential needs to be moved in a smooth way, e.g. using intermediate steps. An algorithm was developed¹ which takes the geometry of the trap and the initial potential into account to calculate the desired intermediate potential, using the following constraints:

- small voltage variations between each step since the experimental voltage supply is bandwidth limited
- voltage boundaries (in our case we are limited to $\pm 10\text{ V}$)
- constant potential shape to keep the axial frequency constant.

¹Killian Singer, Frank Ziesel (SPM⁺10)

4. TRANSPORT OF IONS IN A SEGMENTED PAUL TRAP

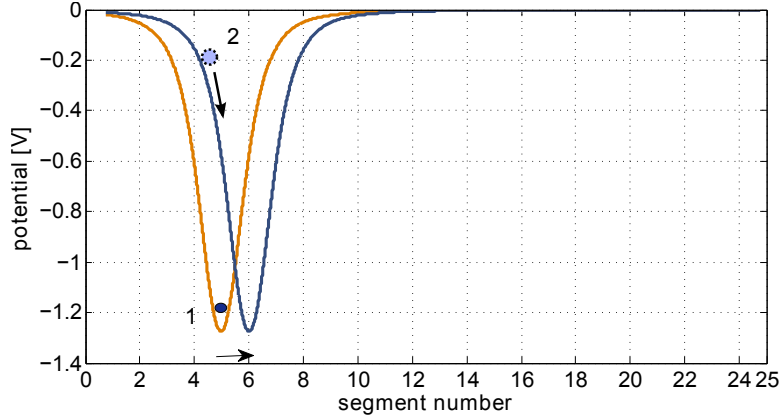


Figure 4.5: Transport by shifting the trapping potential to a neighboring segment (here from segment five to six). Note that the ion gains energy from point 1 to 2 if the potential is switched.

The forward problem of obtaining a set Φ_i of potentials, using a given number of electrodes, is given by:

$$\Phi_i = \sum_{j=1}^N A_{i,j} U_j, \quad i = 1..M \quad (4.1)$$

with N denoting the number of individually controllable electrodes and M the potential sample number. The matrix A maps the voltages U , taking the geometry of the trap into account, to a potential Φ . The ill-conditioned, inverse problem of equation 4.1, is here solved using Tikhonov regularization to obtain A^{-1} and calculate the required voltage set (SPM⁺10). Figure 4.6 shows the result of the algorithm where $M = 113$ intermediate potential positions were calculated, whereas figure 4.7 shows the required voltage set. Using these potentials we are able to deterministically adjust the ion's position along the trap axis limited by the precision of the calculated intermediate potentials and the resolution of voltage supply. An application of this positioning method is shown in a beam profile scan (see 5.1).

Another simple way of realizing a continuous transport is using a ramp (see figure 4.8(a)). Since the potentials and therefore the forces the ion is exposed to are known, one can numerically solve the classical equation of motion for the given problem

$$\ddot{\mathbf{x}}(t) = \mathbf{f}(t, \mathbf{x}) \quad (4.2)$$

where $\mathbf{f}(t, \mathbf{x}) = -q/m \frac{d}{dx} \Phi(t, \mathbf{x})$ is the force arising from the potentials, allowing one to calculate the ion's trajectory for a given potential set of time-dependent voltages

4.2 Transport and Splitting of a Two Ion Crystal

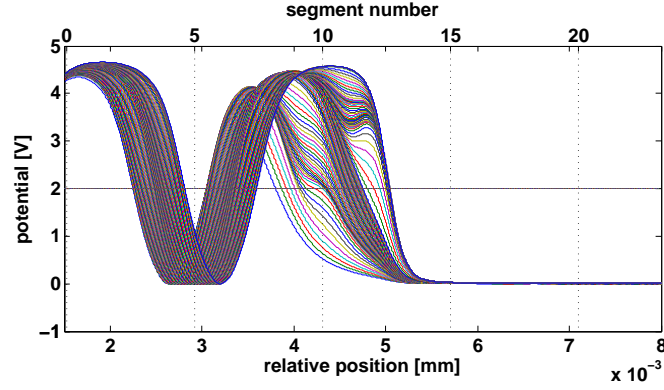


Figure 4.6: Total set of 113 intermediate potentials from segment four to six calculated with the algorithm.

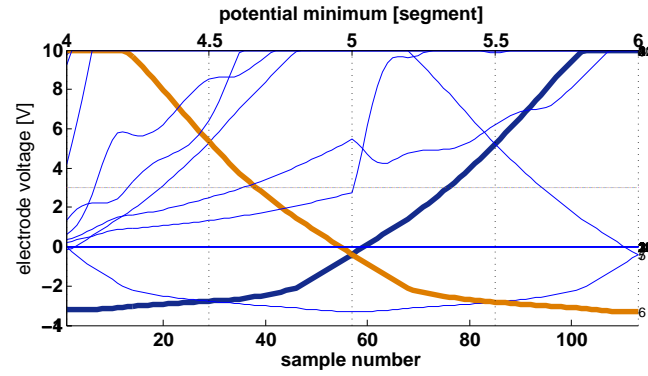


Figure 4.7: Voltages required to realize the potentials shown in figure 4.6. Note that highlighted voltage curves of segment four (dark blue) and segment six (orange) behave as expected.

(see figure 4.8). The amplitude of the resulting oscillation however is large enough to be resolved on the scale of the transported distance ($\approx 280 \mu\text{m}$), as one can tell from figure 4.8(b), which implies strong heating evoking the necessity of a smoother transport ramp. To realize a smooth transport the minimum of the potential, x_0 , needs to be moved in a smarter way, using a similar technique as a crane transporting its load between two points. Rainer Raichle et. al. calculated that an error-function-shaped movement of the minimum x_0 appears to be the best way to adiabatically transport a particle (RLB⁺06). Here a modified error function was used:

$$x_0(t) = \left(1 + \text{Erf} \left[-3 + \frac{6t}{T}\right]\right) / 2 \quad (4.3)$$

4. TRANSPORT OF IONS IN A SEGMENTED PAUL TRAP

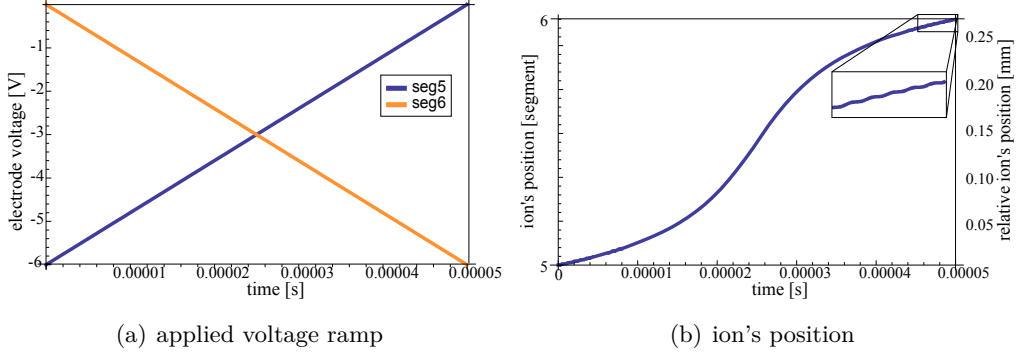


Figure 4.8: Part (a) shows the time evolution of the segment five and six, whereas (b) shows the position of the potential minimum and therefore ion's position.

where $\mathbf{x}_0(t)$ is the minimum position of the potential, $\text{Erf}(z) = \frac{2}{\sqrt{\pi}} \int_0^z e^{-t^2} dt$ and T the total transport time. Figure 4.9 shows the behavior of the position, velocity and force applied to the ion.

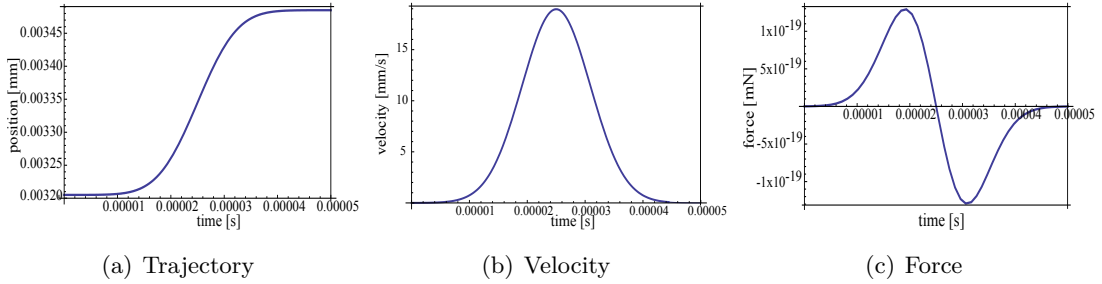


Figure 4.9: Theoretical erf-shaped transport of the ion. Note that the transport is smooth in position, velocity and force.

Now the desired $x_0(t)$ is known and the required voltage ramps need to be found. First the voltages of the electrodes need to be parameterized

$$\begin{aligned} V_1(t) &= V_0 \cdot (1 - y_0(t)) \\ V_2(t) &= V_0 \cdot y_0(t) \end{aligned} \quad (4.4)$$

with V_1 representing the time-dependent voltage of the starting electrode, V_2 the voltage of the ending electrode and V_0 being the initial trapping voltage. The function y_0 describes the time behavior of the voltages and therefore the potential's minimum position $x_0(t)$. Solving the equation of motion for any given voltage ramp, e.g. a linear ramp as described in figure 4.8(a), while knowing that the potential's minimum $x_0(t)$

4.2 Transport and Splitting of a Two Ion Crystal

matches the ion's position $x(t)$ for long transport times $T \rightarrow \infty$ (adiabatic regime), allows one to calculate the inverse map $x_0 \rightarrow y_0$ for any given function x_0 (e.g. equation 4.3) and obtain the required voltage ramps V_1 and V_2 (see figure 4.10(b)).

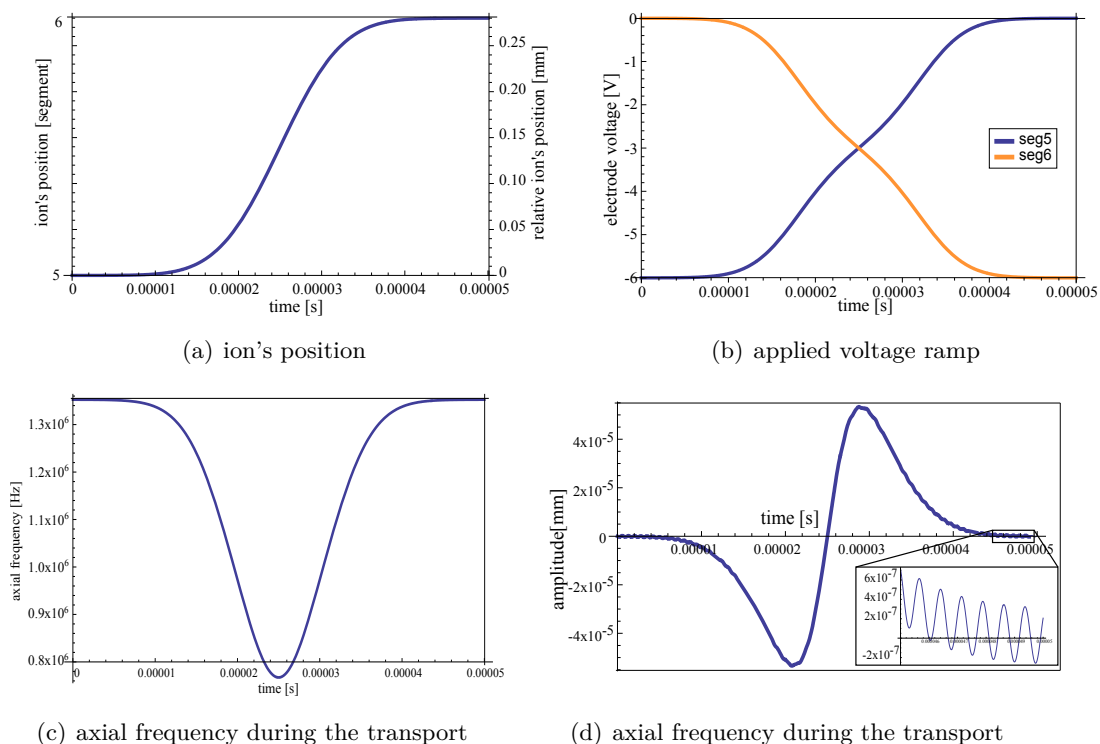


Figure 4.10: Part (a) shows the ion moving from segment five to six using voltage ramps pertaining to an Error function behavior of the potential minimum, whereas (b) shows the required voltages to realize 4.10(a). (c) shows the behavior of the axial frequency during the transport. (d) shows the oscillation amplitude. Note that the inertia reveals the shape of the applied force.

Figure 4.10(d) shows that using a smooth trajectory and force, the amplitude of oscillations can be reduced by a factor of 10^6 . Here, in order to resolve the oscillations in this plot, the solution to the equation of motion, $x(t)$ 4.2, was subtracted from the theoretical trajectory of the potential minimum, $x_0(t)$, given by equation 4.3. Note that due to the inertia of the ion, an xe^{-x^2} shape that corresponds to the applied force is revealed (the ion follows the force and therefore differs from the theoretical trajectory). Figure 4.10(d) also shows small oscillations from the beginning which arise from the fact that using numerical calculation, the initial position of the ion could not be calculated

4. TRANSPORT OF IONS IN A SEGMENTED PAUL TRAP

exact enough to place it in the center of the potential. Further, the constraint of constant axial frequencies was omitted as one can tell from figure 4.10(c). Note that the energy transfer from the transport is obtained from purely classical calculations, such that possible quantum mechanical contributions, like squeezing, are neglected.

Splitting

The splitting of an ion crystal in a micro-structured Paul trap, having the constraint of staying close to motional groundstate, is more complex than mere transport since the potentials need to be modified in a way that the crystal deterministically splits. Deviations of the electrode voltages in a range of $\Delta V \approx 10$ mV is sufficient for the splitting to fail. Further, during the splitting the potential is modified in a way that a critical point with *non*-harmonic axial enclosure (see 4.11(b)) is traversed, leading to inadvertent quantum mechanical effects. Figure 4.11 shows a splitting method for

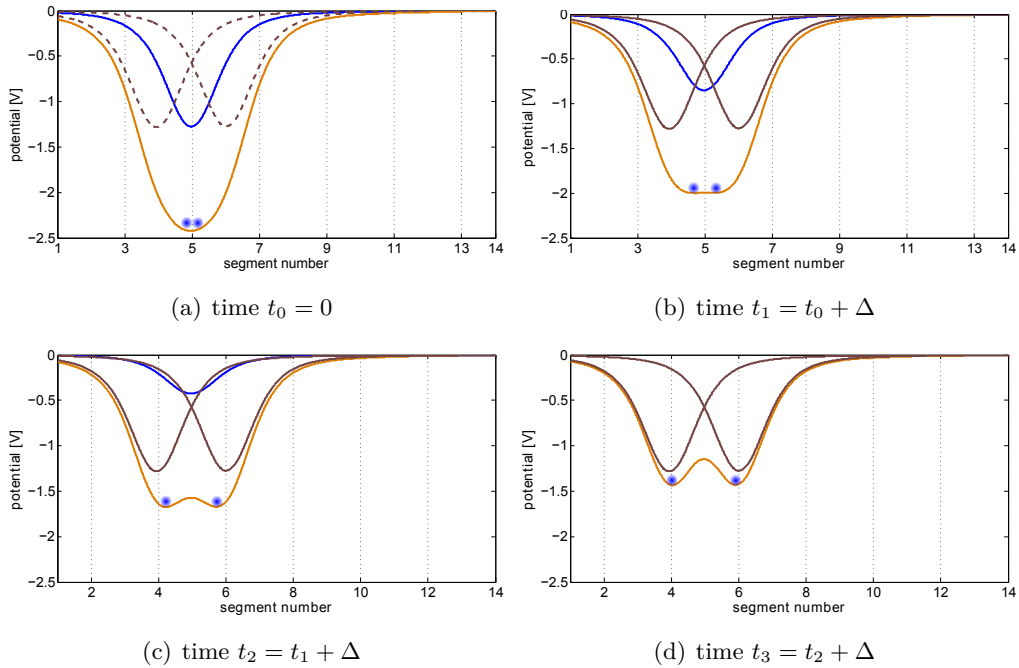


Figure 4.11: Parts (a)-(d) show time development of the trapping potential for splitting starting at part (a).

demonstration purpose. The result is visualized by using this thesis as a flip-book.

5

Experiments

5.1 Ion as a Beam Profilometer

Often, the experiment requires a tight focus of a laser in order to reduce scattered light or efficiently use the power provided by the laser. In some cases the beam needs to be focused to its diffraction limit i.e. individual addressing of qubits (NRR⁺00). Therefore the precise shape of the laser profile at the ion's position is of interest. The combination of multi-channel arbitrary waveform generator and the CCD camera qubit readout enables us to employ the ion as a probe for the transverse mode profile of a laser beam. For the dipole transition near 397 nm we can determine the shape measuring the amount of light detected by the camera depending on the position of the ion and reconstruct the shape since the amount of scattered photons is proportional to the intensity of the laser beam. The profile of the quadrupole transition near 729 nm however is more important since for some experiments it is crucial to focus the beam to its diffraction limit to be able to address the ions individually (NRR⁺00). However, the profile of the near 729 nm laser cannot be accessed directly as explained for the 397 nm laser. To measure the profile we utilize the effect of Rabi oscillations on the $S_{1/2} \leftrightarrow D_{5/2}$ quadrupole transition, where the Rabi frequency Ω is proportional to the square root of intensity I of the laser. First, the Rabi frequency is maximized by aligning the 729 nm laser, and using the maximum Rabi frequency and a fixed $\pi/2$ pulse time¹ (figure 5.1 blue line) the resulting signal becomes sensitive for any change to the laser intensity.

¹Here, a $\pi/2$ pulse time is set to make sure not to 'overflow' the signal since the coarse maximization of the Rabi frequency using the beam might not be the maximum.



5. EXPERIMENTS

Moving the ion through the 729 nm laser beam allows us to precisely measure its profile

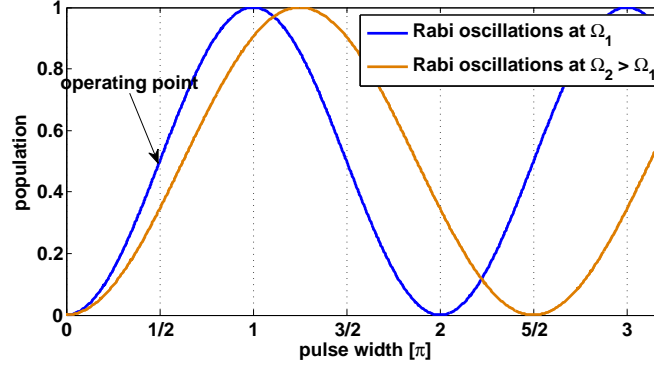


Figure 5.1: Sketch of Rabi oscillations depending on the intensity of near 729 nm laser light. Blue line denotes Rabi oscillation at maximal frequency (maximal intensity) whereas the orange line shows slower oscillations (less intensity). Note that using $\pi/2$ time of the blue line the signal of the orange line drops.

limited by the amount of projection measurements and the precision of ion positioning. To demonstrate this technique figure 5.2 shows the result of a profile measurement of a Laguerre-Gauss mode \mathbf{LG}_{10} (PE04). The ion has been moved over a total distance of $d = 80 \mu\text{m}$ using steps of $\Delta x = 2 \mu\text{m}$. The ion reveals the transverse intensity profile

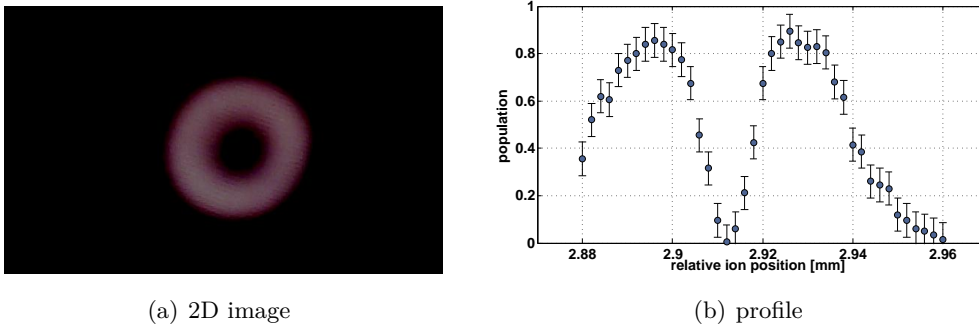


Figure 5.2: Trace a) shows a 2D image of the \mathbf{LG}_{10} mode, whereas b.) shows the profile scan using the ion. The error $\Delta y = 0.07$ is determined by the amount of projection measurements (here 200). The error Δx can be neglected.

of the Laguerre-Gauss mode with high accuracy, limited by projective measurements and the ion positioning. In future, one could use this profile measurement technique to focus the beam to its diffraction limit and verify its shape to avoid unwanted effects

coming from optics. Particularly, one expects interesting effects which arise from a strong gradient of the Laguerre-Gauss mode which will be investigated in future.

5.2 Fast Axial Transport of a Single Ion

One possibility to realize the scalability of an ion-trap-based quantum computer is to shuttle and manipulate only a small number of ions. To do so, the ions need to be transported in a way transferring as little energy as possible to the ion. As explained in section 4.2 an ion transport can be realized by ramping the voltages between two electrodes. Here we used a simple sinusoidal voltage ramp to achieve a transport between segments five and four.

$$V_5(t) = V_0 \cdot [1 - A \cdot x_0(t)]$$

$$V_4(t) = V_0 \cdot A \cdot x_0(t)$$

with $x_0(t) = \sin^2(\frac{\pi t}{T})$ used as a ramp to move the potential minimum, $V_0 = -6$ V the initial trapping depth and A as a parameter to control the distance of the transport. The total (back and forth) transport time T was set to $200 \mu\text{s}$ and the first qualitative measurement of a transport was done using a pulse-width scan on the quadrupole transition near 729 nm. The basic idea is that the Rabi frequency Ω depends on the phonon number of the ion and therefore the contrast of the Rabi oscillations depends on the temperature. Rabi frequency depending on the transition and the amount of phonons is given by:

$$\Omega_{n,n+s} = \Omega_{n+s,n} = \Omega_0 \left| \langle n+s | e^{in(a+a^\dagger)} | n \rangle \right| \quad (5.1)$$

where n is the phonon number, s the sideband order (in our case we used the carrier transition, $s = 0$) and Ω_0 the bare Rabi frequency. Higher phonon numbers n result in lower Rabi frequencies and since the phonon numbers follow the Bose-Einstein distribution, the total measured Rabi oscillation is a superposition of Rabi oscillations at different Rabi frequencies. Figure 5.3 shows the results of measured Rabi oscillations at different parameters A . The total transport distance d can be roughly approximated by $d \approx A \cdot 280 \mu\text{m}$. The first results show strong energy transfer even at short transport distances. Even a tiny transport to a distance $d = 0.28 \mu\text{m}$ indicates massive excitation of vibrations. Transporting to further distances excites the ion to a state where no



5. EXPERIMENTS

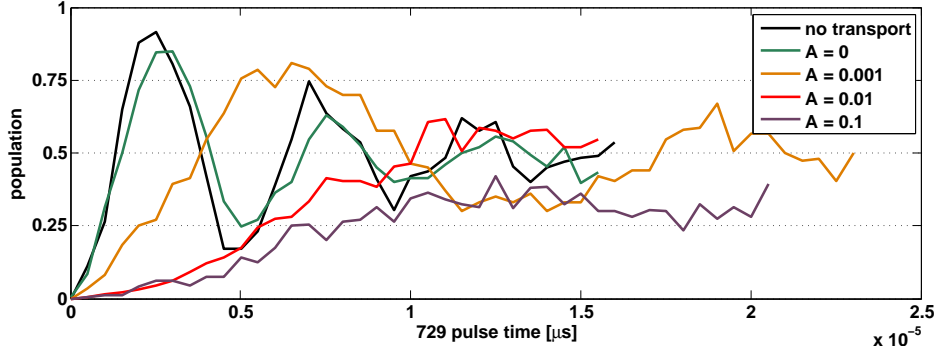


Figure 5.3: Transporting the ion at $200 \mu\text{s}$ back and forth with distance adjusted by the factor of A . Note that the case $A = 0$ indicates that almost no digital noise is modulated onto the analog output of the arbitrary waveform generator.

Rabi oscillations can be observed at all. Several improvements have been proposed to realize a better transport:

- lowpass filtering of the voltages provided by the device
- different voltage ramps
- constant potential depth during the transport
- avoid voltages requiring a change if the most significant bits in the DAC register.

which need to be verified. Still, one pleasant result can be extracted from this measurement: the trace using parameter $A = 0$ indicates that almost no digital clock noise is modulated onto the analog outputs of the arbitrary waveform generator.

5.3 Relative Ion Position Measurement

Another useful combination of spatial information of the CCD camera and the ability to precisely, independently adjust several electrodes, is the possibility to measure the ion position in all spatial dimensions relative to the electrodes. Figure 5.4 shows the initial trapping setup where the ion's position is ideally supposed to be in the center of the potential created by the geometry of the electrodes and applied voltages. Independently varying the voltage of electrode one, two, three and four, which were initially set to ground, leads to a displacement of the ion along the x direction which can be observed

5.4 Reduction of Micromotion - Compensation Scan

with the camera. The absolute displacement depending on the applied voltage on electrode one, two and three and four respectively should ideally match if the ion is situated in the geometric center of the trap. Hence the deviation from this behavior can be used to calculate the relative position of the ion. Measuring the relative axial

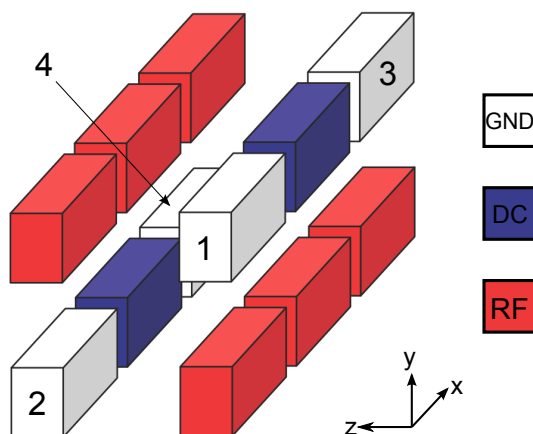


Figure 5.4: Scheme of the electrodes used for the ion position measurement.
Original image: (Pos11)

position as a function of applied voltage on electrode one, two, three and four allows one to measure the impact of each electrode on the ion and therefore its relative position if the geometry is known.

To determine the position of the ion on the CCD image a Levenberg-Marquardt fitting routine was implemented (see Appendix A.3) and using image processing techniques one can fit a Gaussian profile on the image resulting in a sub-pixel localization accuracy. The resulting displacement from the geometric center of the trapping configuration was found to be $|\Delta x| \approx 6 \mu\text{m}$, $|\Delta y| \approx 9 \mu\text{m}$ and $|\Delta z| \approx 2 \mu\text{m}$ which most likely arise from imperfections of the trap geometry and minor differences of the supplied voltage of each pair.

5.4 Reduction of Micromotion - Compensation Scan

The fabrication process of the trap (e.g. geometry of electrodes) usually leads to deviations from the ideal trapping potential resulting in a displacement of the ion with respect to the radio frequency (RF) node. Even in a trap having perfect geometry



5. EXPERIMENTS

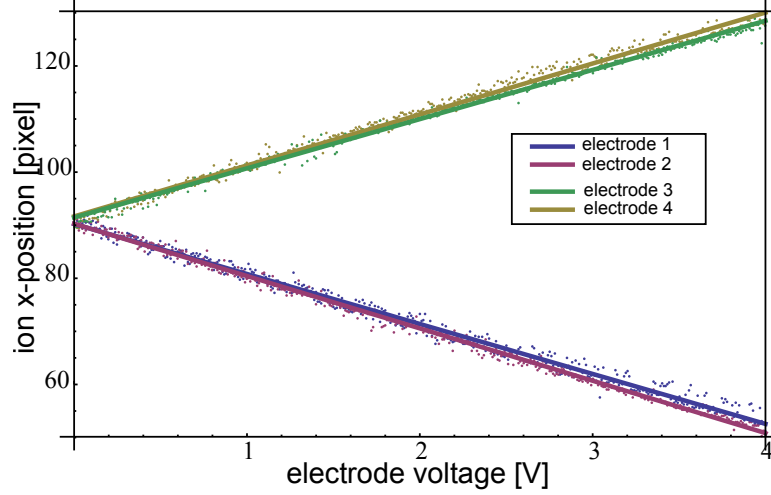


Figure 5.5: Results of displacement measurement. Note the linear behavior and slight difference in slope if of two different segment pairs.

stray charges and background fields would result in a shift. This displacement leads to micromotion as the ion oscillates around the mean value of the RF node driven by the RF frequency. Still, we can compensate the ion position along the dc-axis by applying a compensation voltage V_C using the multi-channel voltage with programmable compensation source resulting in two voltages: $V_{1,2} = V_0 \pm V_C$. The displacement of the ion along the RF-axis can be slightly adjusted by shifting the trapping potential with an offset $V_{1,2} = V_0 \pm V_C + V_O$ (see figure 5.6). To minimize the micro motion we use the effe-

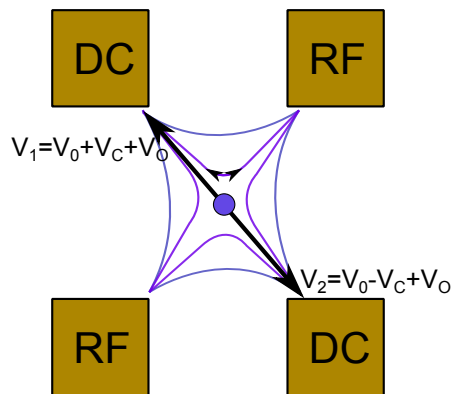


Figure 5.6: Scheme of compensation directions depending on the compensation voltage V_C or offset voltage V_O used for the scan. Note that the offset voltage V_O has only limited impact on the ion position.

5.4 Reduction of Micromotion - Compensation Scan

of Doppler-broadening caused by the ions movement driven with the RF frequency. Tuning the Doppler cooling- and readout laser to the red side of the atomic resonance at approximately half maximum of a potentially Doppler-broadened line, results in a high sensitivity of the fluorescence light to the linewidth. More Doppler broadening results in more fluorescence and less fluorescence indicates less Doppler broadening and therefore less micro motion as one can tell from figure 5.7. The amount of scattered

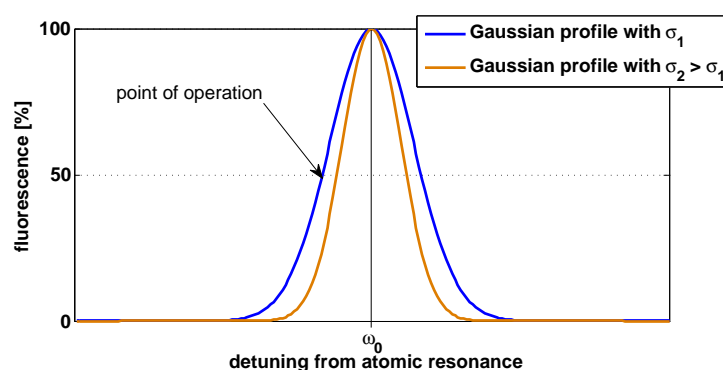
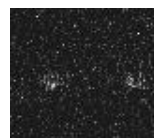


Figure 5.7: Scheme of the Doppler broadening used to minimize the micro motion along one direction. The blue curve denotes a Doppler broadened resonance fluorescence caused by micro motion whereas the orange trace indicates a smaller linewidth since the micro motion is reduced. Note that a smaller line results in less fluorescence therefore the amount of light scattered by the ion can be used to minimize the micro motion.

light is measured using the CCD camera while scanning the parameter space of V_C and V_O in steps of $\Delta V_C = 0.01$ V and $\Delta V_O = 0.05$ V. The result of the scan is presented in figure 5.8. The scan displays an understood valley where the compensation can be adjusted in a way that the fluorescence for a red detuned Doppler cooling laser is minimized. This valley arises from deviations from a perfectly symmetric Paul trap requiring different compensations for different offset voltages. The fringes and the gap where the ion is unstable or not cooled is yet not fully understood. Simulations have shown that this effect might appear from a degenerate setting where the two radial frequencies match and therefore no Doppler cooling is possible. The position of the fringes and the gap depend on the amplitude of the RF which implies that it might be some instability fringe of the stability diagram. This effect will be investigated further by Konstantin Ott and will be described in more detail in his Diploma thesis.



5. EXPERIMENTS

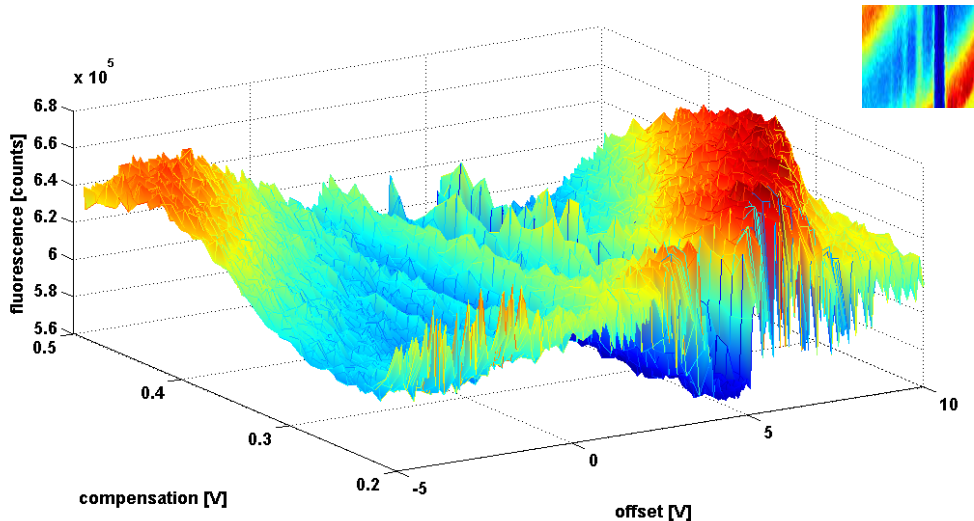


Figure 5.8: Red-detuned compensation and offset scan. The blue regions indicate voltage setting with low fluorescence and therefore small micro motion amplitudes. Note several equidistant fringes appear where the ion seems to be less compensated and a strong gap which at first sight appears as the best point to operate with. In fact this gap seems to be a forbidden zone since the trapping seems to become unstable or the cooling does not work.

5.5 Magnetic Gradient Measurement

The transport between storage- and processor regions with minimum loss of coherence, has so far proven to be a difficult task. One of the leading sources for decoherence using transport is the dephasing arising from magnetic field gradients. In this measurement we employed the ion as a magnetic field gradient probe along the axial trap direction by letting the ion accumulate a phase during a transport which arise from inhomogeneities of magnetic field. To measure the gradient we applied a spin-echo Ramsey scheme as one can tell from figure 5.9. The spin-echo scheme cancels out all dephasing effects that arise from different sources than the magnetic field gradient. The preparation stage consists of Doppler cooling pulses as well as optical pumping pulses, where σ^+ light on the cycling transition, initializes the ion to the $m_J = +1/2$ state. The coherent coupling between the two spin states, is performed by stimulated Raman transitions (Pos09). Since the Doppler cooling and readout laser is not narrow enough to distinguish between the two spin states (≈ 18 MHz separation) the 729 nm frequency stabilized diode laser

5.5 Magnetic Gradient Measurement

was used to shelf the $m_J = +1/2$ to the metastable $D_{5/2}$ state. We use a regular

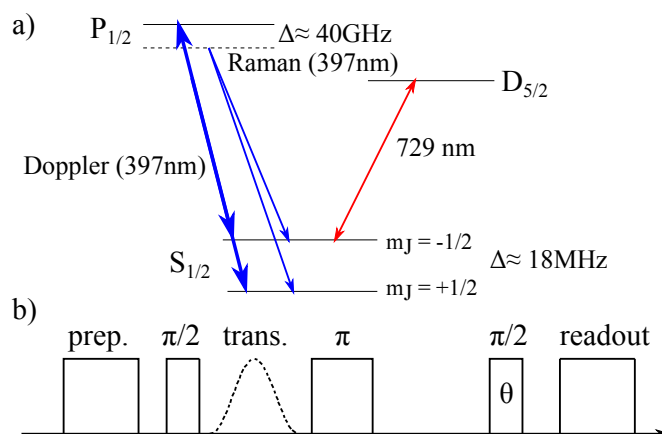


Figure 5.9: Pulse scheme and utilized transitions to measure the magnetic field gradient.

trapping potential at segment five with an additional arbitrary waveform generator¹ connected to segment four, applying an additional potential and shifting the minimum of the trapping potential, thus moving the ion throughout the trap. The transport cycle was set to $T = 400 \mu\text{s}$ therefore the assumption of adiabatic following of the ion is justified ($T \gg 1/1.35 \text{ MHz}$). The scheme can be easily explained using the Bloch sphere (see figure 5.10). The dependence of collected phase arising from magnetic field

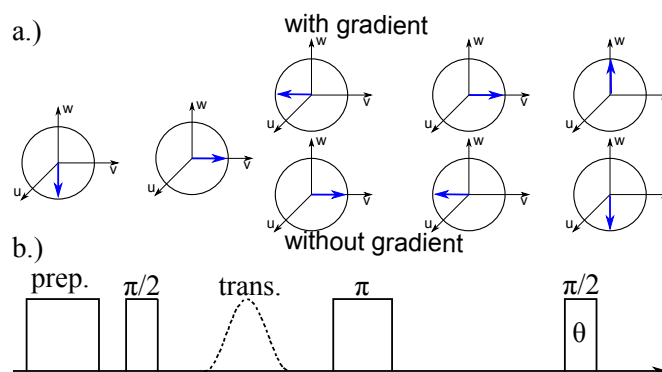
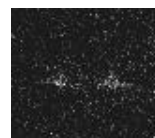


Figure 5.10: Pulse scheme realized in a Bloch sphere Scheme. Sub figure a.) denotes a population development in the using a Bloch vector notation, whereas scheme b.) shows the pulse sequence applied. Note that the spin-echo scheme cancels out all effects arising from sources except the gradient.

¹Agilent 33250a



5. EXPERIMENTS

gradient and the transported distance is described by

$$\phi_{rad} = \frac{g_J \mu_B}{\hbar} \frac{\delta B}{\delta x} \int_0^T [x_{ion}(t) - x_{ion}(0)] dt \quad (5.2)$$

The integral in equation 5.2 can be numerically calculated knowing the geometry of the trap and the voltages applied. The Landé factor of the $S_{1/2}$ state is given by $g_J = 2$. Measuring the accumulated phase along the magnetic field at different distances knowing the constants μ_B (Bohr's magneton) and \hbar (reduced Plank constant) allows one to precisely calculate the gradient $\frac{\delta B}{\delta x}$. The result of the measurement and the omitted details can be extracted from the appended paper.

Single ion as a shot-noise-limited magnetic-field-gradient probe

A. Walther,^{*} U. Poschinger, F. Ziesel, M. Hettrich, A. Wiens, J. Welzel, and F. Schmidt-Kaler

Institut für Quantenphysik, Universität Mainz, Staudingerweg 7, DE-55128 Mainz, Germany

(Received 11 March 2011; published 23 June 2011)

It is expected that ion-trap quantum computing can be made scalable through protocols that make use of transport of ion qubits between subregions within the ion trap. In this scenario, any magnetic field inhomogeneity the ion experiences during the transport may lead to dephasing and loss of fidelity. Here we demonstrate how to measure, and compensate for, magnetic field gradients inside a segmented ion trap, by transporting a single ion over variable distances. We attain a relative magnetic field sensitivity of $\Delta B/B_0 \sim 5 \times 10^{-7}$ over a test distance of 140 μm , which can be extended to the mm range, still with sub- μm resolution. A fast experimental sequence is presented, facilitating its use as a magnetic-field-gradient calibration routine, and it is demonstrated that the main limitation is the quantum shot noise.

DOI: [10.1103/PhysRevA.83.062329](https://doi.org/10.1103/PhysRevA.83.062329)

PACS number(s): 03.67.Lx, 37.10.Ty, 42.50.Dv

I. INTRODUCTION

Over the past decade, trapped ions have emerged as one of the most promising systems to realize quantum computation, with many key ingredients implemented experimentally, such as single and multiple qubit gates [1]. It appears difficult, however, to scale single zone traps significantly beyond the order of ten qubits [2]. One way to store and manipulate such complex systems on a larger scale with a larger number of ions is to divide the ion-trap quantum computer into several regions—each holding only a few ions—combined with transport of the ions between them [3]. To realize this, it is paramount to make the transport between storage regions and processor work with a minimum loss of coherence, which has proven to be a challenge so far. In this paper we investigate the transport of single ion qubits and address one of the leading dephasing mechanisms arising from magnetic field gradients. Previous transport demonstrations [4] have avoided magnetic-field-induced dephasing by adding an extra set of qubit levels, which are less sensitive to field changes during transport. This, however, adds extra complexity to the scheme, and also may not work for all ion species. It has also been shown that adding extra identical transport sequences after a π inversion can cancel out unwanted phase shifts [5] even when transporting across junctions; however, such extra phase-changing operations do not appear to be feasible when transporting qubits that are a part of larger entangled states. Another approach is to use two physical ions in an entangled state to form one logical qubit in a subspace which is free of decoherence from the magnetic field variations over the transported distance [6], at the expense of needing twice as many ions. Even in this scenario, however, the difference in magnetic field magnitude between the two paired ions needs to be sufficiently low.

Here we present a technique for measuring, and compensating for, the magnetic field gradient inside the trap, using a single ion as a movable probe. We carefully tune the currents of external Helmholtz coils for very low B -field gradients. Stationary two-ion crystals also allow for local measurements of gradients [7], although the transport method presented

here adds further advantages. The attainable accuracy of the measurement is higher, because the ion can utilize a much larger distance over which changes to the field are picked up. The gradient is measurable over a much larger spatial extent with a sub- μm resolution, and extends to regions outside those accessible by the laser beams and the ion observation, for example, into storage regions or even across corners and junctions.

For general scientific interest we envisage applications of our method where the combination of high spatial resolution and shot-noise-limited performance is used to map out the magnetic field even of single protons [8] or molecules [9]. We note that μm resolutions have also been reached using Bose-Einstein condensates [10].

II. EXPERIMENTAL SETUP AND METHOD

In our experiment, we employ a segmented microstructured Paul trap [11], where a combination of static and dynamical electric fields provide confinement for a single $^{40}\text{Ca}^+$ ion, and where the segmented design of the trap allows for transport [12]. The strengths of the trapping potentials lead to harmonic oscillation frequencies of $\omega/2\pi = \{1.35, 2.4, 3\}$ MHz in axial and both radial directions, respectively. The relevant internal states of the ion are shown in Fig. 1(a), where Doppler cooling is performed on the $S_{1/2} \rightarrow P_{1/2}$ (cyclotron) transition near 397 nm. The two ground-state spin levels, $|m_J = \pm 1/2\rangle$, are used as qubit states, and operated on by employing stimulated Raman transitions using a separate 397 nm laser, which is detuned by $\Delta \approx 2\pi \times 40$ GHz from the cyclotron transition. In addition, a laser at 729 nm provides state selective shelving during readout, while lasers at 866 and 854 nm prevent trapping in metastable states. Two coils outside of the vacuum chamber in a Helmholtz-like configuration are set up to give a B -field axis at a 45° angle with respect to the trap axis. During the experiment, a magnetic field offset is kept around ~ 0.7 mT giving a Zeeman splitting of the spin states of about 18 MHz, while gradients are tuned by the application of different currents to the two coils.

For determination of magnetic gradients we employ the following sequence of operations, depicted in Fig. 1(b): (i) preparation pulses consisting of Doppler cooling pulses as well as optical pumping pulses which initialize the ion to the

^{*}walthan@uni-mainz.de; <http://www.quantenbit.de>

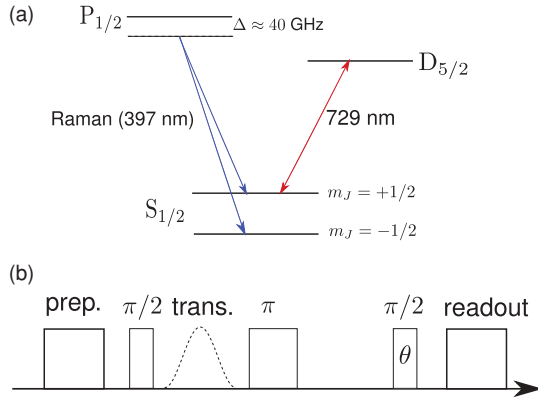


FIG. 1. (Color online) (a) Reduced level diagram of the $^{40}\text{Ca}^+$ ion with the levels that are relevant for the presented experiments. (b) Spin-echo pulse sequence used to measure the magnetic field gradient. The preparation and readout each consist of several steps, as described in the text, and the dashed pulse is the electric potential change that causes the transport, while the solid boxes are laser pulses.

$m_J = +1/2$ state, (ii) spin-echo sequence, with the transport pulse inserted between the first $\pi/2$ pulse and the π pulse, and (iii) readout pulses, which are carried out by an efficient state selective transfer on the 729 nm transition followed by fluorescence from the Doppler laser [13].

Precise knowledge of the transported distance as a function of time comes from a calculation of the potential minimum of the trap for each value of an applied voltage by means of a numerical field solver [14]. In Ref. [12] we experimentally confirmed that the potentials obtained from the simulations match the actual potentials in our trap with an accuracy on the 1% level. From the solver, one can obtain normalized shape factors, $\tilde{u}_i(x)$, that are fixed by the geometry of the trap and depend on the segment number, i , and the distance from that segment, x . The total potential can then be obtained by summation of the voltages applied to each segment multiplied by its respective shape factor:

$$V(t) = V_1 \tilde{u}_1(x) + V_2(t) \tilde{u}_2(x). \quad (1)$$

Here, V_1 is the fixed potential on the main trapping segment and $V_2(t)$ is a time-dependent sine-shaped voltage that is applied to a neighboring segment, such that the ion is moved a certain distance and then moved back, ending at its initial position. $V_2(t)$ is created by a waveform generator and all unused segments are kept at ground. The duration of the transport pulse is $T = 400 \mu\text{s}$, which is shorter than the coherence time of the qubit state but much longer than the inverse of the axial trap frequency, $(1.35 \text{ MHz})^{-1}$. The latter condition means that the ion may adiabatically follow the changes to the voltages, such that the position of the ion can be obtained from the minimum of the total potential at any given time as a function of the applied segment voltages, i.e., $x_{\text{ion}} = x_{\text{ion}}(V_1, V_2(t))$. The total phase shift acquired by the ion is given by the time integral of the frequency shift caused by the B -field gradient during the transport. The frequency shift is proportional to the B field, which in turn is proportional to the spatial position in a

first-order approximation. We can thus express the phase shift in terms of the ion position and the magnetic field gradient:

$$\phi_{\text{rad}} = \frac{g_J \mu_B}{\hbar} \frac{\delta B}{\delta x} \int_0^T [x_{\text{ion}}(t) - x_{\text{ion}}(0)] dt, \quad (2)$$

where the Landé factor of the $S_{1/2}$ state is given by $g_J = 2$. The integral in this equation is thus determined from the displacement of the ion, which is given by evaluating the minimum of the applied potential. It is then clear that the magnetic field gradient, $\delta B/\delta x$, can be extracted by measuring the acquired phase shift for a particular known displacement-time integral.

III. RESULTS

A. Measurement of magnetic field gradients

The result of our experiment to measure the magnetic field gradient over a maximum distance of $140 \mu\text{m}$ is plotted in Fig. 2 for different currents on the Helmholtz coils. Three distinct cases were measured: (i) a large gradient corresponding to 3 A in coil 1 and 1 A in coil 2, (ii) equal currents, 1.9 A, in each coil, and (iii) with currents chosen to minimize the gradient, yielding 1.660 A in coil 1 and 2.122 A in coil 2. The particular values in the optimized last case were chosen by extrapolation from the first two cases, with the desire to reach a zero gradient. In all three cases, the offset magnetic field is close to the same value, i.e., around 0.7 mT, but the gradient varies over more than two orders of magnitude.

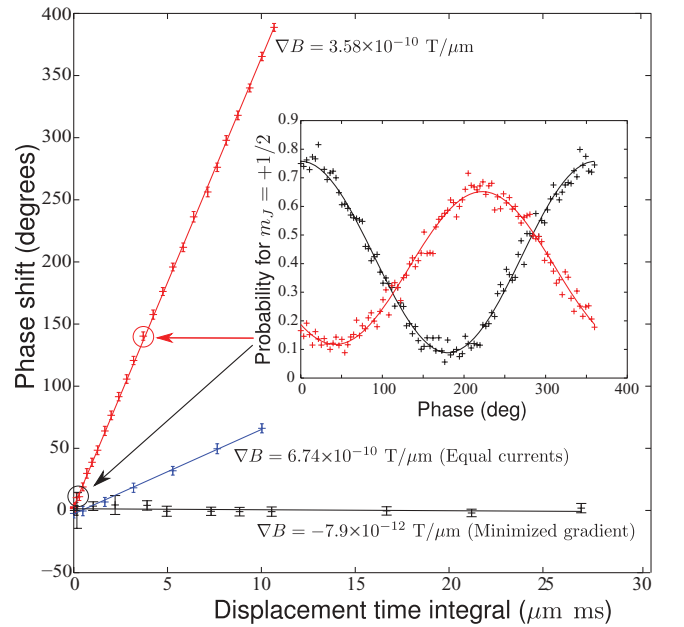


FIG. 2. (Color online) Recorded phase shift as a function of transported distance and time (see text), for three different coil currents. The slope gives the magnetic field gradient, which is listed next to each respective curve. Note how the optimized coil current setting has a gradient that is two orders of magnitude lower than when the coils have the same current. The inset shows the evaluation of a spin-echo fringe for one particular gradient and transport setting compared to a nonshifted one. Each point in the inset consists of 200 ion interrogations.

Furthermore, the standard deviation of the phase measurement in Fig. 2 is about 2° , and from the near-perfect linear fit, we can conclude that the linear approximation that was used in Eq. (2) was well justified. In the figure, each phase shift is evaluated from a cosine fit to the fringe pattern data, resulting from a spin-echo sequence where the phase of the final $\pi/2$ pulse is varied between 0 and 2π in 100 steps, as shown in the inset. The phase is then plotted versus the displacement-time integral [see Eq. (2)], i.e., the representation of how long the ion stays in a magnetic field that is different from its starting location, times the transported distance.

B. High-precision detection of small gradients

The main application for this type of magnetic field inhomogeneity measurement is the creation of a low-decoherence environment for quantum computing, and we now focus on measurements of the low gradient case with high precision. We also aim at using as short as possible total measurement time, such that the method can be efficiently used as a calibration routine. Shortening the time of the acquisition can be achieved by reducing the number of points that are used to determine the acquired phase shift. In principle, for small phase shifts, it is enough to measure the spin-up probability at a concluding angle of $\theta = \pi/2$ in the cosine curve, where the slope is the steepest, in order to obtain an estimation for the phase shift. In reality, however, various mechanisms can cause offsets and loss of contrast of the fringe, which leads to the $\pi/2$ point getting shifted for other reasons than acquired phase. To accommodate for this, we additionally measure the baseline and the contrast of the fringe pattern by also probing the points $\theta = 0$ and $\theta = \pi$, respectively. We can now form a normalized signal, S , which is independent of contrast and offset:

$$S(\phi) = \frac{p(\pi/2, \phi) - p(\pi, \phi)}{p(0, \phi) - p(\pi, \phi)}. \quad (3)$$

With a 5 ms detection time, one measurement of the signal $S(\phi)$, comprised of the three measurement points at $\phi = \{0, 0.5, 1\}\pi$, thus takes 15 ms. In Eq. (3), $p(\theta, \phi)$ denotes the probability of measuring the ion in spin up as a function of the angle of the concluding $\pi/2$ pulse, θ , and the phase shift induced by the magnetic field gradient, ϕ . In general, $p(\theta, \phi)$ is described by a sinusoidal function with a scaling factor and an offset, i.e., $p(\theta, \phi) = A_1 \cos(\theta + \phi) + A_2$. Putting this expression into Eq. (3), however, it becomes clear that the parameter S is independent of both the scaling factor and offset and we find that the phase shift can be obtained as

$$\phi = \arctan(1 - 2S). \quad (4)$$

To investigate the precision obtained from the above construction, we measured a repeated acquisition of these three points with and without transport, for small changes to the current of the coils. An example of this is shown in Fig. 3(a), where each point is an average of all preceding points, and each error bar is the deviation of the last (averaged) point with respect to the previous points. If the measurement is quantum shot-noise limited, this error should converge toward a correct estimation of the phase shift with a rate proportional to \sqrt{N} , where N is the number of repetitions of the experiment.

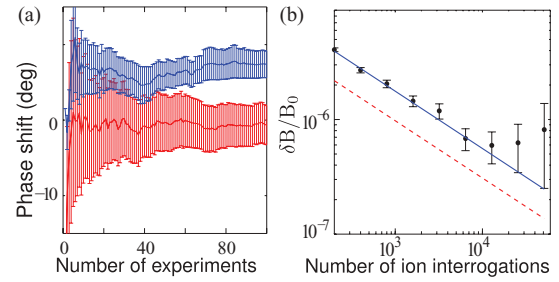


FIG. 3. (Color online) (a) Example measurement of a small magnetic field difference of 7 nT over $19 \mu\text{m}$ (upper blue curve) in comparison to a minimized gradient (lower red curve), where each of the 100 experimental points consists of 200 ion interrogations. (b) An Allan-type standard deviation over a larger data set (black dots) is plotted in comparison with the theoretical expectations using the values of the contrast going from 0.12 to 0.75 as realistic values (blue solid line) and using a perfect contrast (dashed red line), for the standard deviation coming from the quantum projection noise limit (see text). The y -axis scale represents the smallest magnetic field difference we can measure on top of the background of $B_0 = 0.7$ mT.

C. Allan variance and the quantum shot-noise limit

While Fig. 3(a) demonstrates how the phase shift with and without transport directly can be used to resolve small differences in the magnetic field, an Allan-type evaluation of the standard deviation gives a better estimate of the true rate of convergence. This is displayed in Fig. 3(b). To show that the main limitation of the experiment comes from quantum shot noise, we derive an expression for the quantum projection noise, caused by the projection on the spin states. This binary choice indicates that the uncertainty for each individual ion interrogation is given by the binomial distribution

$$\sigma_p(\phi) = \sqrt{p(\phi)[1 - p(\phi)]/N}, \quad (5)$$

where p is the probability of measuring spin up, and N is the total number of individual interrogations. As each data point consists of three actual measurements, the contributions to the error from all three projections must be taken into account. Gaussian error propagation then leads to an expression for the total error of the phase estimation:

$$\sigma_\phi = \sqrt{\sum_{\phi=0, \pi/2, \pi} \left(\frac{\delta\phi}{\delta p(\phi)} \sigma_p(\phi) \right)^2}, \quad (6)$$

where the partial derivatives can be obtained from Eqs. (3) and (4). The binomial standard deviations from Eq. (5) are used as errors together with values for $p(\phi)$ corresponding to having the three points come from a signal with realistic contrast going from 0.12 to 0.75 ($A_1 = 0.31$ and $A_2 = 0.44$), like the one seen in the inset to Fig. 2. We then obtain a limit of $\Delta\phi = 1.81 \text{ rad}/\sqrt{N}$, which is plotted in Fig. 3(b), converted into a corresponding relative magnetic field difference. In addition, the figure also displays the minimal obtainable error that could be reached if the spin-echo contrast would be perfectly 1. We find that the experimental data follows the quantum projection noise curve, which takes the limited contrast into account. From the above derivation it is also clear that the obtained accuracy is not limited by the time it takes to perform the

acquisition, but only by the number of interrogations, which is substantiated by the close proximity to the theoretical limit. This means that technical improvements, such as more efficient camera read out, can be used to reduce the time it takes for a full acquisition. As a reference, the plot in Fig. 3(a) contains in total 20 000 ion interrogations (for each of the three points), and with 5 ms detection time per interrogation, it took only on the order of minutes to acquire. After about 10^4 interrogations, we reach a relative magnetic field sensitivity of $\delta B/B \sim 5 \times 10^{-7}$. At this point the measured Allan deviation appears to deviate from the theoretically expected one. This behavior is attributed to long-term drifts of the experimental setup arising from, e.g., temperature variations in the magnetic field coils. The observed contrast loss can be explained by technical noise from the waveform generator that applies the transport pulse voltage, which leads to a small amount of motional heating. This problem can be solved by a better suited multichannel voltage source that can address all of the trap control segments. Time-dependent magnetic field fluctuations faster than the spin-echo time is further reducing the contrast, and such noise may be reduced by a passive shielding box of mu-metal around the trap setup. It can also be mentioned that it is possible to improve the sensitivity of the method by utilizing two or more ions in a spin-squeezed state, which can reduce the noise of the phase measurement even below the shot-noise limit [15].

Our value of the relative magnetic field sensitivity is comparable to that of other methods used for measuring magnetic fields, such as squids [16] or atomic vapors [17,18]. Though it may be noted that the other methods target different applications, and while those can reach higher absolute sensitivity, our method relies only on a single ion and can thus yield a very high spatial resolution, in the sub- μm range. Another potential application is the detection of the magnetic field from a single spin. Although it is currently difficult to

move the ion close enough (~ 100 nm) to the spin for adequate absolute sensitivity, it is interesting to note that our method has a similar relative sensitivity as magnetic resonance force microscopy [8], where single spin resolution has been reached.

IV. CONCLUSION

In conclusion, we have demonstrated a technique to use the transport of a single ion to detect magnetic field gradients with high resolution, both spatially and magnitude wise. Using the transport of the ion has the natural advantage that magnetic gradients in the entire trap, even regions inaccessible to the necessary lasers, can be minimized, which is expected to be very useful for ion traps used for scalable quantum computing. For a single transported ion, the minimum detectable phase shift suggests that a transported coherence time would be more than 10 ms, which is already long enough that the gradient is no longer the main limitation. The expected coherence time is even significantly longer if we consider a logical qubit in a decoherence-free subspace [6]. This entangled two-ion logical state is insensitive to magnetic field inhomogeneities, although a difference in the magnetic field between the two ions will still cause dephasing. Using the minimized gradient demonstrated here and assuming a reasonable ion separation of $4 \mu\text{m}$, we find a coherence time above 1 s. This time is long compared to the time of qubit gates as well as the expected transport durations; however, it is not so long that one does not realize the necessity of performing a compensation routine, like the one suggested here, for minimizing the magnetic field inhomogeneity.

ACKNOWLEDGMENTS

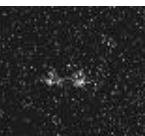
The authors thank Kilian Singer for helpful discussions. We acknowledge financial support by the IARPA project and by the European Commission within the IP AQUATE.

-
- [1] R. Blatt and D. Wineland, *Nature (London)* **453**, 1008 (2008).
 - [2] T. Monz, P. Schindler, J. T. Barreiro, M. Chwalla, D. Nigg, W. A. Coish, M. Harlander, W. Hansel, M. Hennrich, and R. Blatt, *Phys. Rev. Lett.* **106**, 130506 (2011).
 - [3] D. Kielpinski, C. Monroe, and D. Wineland, *Nature (London)* **417**, 709 (2002).
 - [4] J. P. Home *et al.*, *Science* **325**, 1227 (2009).
 - [5] R. B. Blakestad, C. Ospelkaus, A. P. VanDevender, J. M. Amini, J. Britton, D. Leibfried, and D. J. Wineland, *Phys. Rev. Lett.* **102**, 153002 (2009).
 - [6] D. Kielpinski *et al.*, *Science* **291**, 1013 (2001).
 - [7] M. Chwalla, K. Kim, T. Monz, P. Schindler, M. Riebe, C. Roos, and R. Blatt, *App. Phys. B* **89**, 483 (2007).
 - [8] D. Rugar, R. Budakian, H. J. Mamin, and B. W. Chui, *Nature (London)* **430**, 329 (2004).
 - [9] S. Knünz, M. Herrmann, V. Batteiger, G. Saathoff, T. W. Hansch, K. Vahala, and T. Udem, *Phys. Rev. Lett.* **105**, 013004 (2010).
 - [10] S. Wildermuth *et al.*, *Nature (London)* **435**, 440 (2005).
 - [11] S. Schulz, U. Poschinger, K. Singer, and F. Schmidt-Kaler, *Fortschr. Phys.* **54**, 648 (2006).
 - [12] G. Huber, F. Ziesel, U. G. Poschinger, K. Singer, and F. Schmidt-Kaler, *Appl. Phys. B* **100**, 725 (2010).
 - [13] U. G. Poschinger *et al.*, *J. Phys. B* **42**, 154013 (2009).
 - [14] K. Singer *et al.*, *Rev. Mod. Phys.* **82**, 2609 (2010).
 - [15] V. Meyer, M. A. Rowe, D. Kielpinski, C. A. Sackett, W. M. Itano, C. Monroe, and D. J. Wineland, *Phys. Rev. Lett.* **86**, 5870 (2001).
 - [16] M. I. Faley *et al.*, *Supercond. Sci. Technol.* **17**, 324 (2004).
 - [17] S. Groeger, G. Bison, J.-L. Schenker, R. Wynands, and A. Weis, *Eur. Phys. J. D* **38**, 239 (2006).
 - [18] I. K. Kominis, T. W. Kornack, J. C. Allred, and M. V. Romalis, *Nature (London)* **422**, 596 (2003).

6

Outlook

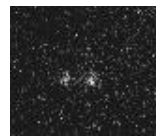
This diploma thesis described technological steps towards a realization of a scalable quantum computer. High fidelity qubit readout algorithms based on images provided by an EMCCD camera were investigated and implemented into the experimental control system. Further, the way towards fast transport was paved by implementing a software interface for fast PC to FPGA communication, allowing us to process voltage sequences at a maximum rate of 2.5 Megasamples. These tools permit us to advance onto a new level of experiments. The ability to fast, precisely and individually discriminate the state of a multi qubit system will allow us to perform fast state tomography of qubits and accurate readouts. Transport operations between different parts of the trap will enable us to operate with a set of *decoherence free* qubits encoded in odd Bell states. However, the steps towards a scalable quantum computer need to be taken one at a time. The stability of a two ion crystal needs to be improved by finding optimum trap operating parameters. Furthermore, various decoherence sources such as magnetic field or laser intensity fluctuations need a better suppression. The next conceivable aim would be the entanglement of two ions by the realization of a *geometric phase gate*. The transport sequences need to be optimized to fit the limitations of the experiment in order to transfer as little energy as possible to the ion. Further, lowpass filters need to be designed in a way that a balance between speed and noise suppression is met to avoid unnecessary heating. Calculations show that a fast transport beyond adiabatic limit is possible for a well controlled, time-dependent potential. Steps towards finding an optimum for fast transport were done and need to be continued.



6. OUTLOOK

References

- [And06] Andor, www.sens-tech.com. *iXon DV860 (back illuminated)*, 2006. 22
- [AVN11] AVNET, <http://www.em.avnet.com/>. *Xilinx Virtex-5 FXT Evaluation Kit*, 2011. 46
- [BBC⁺95] Adriano Barenco, Charles H. Bennett, Richard Cleve, David P. DiVincenzo, Norman Margolus, Peter Shor, Tycho Sleator, John A. Smolin, and Harald Weinfurter. Elementary gates for quantum computation. *Phys. Rev. A*, 52(5):3457–3467, Nov 1995. 2
- [BCJD99] Gavin K. Brennen, Carlton M. Caves, Poul S. Jessen, and Ivan H. Deutsch. Quantum logic gates in optical lattices. *Phys. Rev. Lett.*, 82(5):1060–1063, Feb 1999. 2
- [BHM03] A. G. Basden, C. A. Haniff, and C. D. Mackay. Photon counting strategies with low-light-level ccds. *Monthly Notices of the Royal Astronomical Society*, 2003. 23, 24
- [Blo06] Dr. Imanuel Bloch. Atom physics lecture, part i, 2006. 8, 10
- [Bro05] Ilja Bronstein. *Taschenbuch der Mathematik*, volume 6. Verlag Harri Deutsch, 2005. 20
- [CW08] John Clarke and Frank K. Wilhelm. Superconducting quantum bits. *Nature*, 453:1031–1042, June 2008. 2
- [CZ95] J. I. Cirac and P. Zoller. Quantum computations with cold trapped ions. *Phys. Rev. Lett.*, 74(20):4091–4094, May 1995. 1, 2, 3, 5
- [CZKM97] J. I. Cirac, P. Zoller, H. J. Kimble, and H. Mabuchi. Quantum state transfer and entanglement distribution among distant nodes in a quantum network. *Phys. Rev. Lett.*, 78(16):3221–3224, Apr 1997. 3
- [DBDM04] L.-M. Duan, B.B. Blinov, Moehring D.L., and C. Monroe. Scalable trapped ion quantum computation with a probabilistic ion-photon mapping. *Quantum Information and Computation*, 2004. 3
- [DiV00] David P. DiVincenzo. The physical implementation of quantum computation. *Fortschritte der Physik*, Feb 2000. 5
- [Dua04] L.-M. Duan. Scaling ion trap quantum computation through fast quantum gates. *Phys. Rev. Lett.*, 93(10):100502, Sep 2004. 3
- [FYV00] L. Fedichkin, M. Yanchenko, and K. A. Valiev. Novel coherent quantum bit using spatial quantization levels in semiconductor quantum dot. *ArXiv Quantum Physics e-prints*, jun 2000. 2
- [GRZC03] J. J. García-Ripoll, P. Zoller, and J. I. Cirac. Speed optimized two-qubit gates with laser coherent control techniques for ion trap quantum computing. *Phys. Rev. Lett.*, 91(15):157901, Oct 2003. 3

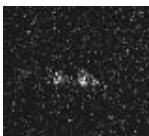


REFERENCES

- [HHR⁺05] H. Haffner, W. Hansel, C. F. Roos, J. Benhelm, D. Chek-al kar, M. Chwalla, T. Korber, U. D. Rapol, M. Riebe, P. O. Schmidt, C. Becher, O. Guhne, W. Dur, and R. Blatt. Scalable multiparticle entanglement of trapped ions. *Nature*, 438:643–646, Dez 2005. 3
- [JBT⁺09] M. Johanning, A. Braun, N. Timoney, V. Elman, W. Neuhauser, and Chr. Wunderlich. Individual addressing of trapped ions and coupling of motional and spin states using rf radiation. *Phys. Rev. Lett.*, 102(7):073004, Feb 2009. 3
- [JKMW01] Daniel F. V. James, Paul G. Kwiat, William J. Munro, and Andrew G. White. Measurement of qubits. *Phys. Rev. A*, 64(5):052312, Oct 2001. 14
- [KW02] C. Kielpinski, D. Monroe and D. J. Wineland. Architecture for a large-scale ion-trap quantum computer. *Nature*, 417:709–711, June 2002. 7
- [LCW98] D. A. Lidar, I. L. Chuang, and K. B. Whaley. Decoherence-free subspaces for quantum computation. *Phys. Rev. Lett.*, 81(12):2594–2597, Sep 1998. 2
- [LD98] Daniel Loss and David P. DiVincenzo. Quantum computation with quantum dots. *Phys. Rev. A*, 57(1):120–126, Jan 1998. 2
- [LDM⁺03] D. Leibfried, B. DeMarco, V. Meyer, D. Lucas, M. Barrett, J. Britton, W. M. Itano, B. Jelenkovic, C. Langer, T. Rosenband, and D. J. Wineland. Experimental demonstration of a robust, high-fidelity geometric two ion-qubit phase gate. *Nature*, March 2003. 14, 15
- [Mai06] Robert Maiwald. Abbildungs- und steuerungssystem für ein experiment mit einzelnen ionen. Master's thesis, University of Ulm, 2006. 20
- [Mar03] Florian Markowetz. Klassifikation mit support vector machines, 2003. 37
- [MMO⁺07] D. L. Moehring, P. Maunz, S. Olmschenk, K. C. ounge, D. N. Matsukevich, L.-M. Duan, and C. Monroe. Entanglement of single-atom quantum bits at a distance. *Nature*, July 2007. 3
- [Mon02] C. Monroe. Quantum information processing with atoms and photons. *Nature*, March 2002. 2
- [MSB⁺11] Thomas Monz, Philipp Schindler, Julio T. Barreiro, Michael Chwalla, Daniel Nigg, William A. Coish, Maximilian Harlander, Wolfgang Hänsel, Markus Hennrich, and Rainer Blatt. 14-qubit entanglement: Creation and coherence. *Phys. Rev. Lett.*, 106(13):130506, Mar 2011. 3, 7, 45
- [MSW⁺08] A. H. Myerson, D. J. Szwer, S. C. Webster, D. T. C. Allcock, M. J. Curtis, G. Imreh, J. A. Sherman, D. N. Stacey, A. M. Steane, and D. M. Lucas. High-fidelity readout of trapped-ion qubits. *Phys. Rev. Lett.*, 100(20):200502, May 2008. 24, 27, 41
- [MTS85] K. Matsuo, M.C. Teich, and B.E.A. Saleh. Noise properties and time response of the staircase avalanche photodiode. *Electron Devices, IEEE Transactions*, 1985. 23
- [MW01] Florian Mintert and Christof Wunderlich. Ion-trap quantum logic using long-wavelength radiation. *Phys. Rev. Lett.*, 87(25):257904, Nov 2001. 3
- [NC03] Michael A. Nielsen and Isaac L. Chuang. *Quantum Computation and Quantum Information*, volume 6. Cambridge University Press, 2003. 12
- [NMR⁺08] P. Neumann, N. Mizuochi, F. Rempp, P. Hemmer, H. Watanabe, S. Yamasaki, V. Jacques, T. Gaebel, F. Jelezko, and J. Wrachtrup. Multipartite entanglement among single spins in diamond. *Science*, 320(5881):1326–1329, 2008. 2

REFERENCES

- [NRR⁺00] H.C. Nagerl, C. Roos, H. Rohde, D. Leibfried, J. Escher, F. Schmidt-Kaler, and R. Blatt. Addressing and cooling of single ions in paul traps. *Fortschritte der Physik*, 2000. 55
- [PE04] Francesco Pampaloni and Joerg Enderlein. Gaussian, hermite-gaussian, and laguerre-gaussian beams: A primer. oct 2004. 56
- [Pos09] U. G. et. al. Poschinger. Coherent manipulation of a 40Ca^+ spin qubit in a micro ion trap. *Journal of Physics B*, July 2009. 62
- [Pos11] Ulrich Poschinger. *Quantum Optics Experiments in a Microstructured Ion Trap*. PhD thesis, University of Ulm, 2011. 16, 17, 21, 59
- [Pre07] H. William Press. *Numerical Recipes - The Art of Scientific Computing*, volume Third Edition. Cambridge Press, 2007. 88
- [RBKD⁺02] M. A. Rowe, A. Ben-Kish, B. Demarco, D. Leibfried, V. Meyer, J. Beall, J. Britton, J. Hughes, W. M. Itano, B. Jelenkovic, C. Langer, T. Rosenband, and D. J. Wineland. Transport of Quantum States and Separation of Ions in a Dual RF Ion Trap. *Quantum Information and Computation*, may 2002. 7
- [RLB⁺06] R. Reichle, D. Leibfried, R. B. Blakestad, J. Britton J. D. Jost, E. Knill, C. Langer, R. Ozeri, S. Seidelin, and D. J. Wineland. Transport dynamics of single ions in segmented microstructured paul trap arrays. *Progress of Physics*, 54:666, 2006. 51
- [Roo00] Christian Roos. *Controlling the quantum state of trapped ions*. PhD thesis, Leopold-Franzens-University Innsbruck, 2000. 29
- [Sch09] Stephan Schulz. *Scalable Microchip Ion Traps for Quantum Computation*. PhD thesis, University of Ulm, 2009. 7, 8, 22, 46
- [Sch10] Wolfgang Schnitzler. *Deterministic ultracold ion source targeting the Heisenberg limit*. PhD thesis, University of Ulm, 2010. 20
- [Sen10] Sens-Tech, www.sens-tech.com. *Photodetector Module P25PC*, 2010. 25
- [Sho95] Peter W. Shor. Scheme for reducing decoherence in quantum computer memory. *Phys. Rev. A*, 52(4):R2493–R2496, Oct 1995. 2
- [SPM⁺10] K. Singer, U. G. Poschinger, M. Murphy, P. A. Ivanov, F. Ziesel, T. Calarco, and F. Schmidt-Kaler. Colloquium: Trapped ions as quantum bits: Essential numerical tools. *Review of Modern Physics*, 82:2609, 2010. 49, 50
- [Tex06] Texas Instruments, <http://focus.ti.com/docs/prod/folders/print/dac8814.html>. *DAC8814. 16-Bit, Quad, Serial Input Multiplying Digital to Analog Converter*, 2006. 47
- [VSB⁺01] Lieven M. K. Vandersypen, Matthias Steffen, Gregory Breyta, Costantino S. Yannoni, Mark H. Sherwood, and Isaac L. Chuang. Experimental realization of shor’s quantum factoring algorithm using nuclear magnetic resonance. *Nature*, Dez 2001. 2
- [Wel11] Jens Welzel. Planare spin-spin simulatoren. Master’s thesis, University of Ulm, 2011. 17
- [WWKR07] Tatjana Wilk, Simon C. Webster, Axel Kuhn, and Gerhard Rempe. Single-atom single-photon quantum interface. *Science*, 317(5837):488–490, 2007. 3



REFERENCES

Appendix A

Implementation of Camera into Control Program - MyCam

On creating the MyCam Object a connection to the camera is build up, accessing camera properties and setting values on default:

The maximum resolution parameters of the cam are stored in: `long __MAX_RES_X` and `long __MAX_RES_Y` and can be accessed using `getResX()` and `getResY()` with a total array size `__SIZE` which can be retrieved using `getSize()`

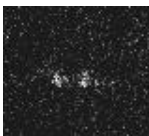
Three arrays are allocated to store image informations.

```
_dataImg = new long[__SIZE];  
_drawImg = new long[__SIZE];  
_buffer = new long[__SIZE];
```

`_buffer` is used to store incoming data from the camera. `_dataImg` holds real **unmanipulated** data (pixel values unchanged - might be rotated image) `_drawImg` holds data to be drawn on the gui. To that array filters may be added without changing the **real** image data (e.g. Gaussian filter etc.).

Temperature limits of the camera are stored in `int __MIN_TEMP` and `int __MAX_TEMP`
EMCCD gain limits are stored in `int __MIN_EMCCD_GAIN` and `int __MAX_EMCCD_GAIN`

On creation of the `MyCam` object the camera is setup to operate at 0.01s exposure time and is initialized to be operated in video mode with disabled cooler. A set of function is designed in a way that the `MyCam` object can be created with an `EXPORT` flag to allow MCP direct access without the necessity of programming functions in the `ScriptDLL`. Every retrieved image is searched for a maximum and minimum pixel count number



A. IMPLEMENTATION OF CAMERA INTO CONTROL PROGRAM - MYCAM

and the corresponding value and index are stored in `long _maxCnt` and `long _maxCntIdx` respectively the min counts.

Listing A.1: List of exported camera commands

```
// Temperature control
SETGETFN(int,tempControl,setTemp,getTemp);

// Temperature lock
GETFN(bool, isTempStable, getTempStable);

// Cooler control
SETGETFN(bool,CoolerControl,setCooler,getCooler);

// EM gain control
SETGETFN(double,EMCCDGainCtrl,setEMCCDGain, getEMCCDGain);

// Baseline clamp control
SETGETFN(bool,BaseLineClamp,setBaselineClamp, getBaselineClamp);

// Baseline offset
SETGETFN(int,BaseLineOffset,setBaselineOffset, getBaselineOffset);

// Button to print index of pre amp and shiftspeeds
void getSettings() {getPreAmpGains(); getVSSpeeds(); getHSSpeeds();};

// Vertical shiftspeed control
void VertShiftSpeed(int idx){setVSSpeed(idx)};

// Horizontal shiftspeed control
void HorShiftSpeed(int idx){setHSSpeed(idx)};

// Preamp control
void PreAmpGain(int idx){setPreAmpGain(idx)};

// Exposure time control
SETGETFN(double,exposureTime,setExpTime, getExpTime);

// Accumulation cycle control
SETGETFN(double,AccCycleTime,setAccTime, getAccTime);

// Kinetic cycle control
SETGETFN(double,KinCycleTime,setKinTime, getKinTime);
```

```
// Shutter buttons.
void shutterOpen() {openShutter();};
void shutterClose() {closeShutter();};

// Subimage mode switch
SETGETFN(bool, subImageMode, setSubImageMode, getSubImageMode);

// Full vertical binning switch
SETGETFN(bool, fullVerticalBinning, setFullVertBin, getFullVertBin);
```

This set of functions can directly be accessed by mere creation of the `MyCam` object in the `ScriptDLL`. A list of functions provided by the `MyCam` object is listed in next paragraph and can be used in any desired way.

A.1 Function List

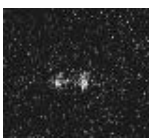
Listing A.2: List of camera commands

```
/*
  Returns the maximum pixel number along x direction.
*/
int getResX()

/*
  Returns the maximum pixel number along y direction.
*/
int getResY()

/*
  Returns the size of the image array.
*/
int getSize()

/*
  Function adjusts the readout window to a sub region of the full CCD
  chip defined by corners [xl,yb] and [xr,yt]. The input is accepted as
  double and converted to int due to GUI. The input is clamped to fit
  maximum range of the camera. The coordinate systems origin is lower
  left corner (0,0)
*/
```



A. IMPLEMENTATION OF CAMERA INTO CONTROL PROGRAM - MYCAM

```
void setSubImageRange(double xl, double xr, double yb, double yt)

/*
  Returns current settings of the subImage Range
*/
void getSubImgProps(int *xl, int *xr, int *yb, int *yt, int *rows, int
*cols)

/*
  Returns the size of the current subImage array.
*/
int getSubImgSize() {return __size_sub;};

/*
  Enables subimage mode of the camera. The area needs to be adjusted
  using setSubImageRange. If no region is set a default region [30,30]-
  [MAX_X-30, MAXY-30] is used. if mode = false full CCD chip is read out.
*/
void setSubImageMode(bool mode)

/*
  Switches full vertical binning of camera pixels. Can be combined with
  subImageMode.
*/
void setFullVertBin(bool mode)

/*
  Opens shutter of the camera. Should not be used in a loop!
*/
void openShutter()

/*
  Closes shutter of the camera. Should not be used in a loop!
*/
void closeShutter()

/*
```

A.1 Function List

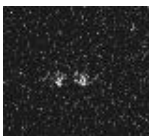
```
Sets the camera to operate in kinetic mode. The function takes into account the settings from subImageMode / fullVerticalBinning and timings (expose time and kinetic cycle time).It allocates required array for the amount of images which are stored in _acquiredDataSeries. After takeSignal finished all images are stored on the internal camera memory and getAcquiredSequenceData will store image series into this array. The function prints max amount of images onto the console.
@param kinSerLen amount of images taken in a single kinetic series.
If the number of images exceed internal memory a warning will appear in the console since the circular buffer would overwrite images.
@param extTrigger true if each image of the sequence is to be taken with a trigger. If not all triggers are send the camera will pend waiting for triggers to complete the series. To abort the abortAcquisition command can be used.
*/
void prepareTriggeredKinetic(int kinSerLen, bool extTrigger)

/*
Sets the camera to operate in video mode. All images are stored in the circular buffer of the camera the newest can be obtained using getMostRecentImage. The function takes into account the settings from subImageMode / fullVerticalBinning and exposure time.
*/
void prepareVideoMode()

/*
Starts a prepared acquisition. Note that the camera cannot change its parameters (e.g. exposure time, imaging area etc.) while acquiring.
*/
void takeSignal()

/*
Ends any acquisition the camera is working on.
*/
void abortAcquisition()

/*
Retrieves series of images from camera storing them into array allocated by prepareTriggeredKinetic
*/
```



A. IMPLEMENTATION OF CAMERA INTO CONTROL PROGRAM - MYCAM

```
void getAcquiredSequenceData()

/*
  Takes a given image number and copies data into _dataImg to deliver a
  single image of a series. You have to make sure imgNum is a valid
  imageNumber. Yet no check is done to prevent out of bounds exception!
*/
void getImgFromAcquiredData(double imgNum)

/*
  Saves most recent image acquired by the camera into _dataImg.
  Rotations are taken into account.
*/
void getMostRecentImage()

/*
  Copies _dataImg into _drawImg. Feel free to modify this function to be
  able to apply filters. etc. to the image.
*/
void updateDrawImage(bool postProcessing)

/*
  Returns number of images acquired. You can use this number to make
  sure not to access invalid images of a sequence taken. In video mode
  this number is always incremented (the cam itself holds this number,
  here I just call this number)
*/
long getTotalNumberImagesAcquired()

/*
  Returns true if camera acquired an new image since the last time
  getMostRecentImage was called. (in video mode you can make sure not to
  read out one and the same image over and over again)
*/
bool hasNewImage()

/*
  Returns an integer value of the camera status. See vendor reference
  for the numbers.
```

A.1 Function List

```
*/
int getStatus()

/*
  Returns true if the camera is acquiring.
*/
bool isAcquiring()

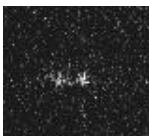
/*
  Produces a console output of possible gain settings. The setting
  itself is set using a number which corresponds to a given pre-amp gain.
*/
void getPreAmpGains()

/*
  Function to adjust the pre amplification gain. To obtain possible idx
  values call getPreAmpGains or see user's manual of the camera.
*/
setPreAmpGain(int idx)

/*
  Returns the currently set pre amplification gain.
*/
int getPreAmpGain()

/*
  Produces a console output of possible vertical shift settings. The
  setting itself is set using a number which corresponds to a given
  shift speed.
*/
getVSSpeeds()

/*
  Function to adjust the vertical shift speed. To obtain possible idx
  values call getVSSpeeds or see user's manual of the camera.
*/
setVSSpeed(int idx)
```



A. IMPLEMENTATION OF CAMERA INTO CONTROL PROGRAM - MYCAM

```
/*
    returns the index of the currently set vertical shift speed.
*/
int getVSSpeed()

/*
    Produces a console output of possible horizontal shift settings. The
    setting itself is set using a number which corresponds to a given
    shift speed.
*/
getHSSpeeds()

/*
    Function to adjust the horizontal shift speed. To obtain possible idx
    values call getHSSpeeds or see user's manual of the camera.
*/
setHSSpeed(int idx)

/*
    Returns the index of the currently set vertical shift speed.
*/
getHSSpeed()

/*
    Function to adjust the electron multiplication gain. The input value
    is clamped to camera specifications. You cannot exceed specs. Double
    is used for GUI purpose. The function itself converts val to an
    integer.
*/
setEMCCDGain(double val)

/*
    Returns the currently set EM gain. Double is used for GUI purpose
*/
double getEMCCDGain()

/*
    Function to adjust CCD chip temperature. The input values are clamped
    to camera specifications. The cooling to the desired temperature will
```

A.1 Function List

```
    start as soon as setCooler(true) is set.
*/
setTemp(int t)

/*
    Returns the currently set target temperature of the CCD chip.
*/
int getTemp()

/*
    Enables the cooling of the CCD. true = on.
*/
setCooler(bool on)

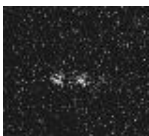
/*
    Returns true if the cooler is enabled.
*/
bool getCooler()

/*
    Returns true if the cooler is in lock.
*/
bool getTempStable()

/*
    Adjusts baseline clamping (see manual for more details). True = on
*/
setBaselineClamp(bool on)

/*
    Returns true if the baseline clamp is on
*/
bool getBaselineClamp()

/*
    Adjusts the baseline offset (see manual for more details). Value is
    clamped to a range of [-1000,1000]. Intercombination of clamp and
    offset is not possible.
```



A. IMPLEMENTATION OF CAMERA INTO CONTROL PROGRAM - MYCAM

```
*/
setBaselineOffset(int off)

/*
  Setter and getter of the exposure time. The value is clamped by
  cameras limits.
*/
setExpTime(double t)
double getExpTime()

/*
  Setter and getter of accumulation time. The value is clamped by
  cameras limits.
*/
setAccTime(double t)
getAccTime()

/*
  Setter and getter of the a single kinetic cycle time. The value is
  clamped by cameras limits.
*/
setKinTime(double t)
getKinTime()
```

A.2 Example Code

However, to visualize the camera data the MCP provides one with some widgets. The camera image can be rendered using an OpenGL environment where a square $\{-1,-1\}$, $\{1,1\}$ is drawn. The retrieved camera image which is stored in an array is processed in a way that it can be placed as a texture on that square.

Listing A.3: Creating a camera GUI object - Data2DPlotArray

```
/*
  main variable for handling the camera
*/
EXPORT MyCam iXon;

/*
  main variables to handle regions of interest
```

```

*/
  int regArrSize = 16;
  double *regArr = new double[regArrSize];

  /*
   main variable for openGL image
  */
  EXPORT Data2DPlotArray
  camImg(iXon.getResX(),iXon.getResY(),iXon._drawImg, regArrSize,
  regArr);

```

The `Data2DPlotArray` object has been extended with a variable `regArrSize` to provide the user with the ability to control 'Regions of Interest' by drawing squares on the openGL GUI. At the moment four regions of interest are implemented into the MCP

- sub image region of interest. Shortcut 'S'
- general purpose region of interest. (can only be set in a cpp program and visualized by switching with 'A')
- region of interest 1. Shortcut '1'
- region of interest 2. Shortcut '2'

which **openGL** coordinates are stored in the array provided by `double *regArr`. To draw a square the openGL widget needs to have the focus (just clicking on it). Holding a shortcut and the left mouse button will allow you to draw a square which is instantly drawn on the screen. Having a drawn ROI it can be *moved* using the shortcut button and the *middle mouse* button. The coordinates however are referred to the openGL system and need to be rescaled into the camera coordinate system. Two functions are provided to transform the coordinate systems:

`void regToPix(double *r1, int *r2)` and
`void pixToReg(int *r1, double *r2)` where first function transforms from openGL region coordinates to camera pixel coordinates and the second function vice versa. Note that the image array passed on to the openGL object `Data2DPlotArray` is the `_drawImg` variable.

The created link of camera and GUI in A.3 does not mean that the GUI is constantly updated with the newest image from the camera. Therefore the GUI needs to be



A. IMPLEMENTATION OF CAMERA INTO CONTROL PROGRAM - MYCAM

refreshed once the camera has a new image. Here a short example clarifies how to update the GUI with the camera running in video mode.

Listing A.4: How to use the camera in video mode

```
/*
  video button for constant GUI updating
*/
EXPORT void startVideo() {
  try {
    iXon.prepareVideoMode();
    iXon.takeSignal();
    videoRunning = true;
    int *rP = new int[regArrSize]; //regions in Pixel coord
    regToPix(regArr, rP);          //convert

    while (videoRunning) {
      if(iXon.getTotalNumberImagesAcquired()>0 && iXon.hasNewImage()) {
        iXon.getMostRecentImage();
        iXon.updateDrawImage(true);

        //-----
        if(updateBinningPlot) {
          //pushing entrys of counterPlot one to the left...
          for (int i=0; i<cntPlotSize-1; i++) {
            cntPlotY[i] = cntPlotY[i+1];
          }
          regToPix(regArr, rP);
          cntPlotY[cntPlotSize-1] = sumInROI(rP[8], rP[10], rP[9], rP[11]);
          camCntPlot.update();
        }
        //-----
        camImg.autoScale();
        camImg.update();
      }
    }
  }
  catch(CameraException e) { e.Show("<Start Video Button"); }
}
```

Listing A.5: How to use the camera in kinetic mode

```
/**
  *@brief starts kinetic series.
  *@param imgNumber number in this kinetic series.
```

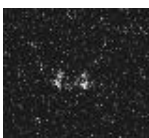
A.2 Example Code

```
    *@param extTrigger external or internal triggering (true = external
    trigger)
    *@param expTime exposure time for the kinetic series.
*/
EXPORT void startTriggeredKinetics(double imgNumber, bool extTrigger,
double expTime) {
    try {
        doingSequence = true;
        if (iXon.isAcquiring())
            iXon.abortAcquisition();
        int num = (int)imgNumber;
        iXon.prepareVideoMode();    //without this command the cam wont do
        anything if after a
                                   //fresh started program a sequence is
        taken directry without video... dunno
        why ?
        iXon.setExpTime(expTime);
        iXon.prepareTriggeredKinetic(num, extTrigger); //prepares camera
        and starts acquisition...
        iXon.takeSignal();
    }
    catch(CameraException e) { e.Show("<startTriggeredKinetics"); }
}

/**
*@brief acquires the data from the kinetic series...
*/
EXPORT void acquireTriggeredKineticData() {
    try {
        cout << "<<< Images Acquired : " <<
        iXon.getTotalNumberImagesAcquired() << endl;

        iXon.getAcquiredSequenceData();    //stores Data in
        internal array of MyCam...

        if (videoRunning) {
            iXon.prepareVideoMode();
            iXon.takeSignal();
        }
        doingSequence= false;
    }
    catch(CameraException e) { e.Show("<stopTriggeredKinetics"); }
}
```



A. IMPLEMENTATION OF CAMERA INTO CONTROL PROGRAM - MYCAM

Listing A.6: Fitting routine applied to an image

```
fitting routine pseudocode
```

A.3 Fitting Routine

For future flexibility using the new experimental control system a **Levenberg-Marquardt** fitting algorithm has been implemented into the software. The algorithm itself was implemented as described in (Pre07) and uses gradients to efficiently find an optimum. However, here a brief presentation of how to retrieve starting values for the algorithm is given in order to fit a Gaussian onto a curve. Since we are working with ions it is of interest how many ions are in the image and where they are situated. EXPORT `int`

```
autoTrackIons(double threshHold, bool feedBack, bool calculateCurve)
```

To first obtain the number we mark the brightest point of the image and its coordinates (fortunately the `MyCam` object already provides us with that information for every image).

Putting a cross through the brightest pixel we obtain two traces along the x and y axis directions where the ion (or ions) are situated. Since the traces are noisy we apply a smoothing **Binomial filter** with a size of five to avoid recognition of several peaks on one real peak. To separate peaks from the background a threshold σ_{new} is defined using convex combination of averaged background and brightest count

$$\sigma_{\text{new}} = \text{counts}_{\text{avg}} * (1 - \sigma_{\text{user}}) + \text{counts}_{\text{max}} * \sigma_{\text{user}};$$

which the user can define by adjusting a threshold σ_{user} between zero and one. The actual peak is situated where the left and right count are lower than the actual count (here one sees why it is important to first smoothen the traces). Using the pre-detected x- and y peaks by the above described algorithm the Levenberg-Marquardt algorithm is used to fit a Gaussian shape onto the traces. **Note this algorithm can only be used if the ions are aligned along the x- or y-axis.**

Appendix B

Implementation of Arbitrary Waveform Generator - myAnalogOutLine

First i briefly explain how a DAC8814 needs to be programmed in order to understand how the `myAnalogOutLine` class works. Figure B.1 show a schematic of the programming

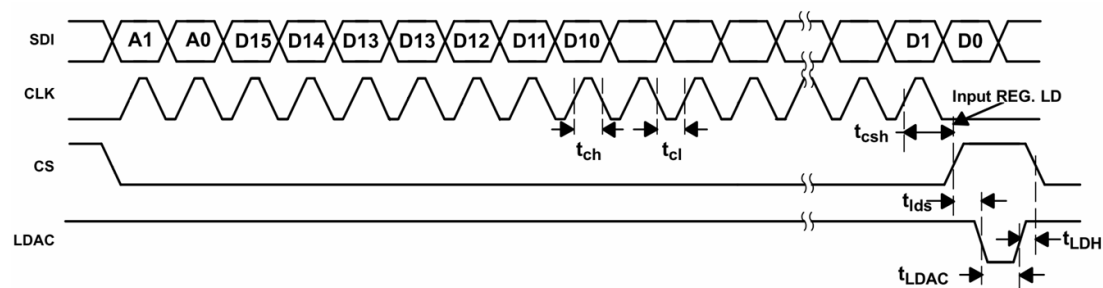
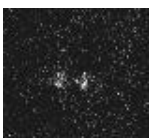


Figure B.1: Scheme of DAC programming.

register of the DAC. Most significant bits A0 and A1 are used to address one of the four channels of the DAC (two bits \rightarrow four combinations \rightarrow four channels) followed by 16 bits representing the output value of the DAC. Note that since the DAC has a shift register it pushes the bits internally every clock cycle. Therefore the programming needs to start with most significant bits. The limiting parameters given by Texas Instruments are:

- t_{ch} clock high : 10 ns



B. IMPLEMENTATION OF ARBITRARY WAVEFORM GENERATOR - MYANALOGOUTLINE

- t_{cl} clock low : 10 ns
- t_{csh} chip select holdoff : 10 ns
- t_{lds} low dac hold off : 5 ns.
- t_{LDAC} Low DAC pulse duration : 25 ns.
- t_{LDH} Low DAC Chip-select holdoff: 10 ns.

However, due to technical switching time limitations of the FPGA (currently 20 ns; maximum 10 ns), the timings of the current version derive from specifications.

- $t_{LDAC} = 20$ ns : is 5 ns shorter than specification.
- $t_{lds} = 20$ ns : 15 ns longer than specification.
- $t_{LDH} = 0$ ns : 10 ns!!! shorter than specification.

One could easily adjust the protocol to match the specifications but one would lose 2×20 ns resulting in a total programming cycle of 440 ns. However the output of the DAC still seems to be stable and using the new version of the FPGA where switching times of 10 ns are possible would allow us to better match the specification without losing to much time.

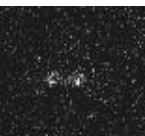
- $t_{LDAC} = 30$ ns : is 5 ns longer than specification.
- $t_{lds} = 10$ ns : 5 ns longer than specification.
- $t_{LDH} = 10$ ns : match.

Knowing how the DAC needs its data and how the FPGA is wired to each DAC B.1 allows us to program the required lines of the FPGA. A single DAC requires five input lines:

- clock line (CLK)
- chip select line (CS)
- data line (SDI)
- *fire* line (LDAC)

Virtex 5 Pin	SAM Name	JP6 Pin	MCP Bit	Function
Y6	SAM_OE#	13	62	none
Y5	SAM_A0	15	61	CS8
Y4	SAM_WE#	16	60	LOAD
W6	SAM_A2	17	59	CS9
V7	SAM_A1	18	58	SDI8
W5	SAM_A3	20	57	SDI9
F5	SAM_D0	21	56	CS0
V6	SAM_D2	23	55	CS1
U7	SAM_D1	24	54	SDI0
U6	SAM_D4	25	53	CS2
U5	SAM_D3	26	52	SDI1
T7	SAM_D6	27	51	CS3
T5	SAM_D5	28	50	SDI2
R7	SAM_D8	29	49	CS4
R6	SAM_D7	30	48	SDI3
P6	SAM_D10	31	47	CS5
R5	SAM_D9	32	46	SDI4
N6	SAM_D12	33	45	CS6
P8	SAM_D11	34	44	SDI5
K5	SAM_D14	35	43	CS7
M7	SAM_D13	36	42	SDI6
K6	SAM_A4	37	41	CS10
L7	SAM_D15	38	40	SDI7
J6	SAM_A6	39	39	CS11
J5	SAM_A5	40	38	SDI10
H4	SAM_IRQ	41	37	SDI11
H6	SAM_RESET#	43	36	RESET
??	SAM_BRDY	??	??	ext. trigger

Table B.1: FPGA MCP and DAC wire names in order to find the required line.



B. IMPLEMENTATION OF ARBITRARY WAVEFORM GENERATOR - MYANALOGOUTLINE

- reset line (RESET)

where LDAC and RESET lines are shared. The clock is provided by the FPGA and therefore does not need to be created additionally. Having these information we can **group** a set of **digital** lines in order to obtain four **analog** outputs. Now we have all required informations to begin with the programming part.

To program the FPGA we first require a connection. This is given by creating a port the PC communicates with the FPGA.

```
CDigitalOutFPGA fpgaPort()
```

Here a physical address of the Ethernet card is used to build up a connection. Having this port we can create **digital** lines leading to a given FPGA output (see table B.1).

```
CDigitalOutLine RESET
CDigitalOutLine LDAC
CDigitalOutLine CS0
CDigitalOutLine SDI0
:
```

This digital outputs are used to create **analog** outputs.

```
myAnalogOutLine C0D0S0(RESET, LDAC, CS0, SDI0, 0);
myAnalogOutLine C0D0S1(RESET, LDAC, CS0, SDI0, 1);
myAnalogOutLine C0D0S2(RESET, LDAC, CS0, SDI0, 2);
myAnalogOutLine C0D0S3(RESET, LDAC, CS0, SDI0, 3);
```

Here it is useful to stick to the following naming: Card[0,3]Dac[0,2]Signal[0,3] since the backboard is designed in a way where the outputs of the subD25 output of each card are as shown in figure B.2.

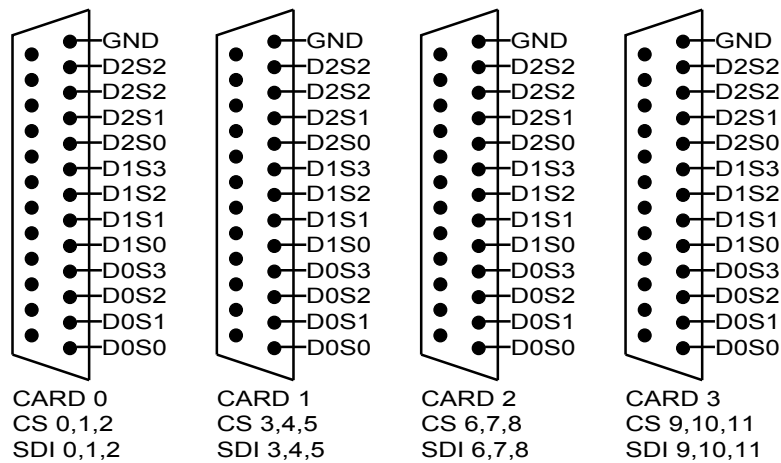


Figure B.2: Scheme of the outputs of arbitrary waveform generator.

B.1 Function List

The `myAnalogOutLine` objects has only a little set of functions since its basic function is only to provide an appropriate digital sequence to the FPGA port.

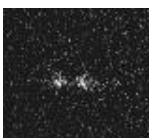
Listing B.1: `myAnalogOutLine` class

```
//constructors and destructors
myAnalogOutFPGA(CDigitalOutLine &CSL,
                CDigitalOutLine &DIL,
                CDigitalOutLine &RESETL,
                CDigitalOutLine &LDAACL,
                int subDacNr,
                bool inverted = false,
                double minV = -10,
                double maxV = 10);

myAnalogOutFPGA();
~myAnalogOutFPGA();

/*
static setter functions. the value is immediately executed.
*/
void set(double val);
void set(bool val);
void set(int val);

/*
sequenced setter. adds required voltage to a sequence of digital
pulses.
```



B. IMPLEMENTATION OF ARBITRARY WAVEFORM GENERATOR - MYANALOGOUTLINE

```
*/
void set(double t, double val, CSequenceFPGA &seq);
void set(double t, int val, CSequenceFPGA &seq);
void set(double t, bool val, CSequenceFPGA &seq);

/*
getter of the latest set value
*/
double get(void) {return _value;};

/*
setter/getter of lines to program dac with.
*/
void setCS(CDigitalOutLine &CS);
void setDI(CDigitalOutLine &DI);
void setRESET(CDigitalOutLine &RESET);
void setLDAC(CDigitalOutLine &LDAC);

CDigitalOutLine* getCS(void) {return _CSLINE;};
CDigitalOutLine* getDI(void) {return _DILINE;};
CDigitalOutLine* getRESET(void) {return _RESETLINE;};
CDigitalOutLine* getLDAC(void) {return _LDACLINE;};

/*
setter/getter of DAC channel
*/
void setSubDacNr(int subDac);
int getSubDacNr(void);

/*
setter/getter of voltage range (for booster cards)
*/
void setMinVoltage(double min);
void setMaxVoltage(double max);
double getMinVoltage(void);
double getMaxVoltage(void);

/*
the voltage can be set to inverted mode (if the analog output is
abused as a digital TTL output)
*/
void setInverted(bool v);
bool getIsInverted(void);
```

LDacC

B.2 Example Code

Listing B.2: create a FPGA connection and analog lines

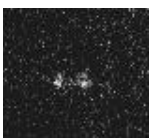
```
//digital port
CDigitalOutFPGA
fpgaPort("\\DEVICE\\{35DFA55F-B9AE-4F59-B47E-5286DA0FBA67}",
FPGAPortDigital, 0xFFFFFFFFFFFFFFFF, 64, true);

//Reset and LDAC are common for all Cards and all Dacs
CDigitalOutLine FPGABitLDAC (LDAC, fpgaPort);
CDigitalOutLine FPGABitRESET (RESET, fpgaPort);
// Card 0
// digital Lines for dac 0
CDigitalOutLine FPGABitC0CS0 (CH0_CS0, fpgaPort);
CDigitalOutLine FPGABitC0DI0 (CH0_DAC0, fpgaPort);

//Card 0
//Dac 0
EXPORT myAnalogOutFPGA C0D0S0(FPGABitC0CS0, FPGABitC0DI0, FPGABitRESET,
FPGABitLDAC, 0);
EXPORT myAnalogOutFPGA C0D0S1(FPGABitC0CS0, FPGABitC0DI0, FPGABitRESET,
FPGABitLDAC, 1);
EXPORT myAnalogOutFPGA C0D0S2(FPGABitC0CS0, FPGABitC0DI0, FPGABitRESET,
FPGABitLDAC, 2);
EXPORT myAnalogOutFPGA C0D0S3(FPGABitC0CS0, FPGABitC0DI0, FPGABitRESET,
FPGABitLDAC, 3);
```

Listing B.3: simple sequence of analog values - slow

```
/*
   Simple function setting sequenced values of one DAC
*/
EXPORT void sequencedSet() {
    CSequenceFPGA seq(fpgaPort); //sequence
    fpgaPort.setLDacChn(3); //slow mode
    fpgaPort.setAnalogTimebase(1600e-9); //4*400ns
    double t=.0;
    for (int i=0; i<=10; i++) {
        C0D0S0.set(t, i, seq);
    }
}
```



B. IMPLEMENTATION OF ARBITRARY WAVEFORM GENERATOR - MYANALOGOUTLINE

```
        CODOS1.set(t,-i, seq);
        CODOS2.set(t, i, seq);
        CODOS3.set(t,-i, seq);
        t+=fpgaPort.getAnalogTimebase();
    }
    seq.genTimingTable("c:/tmp_"); //prints table of data
    seq.start(); //starts
    seq.release(); //doent work yet.
}
```

Listing B.4: simple sequence of analog values - fast

```
/*
   Simple function setting sequenced values of one DAC
*/
EXPORT void sequencedSet() {
    CSequenceFPGA seq(fpgaPort); //sequence
    fpgaPort.setLDacChn(0); //fast mode
    fpgaPort.setAnalogTimebase(400e-9); //in slow mode i need 4*400ns
    for full sequence
    double t=.0;
    for (int i=0; i<=10; i++) {
        CODOS0.set(t, i, seq);
        COD1S0.set(t,-i, seq);
        COD3S0.set(t, i, seq);
        t+=fpgaPort.getAnalogTimebase();
    }
    seq.genTimingTable("c:/tmp_"); //prints table of data
    seq.start(); //starts sequence.
    seq.release(); //doent work yet.
}
```

Make sure that you use only one channel of each DAC if in fast mode. The `setLDacChn` in combination with `setAnalogTimebase` determine when the voltage has to be fired by dac and also the timesteps which need to be met in order not to overwrite the values of previous programming cycle.

Listing B.5: Key function of myAnalogOutLine

```
/**
 *@brief sequenced setter, double as value parameter
 *@param t time the value to be set
```

B.2 Example Code

```

    */param val double voltage value
    */param seq sequence variable
    */
void myAnalogOutFPGA::set(double t, double val, CSequenceFPGA &seq) {
    double tStart = t;
    checkVoltageRange(&val);
    _value = val;
    CDigitalOutFPGA *dPort =
    static_cast<CDigitalOutFPGA*>(_CSLINE->getDigitalPort());
    double aTB = dPort->getAnalogTimebase();
    double lDC = dPort->getLDacChn();
    int tmp = (int)(aTB*1e9/(ANALOG_SEQ_LEN*(lDC+1)) + 0.5); //0.5 due to
    rounding to next Int value
    double digTimeBase = tmp*1e-9;
    bool v = false; //value of serial protocoll in each
    iteration

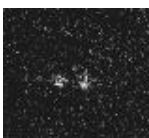
    //address input
    int aI = _subDacNr & 0x03;

    //data input
    unsigned int dI = (unsigned int)((val -
    _minV)*((0x01<<16)-1)/(_maxV-_minV)) & 0xffff;

    if (lDC != 0) //if in serial mode, then the protocoll is
    1 bit shorter due to missing lDAC
        t = t+(_subDacNr)*digTimeBase*(ANALOG_SEQ_LEN-1);
    if(lDC < _subDacNr && lDC !=0 ){
        cerr << "\n Chipselect Channel is lower than used subDacNr!\n" <<
        endl;
        return;
    }

    //[value - min] * [2^16-1
    combination] / [Voltage Range]
    _RESETLINE->set(t,true,seq); //not sure why needed

    //addressing the subdac @ serial protocoll
    for (int i=1; i >= 0; i--) {
        v = (aI >> i) & 0x01;
        _CSLINE->set(t,0,seq);
        _LDACLINE->set(t,1,seq);
        _DILINE->set(t,v,seq);
        t+=digTimeBase;
    }
}
```



B. IMPLEMENTATION OF ARBITRARY WAVEFORM GENERATOR - MYANALOGOUTLINE

```
//generating bitwise Data
for (int i=15; i >= 0; i--) {
    v = (dI >> i) & 0x01;
    _CSLINE->set(t,0,seq);
    _LDACLINE->set(t,1,seq);
    _DILINE->set(t,v,seq);
    t+=digTimeBase;
}

//final steps Chipselect back hi and ldac setts
_CSLINE->set(t,1,seq);
t+=digTimeBase;
_LDACLINE->set(tStart+aTB-digTimeBase,0,seq);
t+=digTimeBase;
_LDACLINE->set(tStart+aTB,1,seq);
}
```
